MICRORHEOLOGY OF SOFT MATTER

Daniel Tien-Nang Chen

A DISSERTATION

in

Physics and Astronomy

Presented to the Faculties of the University of Pennsylvania

in Partial Fulfillment of the Requirements for the Degree of Doctor of Philosophy

2010

Supervisor of Dissertation

_____

Arjun G. Yodh

Professor of Physics and Astronomy

Graduate Group Chairperson

_____

Ravi Sheth, Professor of Physics and Astronomy

Dissertation Committee

Tom C. Lubensky, Professor of Physics and Astronomy

John C. Crocker, Associate Professor of Chemical and Biomolecular Engineering

Mark Goulian, Associate Professor of Physics and Astronomy and of Biology

Masao Sako, Assistant Professor of Physics and Astronomy

Dedication

To my family

Acknowledgements

The work in this thesis is the product of many years of investigation. Many people have contributed to this enterprise, some directly, others in unobvious, but equally important ways.

First and foremost, I am grateful to my advisor, Arjun Yodh, who constantly challenged and created opportunities for me throughout my PhD. Without his steadfast guidance and support, this thesis would not have been possible. What I admire most about Arjun is his focus, integrity, and openness to letting students take responsibility for seeing their ideas through to fruition. By setting the bar high and leading through questioning, Arjun illuminates the path for students to discover the answers for themselves. Looking back, it has been a real luxury to grow as a scientist in Arjun's lab.

I am very grateful to my committee members for their time and consideration: Tom Lubensky, John Crocker, Mark Goulian, and Masao Sako. Their generosity has made the final stages of this dissertation relatively stress-free.

I feel privileged to have obtained my degree in soft matter at Penn where I've had the opportunity to learn from the best people in the field. In particular, John Crocker and Tom Lubensky have always openly shared their insights into the experimental and theoretical underpinnings of microrheology with me. It was a real pleasure collaborating with them. Mark Goulian and his lab generously shared their expertise on bacteria with me, which was crucial during the early stages of the project. My good friend and collaborator Andy Lau worked closely with me throughout my PhD and exponentially expanded my knowledge of physics. I feel fortunate that he took me under his wing.

Acknowledgements are due to many colleagues whose camaraderie both in and out of the

lab has made my seemingly impoverished grad student life so rich. Early on, Mohammad Islam and Keng-Hui Lin led me into the lab and made my transition from student to researcher a smooth one. Over the years, I have benefitted greatly from many stimulating collaborations and discussions with my fellow time-travellers: Mateusz Bryning, Ahmed Alsayed, Jonathan Fisher, Regine Choe, Turgut Durduran, Alper Corlu, Hsing-Wen Wang, David Busch, Jian Zhang, Zvonimir Dogic, Yilong Han, Larry Hough, JC Loudet, Oni Basu, Kevin Aptowicz, Piotr Habdas, Zexin Zhang, Ke Chen, Peter Yunker, Matt Lohr, Matt Gratale, Jennifer Lynch, Sophie Chung, and Nico Bodenschatz. Their enthusiasm and support has made the Yodh lab a wonderful place to work. My classmate and good friend Paul Biancaniello, who was coincidentally the first person I met within hours of arriving in Philadelphia, has been a constant source of intellectual rapport and has always been there for me during challenging times.

My research efforts have been greatly aided by logistical support from the LRSM office: Fred Hellmig, Raymond Hsiao, and Marcelyn Kuklinski. I would also like to acknowledge Drew McGhie for including me in many educational outreach opportunities.

I am grateful to my early scientific mentors at Berkeley, Musa Ahmed and Kam-Biu Luk, whose encouragement and positive example inspired me to follow in their footsteps.

Outside the lab, many friends have had a tremendous impact on my well-being. My Metacomm friends: Kevin and Karen Rowe, Sean and Jennifer Daly, Patrick and Jane Conlin, Jason and Kashi Behrstock have skipped the stones of life with me. Their kindness, optimism, and adventurous outlook has sustained me all these years. Kevin is one of the most generous and in-tents people I know and his friendship has had a deep influence on my personal development. My life in Philadelphia would not have been so good without the fortuitous companionship of

my childhood friends Gary Liu and Ben Todd, fellow PhD travailers Bei Xiao and Andre Brown, Kate Norton, Sun-Sun Chen, Earl Wagner, and guitar *sensei* Ron Bennett.

Finally, I would not be able to walk out of the lab today were it not for the love and support of my family. This thesis is dedicated to them. My parents, Mark and Grace Chen, whose love made me the person that I am today. From an early age, they instilled in me the importance of education and provided a stable home without which I would not have had the courage to pursue this path. My mother was actually my first science teacher. It was she who many years ago first exposed me to the mysterious organization of the periodic table of elements, and in the process, sparked my fascination with science. My little brother and sister-in-law, Alan and Wendy Chen, have always looked out for me, rather than the reverse. My grandmother, Yu Ju Hsu, and my dearly departed grandparents, Ming Hsu, Chi Jong and Jong Yu Chen, who lived through turbulent times without losing their sense for the important things in life. Under their umbrella we stand. I remember them here.

Abstract

Microrheology of Soft Matter

Daniel Tien-Nang Chen

Arjun G. Yodh

This thesis describes the application of microrheology to characterize the mechanical properties of three soft matter systems: an entangled biopolymer solution, a suspension of actively swimming bacteria, and a gel-forming carbon nanotube network. We demonstrate using these distinct model systems that it is possible to employ microrheology to extract both local and bulk information using a combination of one- and two- point measurements and theoretical modeling.

In the first set of experiments, we use microrheology to probe the rheological properties of semi-dilute polymer solutions of λ-DNA. In these solutions, the depletion interaction leads to a layer of reduced DNA density near the particle's surface. We demonstrate a method for deducing the local microstructure of these layers along with the bulk rheology of the polymer solution. This work was one of the first to systematically demonstrate that tracer-based microrheological methods could be used to deduce both local and bulk rheology in a well-characterized model soft matter system.

In the second set of experiments, we use microrheology to probe the dynamics of a model active soft matter system: a suspension of swimming bacteria. By comparing measurements of the fluctuations of passive tracer particles with the response of a driven, optically trapped tracer in the bacterial bath, we demonstrate a breakdown of the fluctuation-dissipation theorem

in bacterial baths. These measurements enable us to extract the power spectrum of the active stress fluctuations. We develop a theoretical model incorporating coupled stress, orientation, and concentration fluctuations of the bacteria to explain the observed scaling of the power spectrum.

In the final set of experiments, we report measurements of gelling rigid rod networks, comprised of a semidilute dispersion of surfactant stabilized carbon nanotubes. Microrheology is employed to follow the rheological evolution of the suspension from a semidilute solution of unbonded tubes to a bonded gel network. A theoretical model based on the crossing probability of rods confined to finite volumes is developed to account for network elasticity. Model predictions compare well with computer simulations and experiments as a function of nanotube volume fraction and cure time.

Contents

List of Tables

List of Figures

Chapter 1

Introduction

Imagine looking, as people in the 18th Century did, at particles in water under a microscope. The jiggling motions of micron-sized objects that you are observing might, based on the intuitive association between motion and life, be attributed to the particles being ‘alive’. It wasn’t until 1826 that the careful experiments of Robert Brown showed that they were in fact the consequence of thermal fluctuations of ‘dead’ matter. In 1905, Einstein considered Brownian motion using kinetic theory and in a stroke of insight, he offered compelling evidence for the atomic hypothesis. In this thesis we build on these seminal insights to ‘decode’ the jiggles resulting from thermal and active motion of particulate matter in a variety of soft materials.

1.1 Soft matter/complex fluids

The rise of soft matter from a subaltern to mainstream discipline of physics has been fueled in part by the promise of deciphering the ‘rules’ of self-assembly, an endeavor which, if realized,

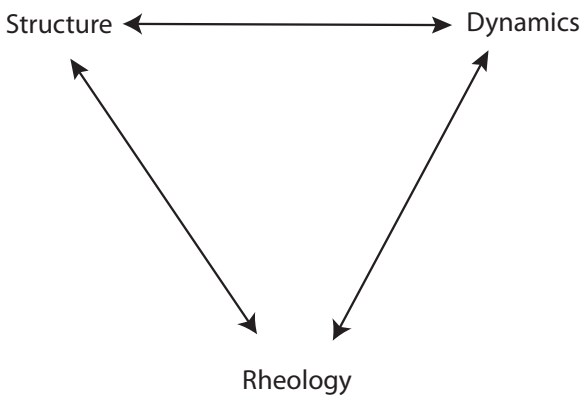

Figure 1.1: Structure, Dynamics, and Rheology of Soft Matter

could enable large-scale engineering of complex structures with broad societal impact. Moreover, the potential for leveraging its methods of inquiry to yield new insights about other fields such as molecular biology and chemical/bio/mechanical engineering has also generated much scientific interest in soft matter physics.

Characterization of a colloidal suspension, polymer network, or emulsion requires that the relationship between its structure, its equilibrium and non-equilibrium dynamics, and its rheology be determined. These categories, sketched in Figure 1.1, are not independent. In most materials they are coupled, albeit not in a simple universal manner. A concrete example is the hard sphere colloidal suspension, illustrated in Figure 1.2. In equilibrium, random collisions among particles (blue spheres) with liquid-like order make the suspension resistant to flow. But as the shear stress or, equivalently, the shear rate increases, the particles become ordered into lane-like configurations. These lane-like configurations have a lower viscosity relative to the

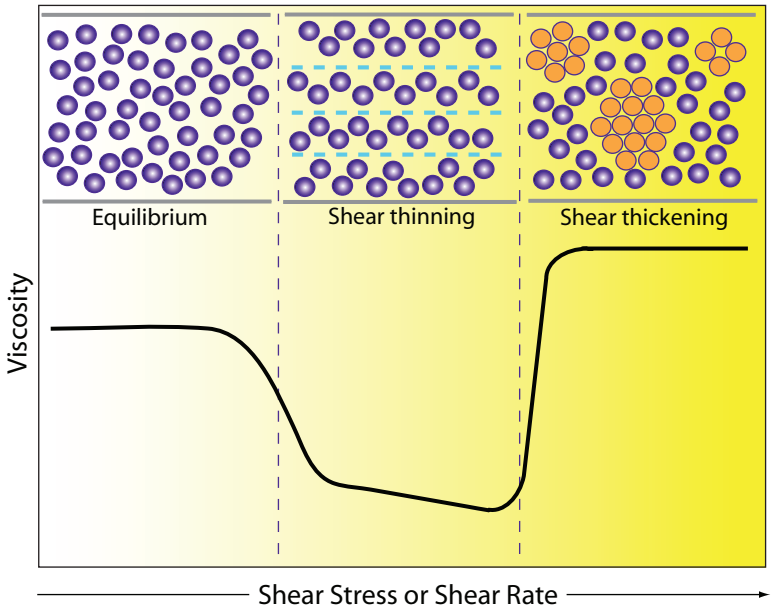

Figure 1.2: Relationship between structure, dynamics, and rheology in the shear thinning-shear thickening transition in hard sphere colloidal suspensions. Adapted from [113].

more randomized configurations. At yet higher shear rates, hydrodynamic forces between particles dominate over stochastic ones, a change that disrupts the order and spawns hydroclusters, i.e. transient fluctuations in particle concentration. The difficulty that particles have in flowing around each other in such a strong flow leads to a higher rate of energy dissipation and an abrupt increase in viscosity [113]. Thus, it is clear that a combination of rheological and structural measurements is necessary to fully elucidate such phenomena in even a relatively simple system; any single measurement modality would be insufficient.

An important way that we learn about the structure and dynamics of soft matter is to probe them mechanically. Rheology measurements typically subject a material to shear in a prescribed geometry and the material's resulting stress and strain are measured to extract its shear and elastic moduli. These moduli are measures of a material's intrinsic elastic properties, analogous to specific heat capacity and various coefficients of heat transport or resistivity and electrical

transport.

Real materials, and especially soft materials, are neither ideal solids nor ideal liquids. Real soft materials exhibit both elastic and viscous responses and are therefore called viscoelastic. The internal structures of soft solids and complex fluids composed of colloidal particles, filamentous and flexible polymers, and other supra-molecular arrangements lead to complicated mechanical responses. As a result, the relations between stress and strain are not simply defined by elastic and viscous *constants*; rather, these relations can be functions of time, direction, and extent of deformation. The goal of rheological experiments is to quantify the viscoelasticity of a material over as wide a range of time and deformation scales as possible and, ultimately, to relate these viscoelastic properties to the molecular meso- and macro- structure of the material. Today, the rheology of many soft materials, both biological and synthetic, is often very different from that of materials like rubber for which theoretical models have proven highly effective. Thus many open questions remain about how to relate structure to viscoelastic response.

1.2 Overview of rheology/microrheology techniques

Rheology is a well established methodology for extracting information from material deformation [21]. Rheometry has been a standard method to characterize materials in industry for most of the twentieth century. In concert with the tremendous insights generated by computational advances (e.g. molecular dynamics simulations) that have occurred at the end of the 20th century (and continue today), rheology has generated valuable insight into the detailed microscopic molecular motions of polymers for example. However, in its conventional implementations,

rheology has limitations; it requires a large amount of material, it typically operates at low frequency, and it measures motions over relatively large length scales (mm's).

Relatively recently, owing in part to innovations in light scattering techniques and digital video microscopy, it has been realized that rheological information can be extracted from an analysis of the motions of micron-scale probe particles embedded in the material. This suite of new measurement technologies, termed *microrheology*, has augmented the scope of materials and the range of length and time scales that can be studied. Importantly, microrheology has enabled the study of materials in situations wherein traditional rheometers are difficult to use, e.g., when the material is available only in very low quantities ($< 1mL$) . Moreover, microrheology has been useful in situations where removal of materials from their natural (*in situ*) contexts alters their ability to function, such as in living cells. This thesis describes applications of microrheology to the study of soft matter.

Rheometers generally measure two quantities: stress, the amount of force per unit area applied to the sample; and strain, the dimensionless degree to which the material deforms. The materials' properties, quantified as elastic moduli for solids or viscosities for liquids, are calculated from the ratio of stress to strain or stress to strain rate, respectively. To characterize fully the viscoelastic properties of complex soft materials, the relation of stress to strain must be measured over a wide range of strains, strain rates, and time scales (Figure 1.3). Unfortunately, quite often existing instruments and methods either cannot cover a large enough range or else disrupt the material during measurements. Thus, recent advances in rheological methods have been motivated in part by attempts to measure delicate samples with complex time-dependent responses at the micron scale. These microrheological methods have even been extended for

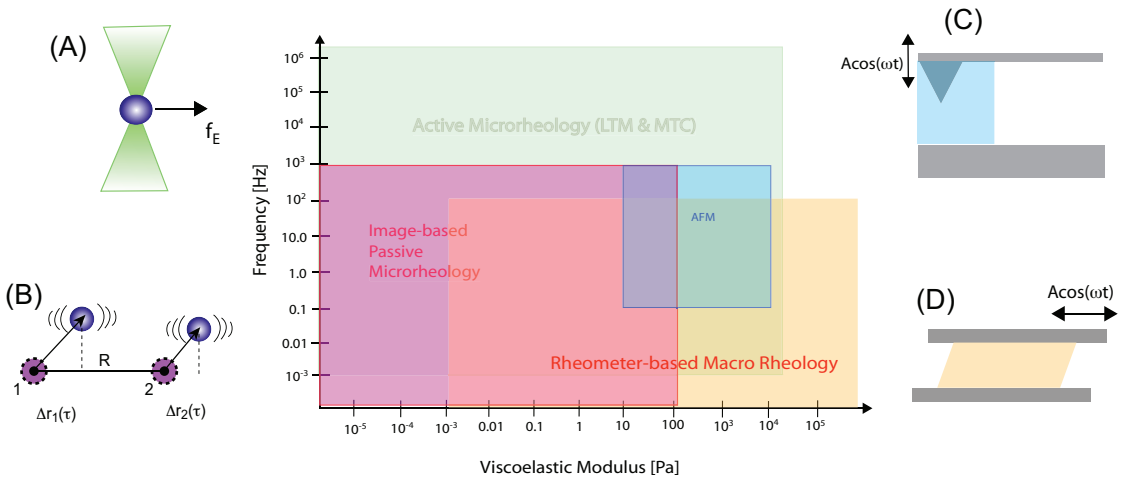

Figure 1.3: Rheological Techniques employed to probe soft materials. Main Figure: Typical frequency and viscoelastic modulus range of techniques. (Note: contours represent min/max ranges of the techniques). Schematic illustrations of A) Active microrheology using optical tweezers to force probe particle. B) Passive two-point microrheology using image-based particle tracking. C) Dynamic material deformation using atomic force microscopy (AFM). D) Oscillatory Macrorheology.

use in live cells. Additional experimental and theoretical progress has been made on systems far from equilibrium, e.g., systems in which non-thermal sources of energy drive fluctuations and rheological responses.

As with any other new measurement technology, questions have been raised about the limitations of microrheology. Chief among these, circa the early 2000's, was the effect of material heterogeneity on the interpretation of probe based microrheological measurements. For example, when these heterogeneities exist, can the bulk moduli even be measured using microrheology? Whereas these issues can complicate interpretation of experimental data, such complications can be cleverly turned around to increase the amount of information available from a microrheology experiment. In a different vein, the ability to probe miniscule, inhomogeneous,

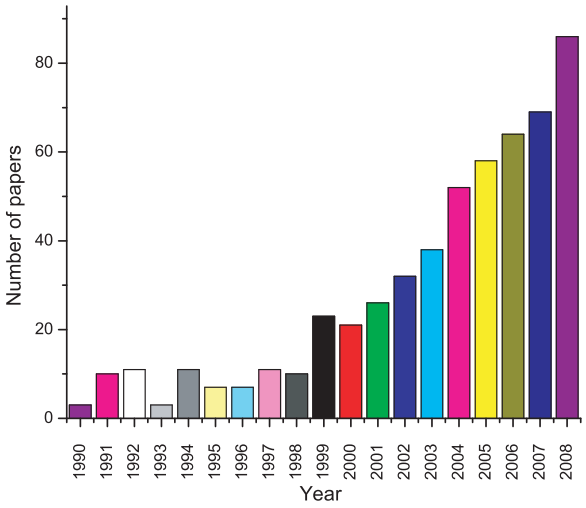

Figure 1.4: Number of papers published with keyword “microrheology” in title, abstract, or sorting field as determined by the ISI (Web of Science) online database.

out-of-equilibrium materials *in situ* and at high bandwidth holds the potential to reveal new insights about the inner workings of living cells [57], sensorimotor assemblages [67], and novel materials (e.g., self-healing materials [22]). This excitement has led to a growth of activity in the subfield of microrheology. Figure 1.4 shows the number of published papers containing the keyword “microrheology” in the title, abstract, or sorting category for each year spanning the period 1990 - 2008, as determined by Thomson Scientific’s ISI Web of Knowledge database. Assuming that the number of papers per year is a reflection of science interest in microrheology, the results are indeed indicative of exciting progress and potential.

1.3 Organization

The remainder of this thesis is organized as follows. In Chapter Two, we introduce the theoretical underpinnings of rheology and microrheology. In doing so, many of the issues that arise in interpretation of microrheological data will be introduced. In Chapter Three, we describe the

experimental methods commonly employed in microrheology experiments, many of which have been used in this thesis. In Chapter Four, we describe measurements of the viscoelastic response of entangled polymer solutions using λ-DNA as a model system [18]. This study highlights the use of thermal microrheology to quantitatively characterize mechanical heterogeneities around the probe particles, in this case stemming from depletion interactions between the probe and the DNA solution. Chapter Five describes microrheological experiments on suspensions of actively swimming bacteria [20]. Bacterial baths constitute a model of active matter in a driven non-equilibrium steady state. The work explores the extent that the theoretical framework employed to interpret results from equilibrium systems can provide an adequate characterization of a non-equilibrium system. Our work explicitly demonstrates how theory must be modified to accommodate non-equilibrium systems. In Chapter Six, we describe measurements of a gelling suspension of single-walled carbon nanotubes [19]. Of primary interest is our new access to the dynamics of the incipient gel which microrheological measurements permit. We introduce theoretical models and computer simulations of rigid rods in a confined volume to elucidate the role of bonding in this network class. The work described in Chapters 4-6 has been published [18–20], and the chapters follow largely from these papers with some amplification of ideas. Finally, we conclude and give some future directions for work in Chapter Seven.

Chapter 2

Theory

2.1 Introduction

The rheological behavior of most complex materials, particularly soft materials, can exhibit many regimes depending on the scale, geometry, amplitude, and rate of the imposed deformation. Consider the classic toy: silly-putty. When squeezed slowly, it deforms and flows like a liquid; however, when thrown against a wall, it bounces like a rigid elastic solid. Many techniques have been developed to characterize these behaviors. Broadly speaking, there are two classes of rheological measurements: macrorheology and microrheology. In this chapter, I will describe the theoretical underpinnings of these methodologies. Much of the material on macrorheology in this Chapter can be found in textbooks including Landau and Lifshitz [54], Ferry [36], Macosko [65], Doi and Edwards [32], Larson [56], and Rubinstein and Colby [87]. Much of the material on microrheology is covered in review articles [99, 114].

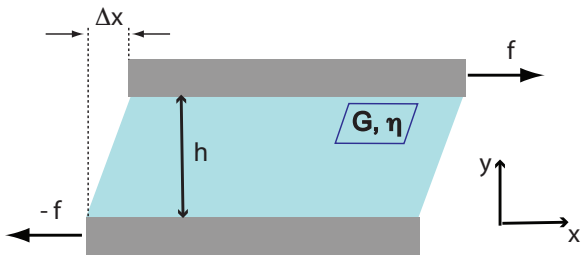

Figure 2.1: Two-dimensional representation of simple shear.

2.2 Macrorheology

2.2.1 Basic Definitions

Consider a material sandwiched between two parallel plates, as depicted in Figure 2.1. This is a prototypical set-up encountered in macrorheology experiments. In this simple shear apparatus, the top plate is displaced with a force f in the x-direction, and the force is transmitted to the bottom plate through the material. The adhesion between the material and the surfaces is considered to be strong enough such that there is no slippage at either surface. If the material is totally rigid, the bottom plate must be held in place by a force $-f$ to prevent net translation in the +x direction. The shear stress, σ_{xy} (simply denoted σ), resulting from the force exerted in the $+x$ direction and transmitted to a planar cross-sectional area A normal to the y-direction is defined as:

$$\sigma \equiv \frac{f}{A}. \tag{2.1}$$

The units of stress are force per unit area ($Pa \equiv kg\ m^{-1}\ s^{-2}$ in SI units). The shear strain γ is defined as the displacement of the top plate Δx divided by the thickness of the sample h:

$$\gamma \equiv \frac{\Delta x}{h}. \tag{2.2}$$

If the material is a perfectly elastic solid (as it sometimes is for low strains), then the stress will be linearly proportional to the strain. The constant of proportionality, known as the shear modulus G, is defined by:

$$G \equiv \frac{\sigma}{\gamma}. \tag{2.3}$$

The shear modulus has the same units as the shear stress, since strain is dimensionless. Each sub-parcel of the material subjected to shear will experience the same local stress and strain, assuming the material deformation is uniform, or affine. The property of elastic materials, that the modulus is constant over a range of strains is more generally known as Hooke's law of elasticity, a constitutive relation valid in the linear response regime (typically $\gamma < 4 - 5\%$). A generalization of Hooke's Law is explicated in Landau and Lifshitz's Theory of Elasticity [54]. In passing, I remark on some notable features of this formalism that will be of use in understanding literature associated with the subjects in this thesis.

First, stress (σ_{ij}) and strain (γ_{kl}) are 2nd rank tensors, and stiffness (C_{ijkl}) is a 4th rank tensor connecting them, i.e., $\sigma_{ij} = C_{ijkl}\gamma_{kl}$. Or, as is sometimes denoted in the literature: $\sigma = \mathbf{C} : \gamma$. The total number of independent components of C_{ijkl} is reduced from 81 to 21 due to the stress and strain tensors being symmetric, i.e., $\sigma_{ij} = \sigma_{ji}$, $\gamma_{kl} = \gamma_{lk}$, implying $C_{ijkl} = C_{jikl} = C_{ijlk}$ and the symmetry of the stiffness tensor as a consequence of the strain energy U being a quadratic function of the strain to lowest order, i.e., $U = \frac{1}{2}\int C_{ijkl}\gamma_{ij}\gamma_{kl}d^dx$,

implying $C_{ijkl} = C_{klij}$. Since the trace of any tensor is independent of basis, the most complete coordinate-free decomposition of the strain tensor is to represent it as the sum of a constant tensor and a traceless symmetric tensor:

$$\gamma_{ij} = \frac{1}{3}\gamma_{kk}\delta_{ij} + (\gamma_{ij} - \frac{1}{3}\gamma_{kk}\delta_{ij}). \tag{2.4}$$

The first term on the right is known as the volumetric strain tensor; it corresponds to deformations akin to hydrostatic compression. It is straightforward to show that for small (linear) deformations, the volume change given by $dV' = dV(1 + \gamma_{ii})$, where the prime denotes the volume of a parcel of the deformed material. In other words, the relative volume change is equal to the trace of the strain tensor: $(dV' - dV)/dV = \gamma_{ii}$. If the trace of the strain tensor is non-zero ($\gamma_{ii} \neq 0$), then the resulting deformation will not be volume-conserving. The second term, known as the deviatoric strain tensor, or shear tensor, is traceless, corresponding to a volume-conserving shear deformation. Any arbitrary deformation can be captured by a linear combination of these two elementary deformations, and thus a generalized Hooke's Law for isotropic materials is:

$$\sigma_{ij} = 3K(\frac{1}{3}\gamma_{kk}\delta_{ij}) + 2G(\gamma_{ij} - \frac{1}{3}\gamma_{kk}\delta_{ij}). \tag{2.5}$$

Here K is known as the bulk modulus, and G is known as the shear modulus. Written in this way, it is clear that K and G are elements of the stiffness tensor C_{ijkl} for isotropic media. For other symmetries, e.g. crystalline, there will be additional elements corresponding to the underlying symmetries of the structure. There are many equivalent ways to express the

information of Eq. 2.5. For instance, it can also be written as:

$$\sigma_{ij} = \lambda\gamma_{kk}\delta_{ij} + 2\mu\gamma_{ij}, \tag{2.6}$$

where λ, μ are known as Lamé coefficients and are related to K, G via $\lambda = K - \frac{2}{3}G$ and $\mu = G$. It is sometimes more convenient to use the Lamé coefficients because the stiffness tensor can be written: $C_{ijkl} = \lambda\delta_{ij}\delta_{kl} + \mu(\delta_{ik}\delta_{jl} + \delta_{il}\delta_{jk})$. Also, the free energy of a deformed isotropic material is, to lowest (harmonic) order a neat quadratic function of the strains: $F = F_0 + \frac{1}{2}\lambda\gamma_{ii}^2 + \mu\gamma_{ij}^2$.

The elementary deformations are summarized in Figure 2.2. When a material is stretched in one direction, it tends to contract (or occasionally, expand) in the other two directions perpendicular to the direction of stretch. Conversely, when a sample of material is compressed in one direction, it tends to expand (or rarely, contract) in the other two directions. The Poisson ratio ν relates the elongational strain to volumetric change in materials, i.e., $\Delta V/V = (1 - 2\nu)\Delta L/L$. For incompressible materials, $\nu = \frac{1}{2}$. In general, the elastic properties of homogeneous isotropic linear elastic materials are uniquely determined by any two quantities among K, G, E, ν; thus, given any two moduli, any other of the elastic moduli can be determined.

By contrast, if the material is a pure liquid, the shear stress is independent of strain. Rather, shear stress depends linearly on the shear rate $\dot{\gamma} \equiv \frac{d\gamma}{dt}$. The constant of proportionality, known as the viscosity η, is defined by:

$$\eta \equiv \frac{\sigma}{\dot{\gamma}}. \tag{2.7}$$

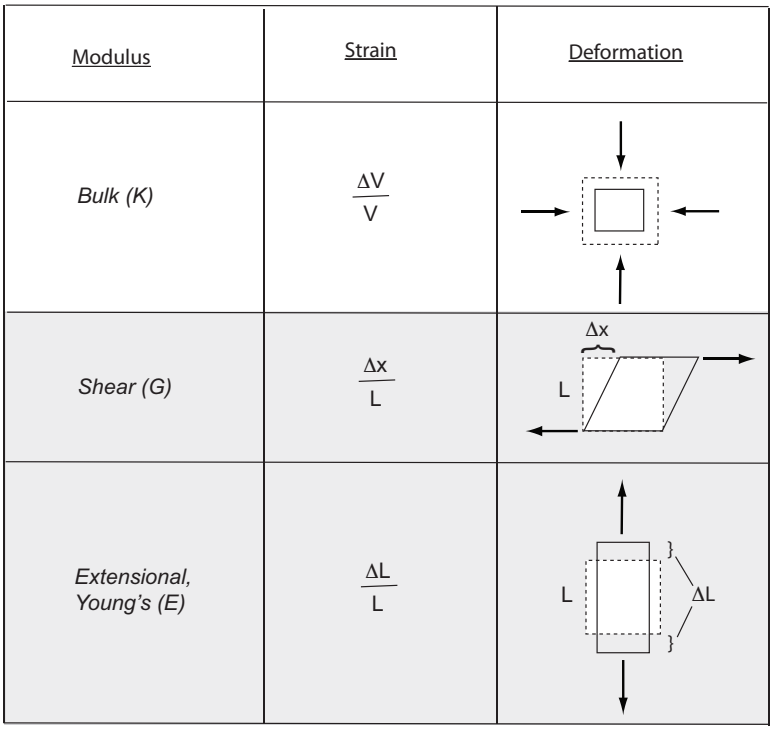

Figure 2.2: Elementary deformations, modulus, and strain for homogeneous isotropic materials. Dashed figure in deformation column corresponds to material prior to deformation. Shaded region corresponds to volume-conserving deformations.

Viscosity has units of force per unit area time (Pa s in SI units). Fluids for which Eq. 2.7 holds are known as Newtonian fluids. Note that for such fluids, the resistance to deformation (shear stress) depends on the rate of deformation and not the amplitude of the deformation, as for solids. As anyone who swims knows, it's not how large the stroke that matters, but rather how fast the stroke. A similar analysis to Eqns. 2.4 - 2.6 can be carried out to generalize the stress-strain relation for Newtonian fluids. Essentially, it is the same with the substitution of strain rate tensor v_{ij} for u_{ij}, and substitution of bulk and shear viscosities for bulk and shear moduli.

2.2.2 Viscoelasticity

Most soft materials are viscoelastic, having time-dependent mechanical responses intermediate between Newtonian fluids and Hookean solids. A time-dependent generalized shear relaxation modulus $G(t) \equiv \sigma(t)/\gamma$ is necessary to describe this behavior. Imagine imposing a constant stress, σ_0, at time $t = t_0$, and then monitoring the stress in the material as shown in Figure 2.3. For a Hookean solid with shear modulus G, the stress will be γG for as long as the stress is applied and then it will rapidly return to zero once the strain is released. For a Newtonian liquid, the stress will exhibit an initial transient spike and then decay rapidly to zero. For a dominantly liquid-like viscoelastic material, the stress will decay exponentially to zero with a characteristic relaxation time τ, as shown in Figure 2.3B.

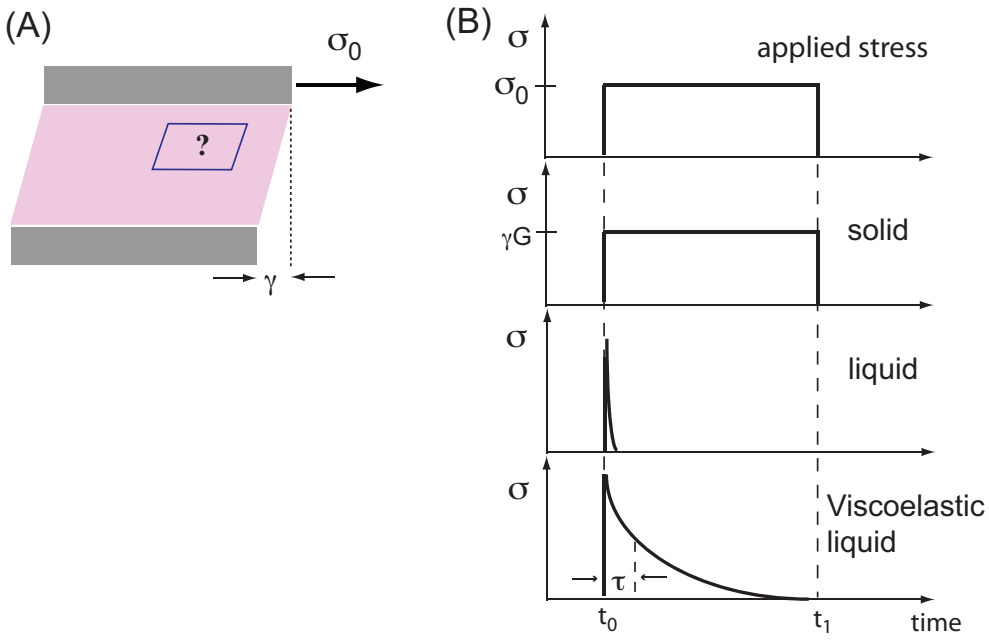

Figure 2.3: Stress relaxation in soft materials. (A) Schematic illustration of stress σ_0 being applied to a solid, liquid, or viscoelastic liquid material. (B) Stress profile for solid, liquid, and viscoelastic liquid materials. (Top) The step stress σ_0 is applied at time t_0 and removed at time t_1. τ is the relaxation time of the decaying stress in viscoelastic liquid.

In order to gain insight into the rheological responses of linear viscoelastic materials, including the factors that control the relaxation time, simple mechanical models of linear viscoelastic behavior have proven to be very useful conceptual aids. Mechanical models of viscoelastic materials utilize linear combinations of springs and dashpots to mathematically model elastic and viscous components, respectively. The elastic elements can be modeled as springs with elastic modulus G with a stress-strain relation:

$$\sigma = G\gamma, \tag{2.8}$$

where σ is the stress, G is the shear modulus of the material, and γ is the strain that occurs under the given stress, similar to Hooke's Law. The viscous components can be modeled as dashpots such that the stress-strain rate relationship can be given as

$$\sigma = \eta\frac{d\gamma}{dt}, \tag{2.9}$$

where η is the viscosity of the material, and $\frac{d\gamma}{dt}$ is the strain rate. Eq. 2.9 predicts that stresses in the viscous element will be larger whenever sudden deformations are imposed.

The simplest mechanical models for viscoelastic behavior are the Maxwell and Voigt models. The Maxwell model idealizes the viscoelastic material as a spring in series with a dashpot, as depicted in Figure 2.4. The Maxwell model captures the essential features of the rheology of an entangled polymeric network. In such an entangled polymer network, stresses in the network can relax at long times, whereas for short times, entanglements between polymer strands prevent relaxation and give rise to a dominantly elastic rheological response. Accordingly, such networks

possess a relaxation time scale, below which the response is dominantly elastic and above which the response is dominantly viscous. Under a sudden imposed strain, as depicted in Figure 2.4C, the spring element will initially bear the full strain in the system owing to the fact that the stress in the viscous element is large. Over time, the strain will relax to zero as the strain is transferred to the dashpot.

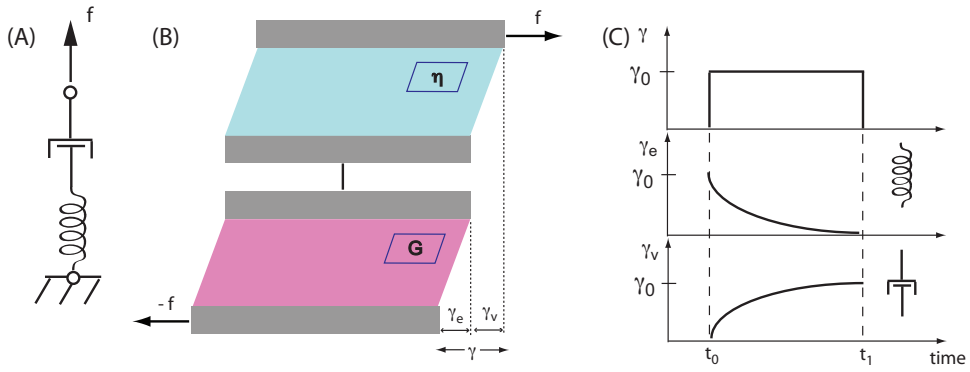

Figure 2.4: (A) Maxwell elements of spring and dashpot in series. (B) Maxwell Model for viscoelastic materials is a Newtonian liquid with viscosity η and Hookean solid with shear modulus G. Shear stress is transmitted serially through each material via the plates. (C) (top) Step strain γ_0 is imposed at time t_0 and held constant until time t_1 whereupon it is released. (middle) Time-dependent strain (extension) in the elastic element. Initially the imposed strain is fully accommodated in the elastic element and then it slowly decays. (bottom) Time-dependent strain (extension) in the viscous element. Initially there is no strain in the dashpot and then it increases. Note that upon release of strain at $t = t_1$, there is no recovery if (as shown) the strain in the elastic element has completely relaxed.

Under an imposed total strain $\gamma = \gamma_e + \gamma_v$, the strain across the elastic spring γ_e and the strain across the viscous dashpot γ_v are free to adjust until stress on both elements is the same, i.e.,

$$\sigma = G\gamma_e = \eta\frac{d\gamma_v}{dt}. \tag{2.10}$$

In the step strain experiment, a constant strain γ_0 is applied at $t = 0$ and the time dependent

strain in the viscous element is given by

$$\tau \frac{d\gamma_v(t)}{dt} = \gamma_0 - \gamma_v(t), \tag{2.11}$$

where the relaxation time $\tau \equiv \eta/G$. Solving,

$$\frac{d\gamma_v(t)}{\gamma_0 - \gamma_v(t)} = \frac{dt}{\tau}, \tag{2.12}$$

$$\ln[\gamma_0 - \gamma_v(t)] = \frac{-t}{\tau} + C. \tag{2.13}$$

Here the initial condition $\gamma_v(0) = 0$, yields $C = \ln \gamma_0$, and the strain in the elastic element $\gamma_e(t)$ equals:

$$\gamma_e(t) = \gamma_0 - \gamma_v(t) = \gamma_0 \exp(-t/\tau). \tag{2.14}$$

Since the elements are in series, the stress across both elements is identical thus:

$$\sigma(t) = G\gamma_e(t) = G\gamma_0 \exp(-t/\tau). \tag{2.15}$$

The stress decays to its equilibrium value exponentially with a relaxation time $\tau = \eta/G$, as shown in the bottom panel of Figure 2.3C. In the Maxwell model, the stress relaxation modulus $G(t) \equiv \sigma(t)/\gamma_0 = G\exp(-t/\tau)$. Thus, the two main features of the stress relaxation are: one, the modulus is independent of strain in the linear regime and two, a single relaxation time governs the stress relaxation.

This two-element, one-relaxation-time Maxwell model is overly simplified, however; it turns out that more complex mechanical networks, approximating real polymer networks, can be modeled as multiple basic Maxwell elements of series springs and dashpots. Importantly, in the linear response regime, each independent mode has its own relaxation time. Network behavior is derived by combining these modes via linear superposition to yield a network stress relaxation modulus having a broader, multi-timescale decay profile. In real entangled polymer networks, for example, the distribution of relaxation times is a consequence of the multiple length scales in the underlying polymer length distribution, e.g., lengths of polymer segments between entanglement points or dangling polymer strands. These segments and strands each vibrate with a characteristic frequency which depends in part on the segment length and segment tension. Collectively, these thermally excited vibrations, somewhat analogous to a strummed chord on a guitar, give rise to a broader stress relaxation profile than predicted by the Maxwell model.

Another possibility in real polymer networks is for the strands to be cross-linked, as in a polymeric gel. In such a situation, the stresses in the network will never relax so long as a stress or strain is imposed. This feature is captured in the Voigt model as a spring in parallel with a dashpot, as depicted in Figure 2.5. After a step stress is imposed, the strain across both elements increases to a saturating value (Figure 2.5C). The stress is initially higher in the dashpot but eventually the stress is transferred entirely to the spring element at long times.

In the Voigt model, the strain, rather than the stress (as in the Maxwell model), is the same across both elements: $\gamma = \gamma_e = \gamma_v$. The total stress is thus the sum of the stresses on both elements and is free to adjust to accommodate the strain:

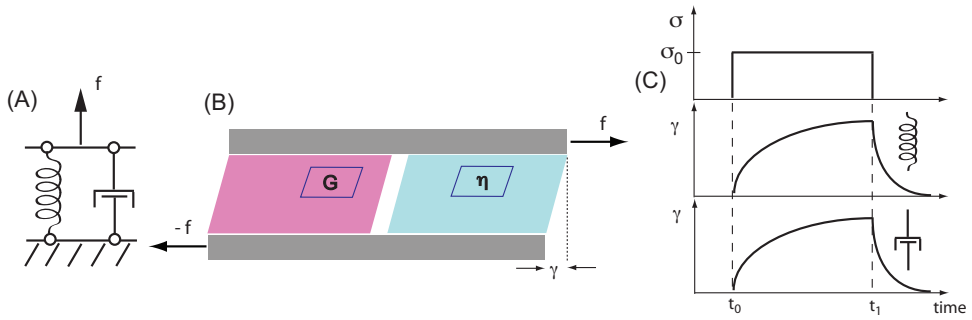

Figure 2.5: (A) Voigt elements of spring and dashpot in parallel. (B) Voigt model for viscoelastic materials is a Newtonian liquid with viscosity η and Hookean solid with shear modulus G. Shear stress is applied simultaneously to both media via the same plate. (C) (top) Step stress σ_0 is imposed at time t_0 and held constant until time t_1 whereupon it is released. (middle) Time-dependent strain (extension) in the elastic element. (bottom) Time-dependent strain (extension) in the viscous element. The strain in both elastic and viscous elements is the same due to the parallel geometry of the deformation. Note that the strain returns to its initial state upon the release of the stress at $t = t_1$ due to the elasticity in the spring.

$$\sigma(t) = G\gamma(t) + \eta\frac{d\gamma}{dt}. \tag{2.16}$$

Since materials obeying the Voigt model cannot be instantaneously deformed, an alternative deformation methodology in which a step stress is applied must be used to elicit the rheological response of the Voigt model. Applying a constant step stress $\sigma(t) = \sigma_0$ at $t = 0$, Eq. 2.16 becomes

$$\tau\frac{d\gamma}{dt} + \gamma = \frac{\sigma_0}{G}, \tag{2.17}$$

where $\tau = \eta/G$. Eq. 2.17 can be readily solved by following the procedure of Eq. 2.11 - 2.14 and applying the initial condition $\gamma(0) = 0$. The time-dependent strain for the Voigt model is thus

$$\gamma(t) = \frac{\sigma_0}{G}\left[1 - e^{-t/\tau}\right]. \tag{2.18}$$

The measurement used to illustrate the Voigt model in Figure 2.5C, wherein a constant step stress is applied to a material and its strain recovery is monitored, is known in rheological literature as creep response.The creep analogue of the shear relaxation modulus is known as the shear creep compliance, $J(t)$, and is given by the ratio of the time-dependent strain and stress: $J(t) = \gamma(t)/\sigma_0$. It follows from Eq. 2.18 that the creep compliance is:

$$J(t) = \frac{1}{G}\left[1 - e^{-t/\tau}\right]. \tag{2.19}$$

The main difference between the Voigt and Maxwell model is in their long time behavior. In both models the viscous stress in the dashpot is initially larger after the step strain (Maxwell) or stress (Voigt) is applied, and then it decays exponentially with time. In the Maxwell model, the consequence is that the stress decays to zero. In the Voigt model, the consequence is that the strain saturates to a constant value σ_0/G owing to the fact that in parallel the strain from the extension of the spring is always present and bears all the stress after the transients decay. It is also worth noting that the Voigt model will always return to its initial strain after the stress is turned off as shown in Figure 2.5C. In contrast, the Maxwell material will not return to its initial strain state, so long as the duration of the strain deformation exceeds the relaxation time. Thus the Voigt model is a hallmark of elastic behavior expected for gels. Accordingly, the Voigt model is a simple idealized model for polymeric gels wherein cross-links prevent long time relaxation of the deformed network. One such system is a carbon nanotube network cross-linked by van

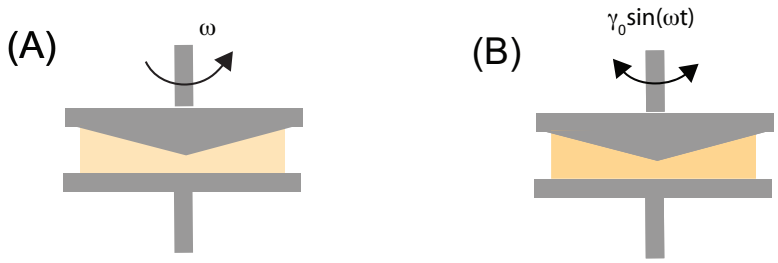

Figure 2.6: (A) Schematic of steady shear rheology measurement in a cone-and-plate geometry. The top cone is rotated at a constant angular velocity ω and the resulting stress or strain is measured. (B) Schematic of oscillatory rheology measurement. The top cone is rotated sinusoidally and the stress or strain is measured.

der Waals interactions. This gel (Voigt) system is further elaborated in Chapter 6. Entangled polymeric networks (Maxwell) of λ-DNA are the subject of Chapter 4.

2.2.3 Common Rheology Measurements

The two most common macrorheology measurements are steady shear and oscillatory measurements. In steady shear measurements, the top plate is rotated at a constant angular velocity ω, as illustrated in Figure 2.6A. The resulting stress is determined via:

$$\sigma(t) = \int_{-\infty}^{t} G(t-t')\dot{\gamma}(t')dt'. \tag{2.20}$$

Eq. 2.20 is a general statement of the Boltzmann superposition principle which states that the stress in the material at any given time is due to a linear superposition of its previous shear history. Since the shear rate $\dot{\gamma} = \omega$ is time-independent in steady shear measurements, we have

$$\sigma(t) = \dot{\gamma}\int_{-\infty}^{t} G(t-t')dt' = \dot{\gamma}\int_{0}^{\infty} G(\tau)d\tau, \tag{2.21}$$

where the variable substitution $\tau = t - t'$ has been made. This leads naturally to a definition of

viscosity as the time integral of the shear relaxation modulus:

$$\eta = \int_0^\infty G(t)dt. \tag{2.22}$$

This viscosity is known as the steady shear viscosity and can be empirically related to the more commonly measured dynamic complex viscosity $\eta^*(\omega)$ in many simple polymeric liquids via the Cox-Merz rule [56], which states that $\eta(\dot{\gamma}) \approx \eta(\omega)$.

Dynamic viscoelasticity measurements are made by applying a sinusoidally oscillating strain (or stress) to a sample and measuring its stress (or strain) response, respectively, as a function of frequency (Figure 2.6B). For linear viscoelastic materials, the result is two sinusoidal functions, and both the elastic and dissipative properties of the material are computed from the amplitudes and phase shifts of the sinusoidal functions, as illustrated in Figure 2.7. In strain-controlled oscillatory measurements, for example, the applied strain varies sinusoidally with time:

$$\gamma(t) = \gamma_0 \sin(\omega t), \tag{2.23}$$

which for a Hookean solid leads to a stress which is in phase with the strain:

$$\sigma(t) = G\gamma(t) = G\gamma_0 \sin(\omega t). \tag{2.24}$$

For a Newtonian liquid, by contrast, the stress depends on the rate of strain and as a result, the stress lags the strain by exactly $\pi/2$ phase shift:

$$\gamma(t) = \eta\frac{d\gamma}{dt} = \eta\gamma_0\omega\cos(\omega t) = \eta\gamma_0\omega\sin(\omega t + \frac{\pi}{2}). \tag{2.25}$$

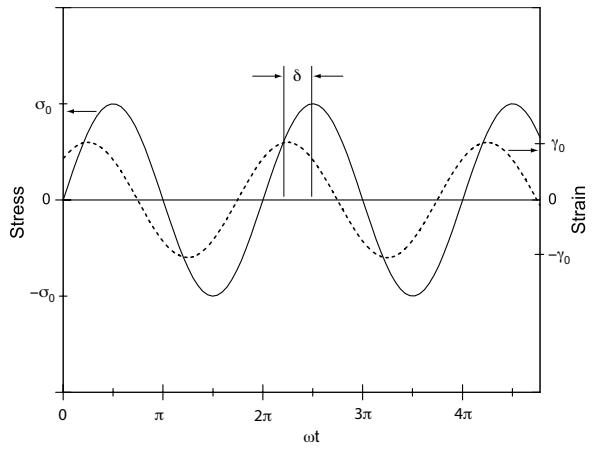

Figure 2.7: Stress σ_0 and strain γ_0 amplitudes vs ωt in an oscillatory deformation of a viscoelastic material. The stress and strain signals are phase shifted by an angle δ.

More generally, interpolating between these two extremes, viscoelastic materials can be characterized as having a stress which is out of phase with the strain by a relative phase angle $0 \leq \delta \leq \pi/2$:

$$\sigma(t) = \sigma_0 \sin(\omega t + \delta), \tag{2.26}$$

with the consequence that the stress and strain are related by the general expression:

$$\sigma(t) = \gamma_0 \left[G'(\omega) \sin(\omega t) + G''(\omega) \cos(\omega t) \right], \tag{2.27}$$

where $G'(\omega)$ is known as the storage modulus and $G''(\omega)$ is known as the loss modulus. Expanding Eq. 2.26 and comparing it to Eq. 2.27, it becomes clear that the storage and loss moduli at each ω can be related to the phase angle δ via:

$$G' = \frac{\sigma_0}{\gamma_0}\cos\delta$$
$$G'' = \frac{\sigma_0}{\gamma_0}\sin\delta$$
$$\tan\delta = \frac{G''}{G'}. \tag{2.28}$$

The ratio of the loss to storage moduli is given by $\tan\delta$, known as the loss tangent. The loss tangent is a useful measure of the degree of elasticity versus viscosity in a material. It is diverging for Newtonian fluids [$\tan(\pi/2) = \infty$] and zero [$\tan(0) = 0$] for Hookean solids. In principle, the oscillatory rheology of the material is completely characterized by knowledge of any two out of the three quantities: G', G'', δ. Equivalently, and more succinctly, the sentiment of Eqns. 2.28 can be mathematically expressed using the complex function:

$$G^*(\omega) = G'(\omega) + iG''(\omega)$$
$$\tan\delta(\omega) = \frac{G''(\omega)}{G'(\omega)}, \tag{2.29}$$

$G^*(\omega)$ is known as the complex shear modulus and $\tan\,\delta(\omega)$ is the frequency-dependent loss tangent. The complex shear modulus characterizes the overall resistance to deformation of a material, regardless of whether that deformation is recoverable (elastic) or non-recoverable (viscous). The information contained in the complex shear modulus can alternatively be expressed in terms of the complex dynamic viscosity $\eta^*(\omega)$ which is trivially related via $G^*(\omega) = -i\omega\eta^*(\omega)$. Typical linear oscillatory rheology data for a variety of common materials is illustrated in Figure

2.8.

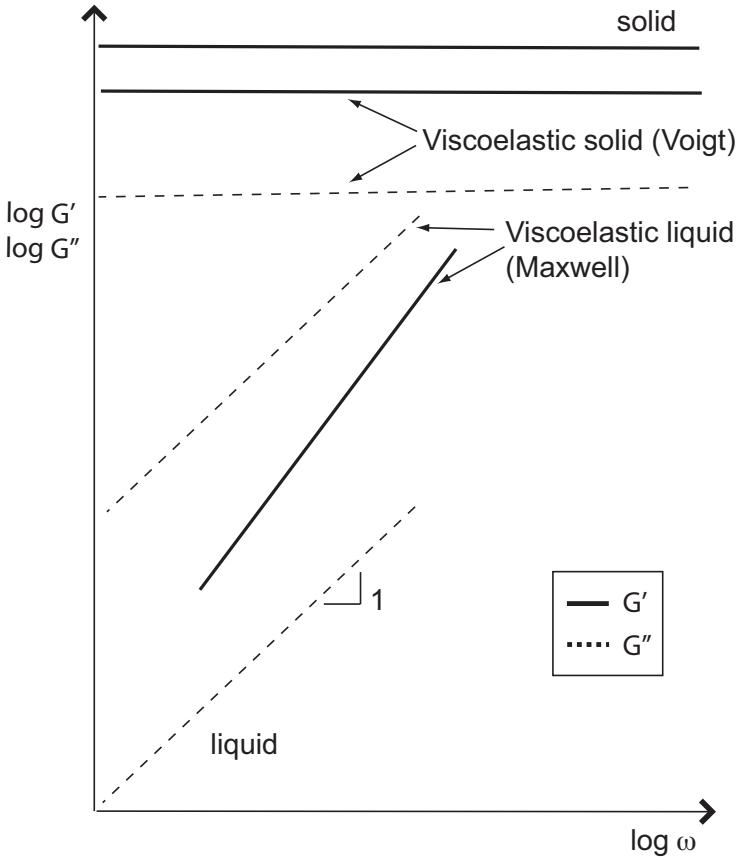

Figure 2.8: Schematic illustration of frequency-dependent shear moduli for prototypical liquids, solids, viscoelastic solids described by Voigt model, and viscoelastic liquids described by the Maxwell model.

2.3 Microrheology

Instead of using macroscopically applied and detected stress and strain to extract a material's moduli, microrheology relies on detecting the displacement of colloidal probe particles embedded in the material to extract similar quantities. These probe displacements can be excited either by broadband thermal energy (i.e. k_BT) or by externally imposed forces (e.g. via magnetic or optical tweezers). The former is termed *passive microrheology*, while the latter is termed *active microrheology*.

2.3.1 The Stokes-Einstein relation

Consider, as Einstein did circa 1905, a particle diffusing in a Newtonian fluid. In thermal equilibrium, collisions of the particle with the molecules in the fluid gives rise to Brownian motion which can be quantified by the particle's mean square displacement (MSD):

$$\langle \Delta x^2(\tau) \rangle = \langle [x(t_0 + \tau) - x(t_0)]^2 \rangle. \tag{2.30}$$

Here $x(t)$ is one omponent of the position of the particle at time t, τ is the lag time, and $\langle\rangle$ denotes time averaging over all initial times t_0 for a single particle or, alternatively, both time and ensemble averaging for a collection of particles.

For a spherical particle with radius a diffusing in a Newtonian liquid of viscosity η, the particle's MSD is related to the diffusivity D via $\langle \Delta x^2(\tau) \rangle = 2D\tau$ where

$$D = \frac{k_BT}{6\pi\eta a}. \tag{2.31}$$

Eq. (2.31) is known as the Stokes-Einstein relation and is the theoretical cornerstone of all passive microrheology measurements. It asserts that measurements of a particle's thermally excited diffusivity can be used to extract the viscosity of the fluid, thus relating an embedded tracer particle's dynamics with the medium's rheology. Owing to the importance of the Stokes-Einstein relation in microrheology, it is useful to derive Eq. 2.31 from first principles. In order to do so, it is instructive to break the derivation down into two steps and critically examine the assumptions underlying each of the steps. The first step is to view Eq. 2.31 as a statement that a stochastic quantity (D) is related to the temperature times a deterministic material quantity (M), i.e. $D = k_B T M$, where $M = 1/6\pi\eta a$. M is called the particle mobility. This is the "Einstein" part of "Stokes-Einstein" due to the fact that it was Einstein who first considered it in 1905.

The second step is relating the particle's mobility (M) to the medium's viscosity. M is a deterministic material property that relates the velocity (v) of a particle embedded in the medium to the force (F) applied to it via $v = M \cdot F$. The hydrodynamic calculation yields $M = 1/6\pi\eta a$ for a spherical particle of radius a translating with velocity v in a Newtonian fluid with viscosity η. This result, first carried out by Stokes in 1851, comprises the "Stokes" part of "Stokes-Einstein".

Finally, note that Eq. 2.31 is contains a constant (i.e. frequency/time-independent) viscosity. However, it is clear from the preceding sections that most soft materials are viscoelastic, and hence frequency-dependent moduli are necessary to describe their rheological response. Thus, the final step will be to generalize the Stokes-Einstein relation to frequency- dependent material properties.

2.3.2 Einstein Component: relating diffusivity to mobility

The phenomena connected most directly with Brownian motion is diffusion: an ensemble of small particles placed at a point in space will spread out in time, diffusing via Brownian motion. Consider a collection of particles diffusing in one-dimension. Let $c(x,t)$ be the concentration at x and t. The process of diffusion is phenomenologically described by Fick's Law, which states that if the concentration is not uniform, there will be a flux $j(x,t)$ which is proportional to the spatial gradient of the concentration, i.e.,

$$j(x,t) = -D\frac{\partial c}{\partial x}, \tag{2.32}$$

where D is the diffusivity, or diffusion constant. Owing to the minus sign on the right hand side of Eq. 2.32, the flux of particles will always be from higher concentration regions to lower concentration regions. Stated another way, in equilibrium, the flux is zero; whereas if the system is driven out of equilibrium the flux acts to restore equilibrium. If there is an external potential $U(x)$ acting on the particles, then Fick's Law must be modified. The potential exerts a force

$$F = -\frac{\partial U}{\partial x} \tag{2.33}$$

on the particles producing in a non-vanishing mean particle velocity v which, assuming the force is weak, is linearly related to F via

$$v = M \cdot F = -M \cdot \frac{\partial U}{\partial x}, \tag{2.34}$$

where M is the particle mobility. The average velocity of the particles in response to the external

potential gives rise to an additional flux cv which must be added to Eq. 2.32, such that the total flux will be

$$j(x,t) = -D\frac{\partial c}{\partial x} - c(M \cdot \frac{\partial U}{\partial x}). \tag{2.35}$$

In equilibrium, the concentration $c(x,t)$ is independent of time and is given by the Boltzmann distribution

$$c_{eq}(x) \propto \exp(-U(x)/k_B T). \tag{2.36}$$

Detailed balance requires the net flux to vanish in equilibrium

$$j(x,t) = -D\frac{\partial}{\partial x}c_{eq} - Mc_{eq}\frac{\partial U}{\partial x} = 0, \tag{2.37}$$

so that substituting Eq. 2.36 into Eq. 2.37 yields

$$D = k_B T M. \tag{2.38}$$

This expression is commonly known as the Einstein relation. It relates a stochastic fluctuating quantity (diffusivity) to a deterministic mechanical property (mobility).

2.3.3 Stokes Component: relating particle mobility to material rheology

The functional form of M for a spherical particle of radius a steadily translating in a Newtonian fluid was obtained by Stokes in 1851. For low-Reynolds number flows, where viscous damping dominates inertial effects, the Navier-Stokes equations as applied to fluid phases reduce to

$$\eta \nabla^2 \vec{u} = \vec{\nabla} p,$$

$$\vec{\nabla} \cdot \vec{u} = 0. \tag{2.39}$$

Here $\vec{u}$ is the local velocity field of the incompressible flow far away from sources and sinks and p is the local pressure. Eqns 2.39 are known as the Stokes equations and can be readily solved for $\vec{u}, p$ by considering appropriate boundary conditions for the fluid at the the probe particle surface (no-slip) and at infinity (bounded) to relate the probe mobility to the viscosity of the medium.

Once solved for, the velocity field $\vec{u}$ and pressure p can be used to determine the stress tensor $\sigma_{\alpha\beta}$ via

$$\sigma_{\alpha\beta} = -p\delta_{\alpha\beta} + \eta(\nabla_\alpha u_\beta + \nabla_\beta u_\alpha). \tag{2.40}$$

Finally, the viscous drag on the particle is given by integrating Eq. 2.40 over the particle surface:

$$F_\alpha = \int_S \sigma_{\alpha\beta} dS_\beta. \tag{2.41}$$

For a sphere of radius a translating through a fluid of viscosity η at constant velocity $\vec{v} = v\hat{z}$, Eqns. 2.39 yield the solutions:

$$\frac{u_\alpha(\hat{r})}{v} = \frac{3}{4}a\left(\frac{\delta_{\alpha z}}{r} + \frac{z r_\alpha}{r^3}\right) + \frac{1}{4}a^3\left(\frac{\delta_{\alpha z}}{r^3} - \frac{3 z r_\alpha}{r^5}\right), \tag{2.42}$$

where $\vec{r}$ is the distance from the sphere's center and z is the displacement along the sphere's direction of motion. The pressure is given by

$$p(\vec{r}) = \frac{3}{2}\eta a \frac{\vec{r}\cdot\vec{v}}{r^3}. \tag{2.43}$$

Substituting Eqns. 2.42 - 2.43 into Eqns. 2.40 - 2.41 and solving for the viscous drag ζ via $\vec{F} = \zeta\vec{v}$, we obtain $\zeta = 6\pi\eta a$. The Stokes mobility is thus

$$M = \zeta^{-1} = (6\pi\eta a)^{-1}. \tag{2.44}$$

The ηa combination could have been guessed from simple dimensional analysis of the drag force. However the "6π" prefactor is a direct consequence of the no-slip boundary condition for the fluid velocity field on the sphere's surface. Interestingly, relaxation of the no-slip boundary condition, e.g., as in the case of a deformable bubble, results in a prefactor value of "4π". Combining Eq. 2.44 with Eq. 2.38 yields the Stokes-Einstein relation, Eq. 2.31.

2.3.4 Generalized Stokes-Einstein Relation

The first assumption in the generalization of the Stokes mobility is that it adopts the same functional form at all frequencies:

$$M^*(\omega) = \frac{\eta_0}{\eta^*(\omega)} M = (6\pi\eta^*(\omega)a)^{-1}, \tag{2.45}$$

i.e., simply replace η_0 with $\eta^*(\omega)$. The basis for this assumption can be found in the underlying linearity of Eqns. 2.39 which, when solved in the non-inertial regime, admit viscous and

viscoelastic solutions exhibiting isomorphic correspondence [119]. With this assumption, Mason and Weitz [70], derived the relationship between the probe MSD and frequency-dependent mobility starting from the Langevin equation:

$$m\dot{V}(t) = f_R(t) - \int_0^t \zeta(t-t')V(t')dt', \tag{2.46}$$

describing the dynamics of a spherical particle subject to a weak random force $f_R(t)$ in an isotropic linear viscoelastic material. Here m and V are the mass and velocity of the probe particle, respectively. $\zeta(t-t')$ is the time-dependent hydrodynamic resistance, defined via $F_H(t) = \int_{-\infty}^{t} \zeta(t-t')V(t')dt'$ whose Laplace transform is the inverse of the mobility $\tilde{\zeta}(s) = \tilde{M}(s)^{-1}$. Taking the Laplace transform of Eq. (2.46) and solving for $\tilde{V}(s)$ yields

$$\tilde{V}(s) = \frac{mV(0) + \tilde{f}_R(s)}{ms + \tilde{\zeta}(s)}, \tag{2.47}$$

where $\tilde{V}(s)$ denotes the Laplace transform of $V(t)$ and s is the Laplace frequency. Because f_R is a stochastic quantity, $V(t)$ must be treated statistically. Multiplying Eq. (2.47) by $V(t=0)$ and ensemble averaging gives

$$\langle V(0)\tilde{V}(s)\rangle = \frac{m\langle V(0)^2\rangle + \langle V(0)\tilde{f}_R(s)\rangle}{ms + \tilde{\zeta}(s)}. \tag{2.48}$$

Assuming that the random force is uncorrelated with the velocity: $\langle f_R V\rangle = 0$ and equipartition: $\frac{1}{2}m\langle V(0)^2\rangle = \frac{1}{2}k_BT$, the Laplace transform of the velocity autocorrelation for d-dimensional probe motion is thus

$$\langle V(0)\tilde{V}(s)\rangle = \frac{dk_BT}{ms+\tilde{\zeta}(s)}. \tag{2.49}$$

If the frequency is low enough that the resistance $\tilde{\zeta}(s)$ dominates over the probe inertia ms (typically $<$ MHz for colloidal systems), then

$$\langle V(0)\tilde{V}(s)\rangle \approx dk_BT\tilde{\zeta}^{-1}(s) = dk_BT\tilde{M}(s). \tag{2.50}$$

The neglect of inertia will be addressed in a later subsection. Finally the Laplace transform of the velocity autocorrelation can be related to the MSD via the identity

$$\langle V(0)\tilde{V}(s)\rangle = \frac{s^2}{2}\mathscr{L}\langle\Delta\mathbf{r}^2(t)\rangle \equiv \frac{s^2}{2}\langle\Delta\tilde{\mathbf{r}}^2(s)\rangle, \tag{2.51}$$

where $\mathscr{L}$ denotes Laplace transformation, to give

$$\langle\Delta\tilde{\mathbf{r}}^2(s)\rangle \approx \frac{2dk_BT}{s^2\tilde{\zeta}(s)} \equiv \frac{2dk_BT}{s^2}\tilde{M}(s), \tag{2.52}$$

or

$$\tilde{M}(s) \approx \frac{s^2\langle\Delta\tilde{\mathbf{r}}^2(s)\rangle}{2dk_BT}. \tag{2.53}$$

Eq. 2.53 is more commonly written in terms of the frequency dependent shear modulus $\tilde{G}(s)$ which is related to the probe mobility $\tilde{M}(s)$ via $\tilde{M}(s) = (6\pi a\frac{\tilde{G}(s)}{s})^{-1}$. The resulting expression is known as the Generalized Stokes-Einstein Relation (GSER):

$$\langle \Delta \tilde{r}^2(s) \rangle = \frac{dk_B T}{3\pi a s \tilde{G}(s)}. \tag{2.54}$$

The GSER is the basis for all passive (thermal) microrheology. It states that the Laplace transform of the probes' MSD is related to the Laplace transform of the shear modulus of the medium. An equivalent representation of Eq. 2.54 in terms of the Fourier components, more commonly encountered in oscillatory macrorheological data, can be readily obtained via analytic continuation $s = i\omega$. In practice, the Laplace or Fourier transformed MSD is typically not obtained directly from the time-domain data since the dynamic range is limited to a few decades in conventional measurement schemes. Instead, local power laws are used to approximate the time-domain MSD and the transforms are generated via algebraic expressions based on the values of the power law exponents. More details of this procedure will be given in Section 3.3.6.

An alternate but, equivalent approach was used by Gittes et. al. [40] and Schnurr et. al. [93] in their data analysis. Their experiments involved optically trapping of the probe particle and thus the introduction of an additional force term into Eq. 2.46 which is more naturally analyzed via the linear response function. The linear response function $\alpha(t)$ relates the probe's displacement $r(t)$ to a weak applied force $F(t)$ is defined via the relation

$$r(t) - r(0) = \int_0^t \alpha(t-\tau) F(\tau) d\tau. \tag{2.55}$$

Taking the Fourier transform of this equation yields

$$r(\omega) = \alpha(\omega)F(\omega). \tag{2.56}$$

The Fluctuation-Dissipation Theorem (FDT) relates the power spectrum of the probe's displacement $S(\omega) = \langle \Delta r(\omega) \Delta r(-\omega) \rangle$ to the imaginary part of the Fourier transform of the linear response function:

$$S(\omega) = \frac{2dk_BT}{\omega}\alpha''(\omega). \tag{2.57}$$

Once $\alpha''(\omega)$ is obtained, the Kramers-Kronig relations can be used to obtain the real part $\alpha'(\omega)$ from the imaginary part [16]. The power spectrum represents the informational endpoint for microrheology of systems in thermal equilibrium, since it is equivalent to a measurement of the response function as Eq. 2.57 attests. Eq. 2.57 is identical to Eq. 2.53, provided the substitution $s = i\omega$ and identity $\alpha^*(\omega) = M^*(\omega)/(i\omega)$ are made. A table summarizing the connections between quantities measured in macroscopic linear rheology and probe dynamics measured in microrheology is given in Table 2.1.

Property	**Symbol**	**Relation**
Linear shear rheology		
Shear relaxation modulus	$G(t)$	$\sigma(t) = \int_0^t G(t-t')\gamma(t')dt'$
Complex shear modulus	$G^*(\omega)$	$\sigma(\omega) = G^*(\omega)\gamma(\omega)$
Complex viscosity	$\eta^*(\omega)$	$G^*(\omega) = -i\omega\eta^*(\omega)$
Creep Compliance	$J(t)$	$i\omega J^*(\omega) = 1/G^*(\omega)$
Local probe response		
Probe Mobility	$M(t)$	$V(t) = \int_0^t M(t-t')F(t')dt'$
Probe resistance	$\zeta(t)$	$F(t) = \int_0^t \zeta(t-t')V(t')dt'$
	$\tilde{\zeta}(s) = \tilde{M}^{-1}(s)$	
Linear response function	$\alpha^*(\omega)$	$M^*(\omega) = i\omega\alpha^*(\omega)$
Probe statistics		
Mean square displacement	$\langle \Delta r^2(t) \rangle$	$\langle \Delta \tilde{r}^2(s) \rangle = \frac{dk_BT}{3\pi as\tilde{G}(s)}$
Positional Autocorrelation	$\langle r(t)r(0) \rangle$	$\langle \Delta r^2(t) \rangle = 2 - 2\langle r(t)r(0) \rangle$
Power Spectrum	$S(\omega) = \langle \Delta r(-\omega)\Delta r(\omega) \rangle$	$S(\omega) = \frac{2dk_BT}{\omega}\alpha''(\omega)$
Two-Point MSD (MSD2)	$MSD2 = \frac{2R}{a}\langle \Delta r_1(t)\Delta r_2(t) \rangle$	$MSD2 = \langle \Delta r^2(t) \rangle$ for homog.

Table 2.1: Relations between properties measured in macroscopic linear rheology and probe dynamics in microrheology. Adapted from Ref. [99].

2.3.5 One-point Microrheology

One-point passive microrheology uses the generalized Stokes-Einstein equation (GSER),

$$\langle \Delta \tilde{r}^2(s) \rangle = \frac{k_B T}{\pi a s \tilde{G}_1(s)}, \tag{2.58}$$

to determine the single-particle shear modulus $\tilde{G}_1(s)$ from the measured single-particle mean-square displacement, $\langle \Delta r^2(\tau) \rangle = MSD1$ [70]. Here $\Delta \tilde{r}^2(s)$ is the Laplace transform of $\Delta r^2(\tau)$ as a function of Laplace frequency s, a is the particle radius, and $k_B T$ is the thermal energy. Eq. (2.58) is the familiar Stokes-Einstein relation generalized to a frequency-dependent viscosity, $\tilde{\eta}(s) = s\tilde{G}_1(s)$. Shear moduli and $MSD1$ may be readily converted between the Fourier, Laplace and lag time domains with simple numerical routines [70]. We will discuss the approximations used to convert the MSD in more detail in Chapter 3. The GSER accurately provides the experimenter with the background medium's complex shear modulus, $G^*_{bulk}(\omega) = G'(\omega) + i\,G''(\omega)$ when the medium is homogeneous on the scale of a. When the sample is heterogeneous, this standard GSER relation can lead to significantly underestimated shear moduli [59, 61].

2.3.6 Limits of the GSER

The validity of one-point microrheology using the GSER to provide an accurate measure of the complex shear modulus $G^*(\omega)$, for even simple homogeneous systems, to say nothing of real complex materials, was far from certain prior to the year 2000. There were two main sources of uncertainty. The first concerned the frequencies over which the GSER of Eq. 2.58 was valid. Theoretical work by Levine and Lubensky [59, 60] showed that there exists a certain frequency

range, $\omega_c < \omega < \omega_i$, within which the probe particles' dynamics provide an accurate measure of $G^*(\omega)$ as measured in bulk rheology. The lower limit, ω_c, is the frequency at which compressional modes become significant compared to the shear modes that are excited in a polymeric network. In bulk rheology, the applied strain has only a shear component, whereas the thermally driven probe particle responds to all of the thermally excited modes of the system, including the compressional modes of the elastic network. Consequently, the GSER would measure a different $G^*(\omega)$ than bulk rheology. At frequencies lower than ω_c the network compresses and fluid drains from denser regions of the network to more rarefied regions in a sponge-like manner. Above ω_c, the network "locks in" with the incompressible fluid with the result that compressional modes are suppressed. Consequently, the GSER should measure the same $G^*(\omega)$ as bulk rheology. An estimate of the lower crossover frequency, ω_c, can be determined by balancing local viscous and elastic forces. The viscous force per unit volume exerted by the solvent on the network is $\sim \eta v/\xi^2$, where v is the velocity of the fluid relative to the network, η is the viscosity of the fluid, and ξ is the mesh size of the network. The local elastic force per unit volume exerted by the network is $G'\nabla^2 u \sim G'u/a^2$ at the bead surface where u is the network displacement field and a is the radius of the bead. Force balance dictates that viscous coupling between the fluid and network will occur when $\eta v/\xi^2 > G'u/a^2$, leading to a crossover frequency

$$\omega_c \geq \frac{G'\xi^2}{\eta a^2}. \tag{2.59}$$

For typical soft materials studied using passive microrheology, $G' \approx 0.1\,Pa$, $\eta \approx .001 Pa\,s$, and $\xi \approx 0.1\,a$ this leads to $\omega_c \approx 1Hz$.

The upper limit, ω_i, is the frequency at which inertial effects set in at the length scale of

the bead. Recall that one of the assumptions in the derivation of the GSER in Eq. 2.54 was the neglect of inertia. Shear waves propagated by the motion of the tracer decay exponentially from the surface of the bead through the surrounding medium. The characteristic length scale of the decay is called the viscous penetration depth and is proportional to $\sqrt{G/\rho\omega^2}$ where ρ is the density of the surrounding fluid and ω is the frequency of the shear wave [36, 60]. When the viscous penetration depth becomes comparable to the size of the bead, inertial effects become significant and cannot be neglected. For a particle of of radius a, this occurs at a frequency given by

$$\omega_i = \sqrt{\frac{G}{\rho a^2}}. \tag{2.60}$$

For typical soft materials studied using passive microrheology, $G \approx 0.1\,Pa$, $\rho \approx 1000\,kg/m^3$, and $a \approx 0.5\,\mu m$ this leads to $\omega_i \approx$ 20 kHz. Note that this is much higher than in macrorheological measurements where a viscous penetration depth of $O(mm)$ leads to the onset of inertial effects at $\sim$ 50 Hz. From these analyses, we find under typical conditions a large frequency range $1Hz < \omega <$ 20 kHz where the GSER accurately measures the shear modulus..

The second source of uncertainty concerned local inhomogeneities in the sample induced by the presence of the probe particles. Consider the situation sketched in Figure 2.9. If the tracers locally modify the structure of the medium, or sample only pores in an inhomogeneous matrix, then bulk rheological properties will not be determined. Such subtle effects called into question the widespread applicability of colloidal probe based microrheology. Along with knowledge about sample homogeneity, the proper interpretation of all microrheology methods also relies on knowing the boundary conditions at the probe/soft material interface and the shape of the strain

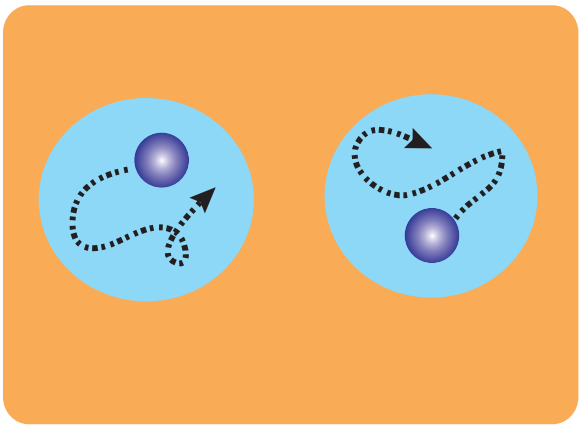

Figure 2.9: Schematic of situation in which particles are embedded in pores with a different compliance than the bulk material.

field, which can be poorly controlled compared to a macroscopic rheometer.

Two-point microrheology (TPM) [26] uses the correlated motion of two well separated tracers to measure the rheological response, with the effect that the measurement becomes insensitive to tracer boundary conditions [59, 61]. This robustness can be turned around to study the nature of the probe boundary conditions with the matrix [18, 100] and even inertial effects [9]. While much early TPM work used an image-based passive approach, it has been adapted to dynamic light scattering [83] and optical tweezer-based instruments [53].

2.3.7 Two-point Microrheology

Particles immersed in a fluid excite long-ranged flows as they move, and similarly move in response to fluid motion. By generating and reacting to a fluid's local velocity, colloidal particles experience hydrodynamic interactions with each other and with the walls of their container. These interactions, in turn, are dominated by the large-scale 'bulk' properties of the medium rather than 'local' regions surrounding the tracers that may arise due to sample inhomogeneity or boundary effects at the particle-material interface. Two-point microrheology takes advantage

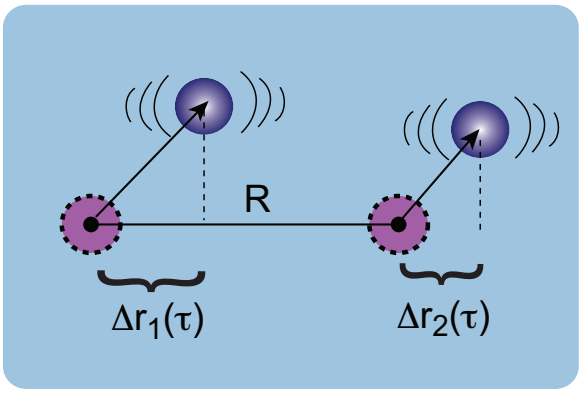

Figure 2.10: Schematic of two-point displacement component. In this depiction the longitudinal component $D_{rr} = \langle \Delta r_1(\tau) \Delta r_2(\tau) \rangle$ is the product of the displacement component projected along the line separating the tracers by distance R, with $R \gg a$ ideally.

of the interparticle coupling to robustly extract bulk material properties in the face of these potentially confounding influences.

Two-point microrheology is based on cross-correlating the equal-time displacements of pairs of tracers. Ensemble and time averaging such products over all trajectory pairs yields a mobility correlation tensor, $D_{\alpha\beta}$, that reports the degree of correlation between the tracers' random motion during lag time τ versus their separation R:

$$D_{\alpha\beta}(r,\tau) = \langle \Delta r^i_\alpha(t,\tau) \Delta r^j_\beta(t,\tau) \delta[r - R^{ij}(t)] \rangle_{i \neq j,t}, \tag{2.61}$$

where i and j denote different particles, α and β denote different coordinates, and R^{ij} is the distance between the distinct particles i and j. Spatially, $D_{\alpha\beta}(r,\tau)$ can be decomposed into a longitudinal D_{rr} and transverse $D_\perp$ components, where the former is the component of the motion along the center-to-center separation vector of the two tracers (depicted in Figure 2.10), while the latter two are the components orthogonal to the separation vector. To lowest order in

a/R, the off-diagonal components (e.g. $D_{r\perp}$) are negligible relative to these. For an incompressible medium, the amplitudes are related via

$$D_{\perp} = \frac{1}{2} D_{rr}, \tag{2.62}$$

Typically, D_{rr} is the strongest component and hence easiest to measure in experiments from a signal-to-noise perspective. Moreover, to lowest order in a/R, D_{rr} depends only on the shear modulus of the medium [59, 61]. By contrast, the $D_{\perp}$ terms have, to lowest order in a/R, dependencies on the bulk modulus as well. This dependency can be turned around to measure frequency- and lengthscale-dependent compressibility using microrheology via the ratio $\frac{D_{\perp}}{D_{rr}} \leq \frac{1}{2}$ ($= \frac{1}{2}$ for an incompressible medium). Accordingly, the shear modulus may be determined using the relation

$$\tilde{D}_{rr}(R, s) = \frac{k_B T}{2\pi R s \tilde{G}(s)}, \tag{2.63}$$

where $\tilde{D}_{rr}(R, s)$ is the temporal Laplace transform of $D_{rr}(R, \tau)$. It is instructive to derive Eq. 2.63 using the Oseen tensor analysis utilized in Ref. [71]. The overdamped Langevin equation with pairwise hydrodynamic coupling yields the equations of motion for a collection of N particles:

$$\mathbf{v}_i(t) = \sum_{j=0}^{N} \mathbf{H}_{ij}(\mathbf{r}_i - \mathbf{r}_j)\mathbf{f}_j(t) + \eta_i, \tag{2.64}$$

here the velocity of a particle is the sum of both self ($i = j$) and distinct ($i \neq j$) terms representing hydrodynamic coupling to deterministic external forces $\mathbf{f}_i(t)$ and stochastic noise $\eta_i(t)$. The

hydrodynamic mobility tensor, $\mathbf{H}_{ij}$, is the Oseen tensor and has the components:

$$\mathbf{H}_{ii}(\mathbf{R}) = \frac{\mathbf{I}}{\zeta},\ \mathbf{H}_{ij}(\mathbf{R}) = \frac{1}{8\pi\eta R}(\mathbf{I} + \hat{\mathbf{r}}\hat{\mathbf{r}}), \tag{2.65}$$

where $\zeta = 6\pi\eta a$ is the Stokes drag of a sphere of radius a in a Newtonian liquid of viscosity η, $\mathbf{I}$ denotes the $d \times d$-dimensional identity matrix, $\hat{\mathbf{r}}$ is a unit vector along the vector connecting the centers of two particles separated by distance R. Eq. 2.65 is derived from solving the Stokes equations and is essentially a Green's function for a point force solution [32, 88]. It is apparent from Eq. 2.65 that interparticle coupling does not depend on the radius of the particles. The elements of the Oseen tensor in Eq. 2.65 are the leading order components ($O(a/R)$). The next-to-leading order components are $O[(a/R)^4]$ for the diagonal elements and $O[(a/R)^3]$ for the off-diagonal elements [11]. Brownian forces are represented by the stochastic noise term $\eta_i(t)$ and satisfy the statistical properties:

$$\langle \eta_i(t) \rangle = 0,\ \langle \eta_i(t)\eta_j(t') \rangle = 2k_B T \mathbf{H}_{ij}(\mathbf{r}_i - \mathbf{r}_j)\delta(t - t'). \tag{2.66}$$

Eq. 2.66 assumes that the random forces are consistent with Gaussian white noise with zero mean and also with the FDT. Explicitly, for two particles 1 and 2, Eq. 2.64 yields the coupled equations:

$$\begin{aligned} \mathbf{v}_1(t) &= \mathbf{H}_{11}\mathbf{f}_1(t) + \mathbf{H}_{12}\mathbf{f}_2(t) + \eta_1(t) \\ \mathbf{v}_2(t) &= \mathbf{H}_{21}\mathbf{f}_1(t) + \mathbf{H}_{22}\mathbf{f}_2(t) + \eta_2(t) \end{aligned} . \tag{2.67}$$

In the absence of external forces $\mathbf{f}_1(t) = \mathbf{f}_2(t) = 0$, Eqns. 2.67 reduce to $\mathbf{v}_i(t) = \eta_i(t)$. Computing the ensemble average of the cross-correlation $\langle \mathbf{v}_1(t)\mathbf{v}_2(t') \rangle$ yields

$$\begin{aligned}\langle v_1(t)v_2(t')\rangle &= \langle \eta_1(t)\eta_2(t')\rangle \\ &= 2k_BT\mathbf{H}_{12}(\mathbf{r}_1-\mathbf{r}_2)\delta(t-t') \\ &= \frac{k_BT}{4\pi\eta R}\langle \mathbf{I}+\hat{\mathbf{r}}\hat{\mathbf{r}}\rangle\delta(\mathbf{t}-\mathbf{t}') \\ &= \frac{k_BT}{2\pi\eta R}\delta(t-t'). \end{aligned} \tag{2.68}$$

Taking the Laplace transform of Eq. 2.68 and using the identity $\langle \tilde{v}_1(s)\tilde{v}_2(s)\rangle = s^2\langle \Delta\tilde{r}_1(s)\Delta\tilde{r}_2(s)\rangle = s^2\tilde{D}_{rr}(R,s)$ and the frequency generalization $\tilde{\eta}(s) = \tilde{G}(s)s^{-1}$ yields Eq. 2.63 . Significantly, Eq. 2.63 has no explicit dependence on a, suggesting that it is independent of the tracer's size, shape and boundary conditions with the medium in the limit $R \gg a$. This is the signal advantage of two-point measurements that has enabled it to surmount the inhomogeneity issue that limited 'blind' application of the GSER in microrheology. Eq. 2.63 can be rendered identical to the one-point GSER in Eq. 2.58, provided the identification

$$\langle \Delta\tilde{r}^2(s)\rangle = \frac{2R}{a}\tilde{D}_{rr}(R,s), \tag{2.69}$$

is made. Eq. 2.69 suggests that a two-point MSD (MSD2) can be defined from the $D_{rr}(R,\tau)$ component, by mulitplying by a geometric prefactor $2R/a$:

$$\langle \Delta r^2(\tau)\rangle_2 = \frac{2R}{a}D_{rr}(R,\tau), \tag{2.70}$$

Eq. 2.70 represents the MSD of a tracer in a medium in which affine extrapolation of the large-scale strain field down to the particle length scale is valid. If the material is homogeneous, isotropic on length scales significantly smaller than the tracer, incompressible, and connected to the tracers by uniform no-slip boundary conditions over their entire surfaces, then the two MSDs will be equal $\langle \Delta r^2(\tau) \rangle_2 = \langle \Delta r^2(\tau) \rangle$. If these boundary and homogeneity conditions are not satisfied, the two MSDs will be unequal. In this case, using the MSD2 in the GSER will still yield the "bulk" rheology of the material (on the long length scale "R"), while using the MSD1 will report a rheology that is a complicated superposition of the bulk rheology and the local rheology of the material at the tracer boundary [59, 61]. We will discuss this in more detail in the next section.

2.3.8 Electrostatic Analogy

The introduction of particles into an otherwise homogeneous medium can perturb the medium out to a radius larger than the particle size as shown in Figure 2.11. This perturbation can be a result of a reduction of density of the material near the particle's surface, as in the case of depletion. This density reduction leads to a spatially inhomogeneous elastic constant tensor $K_{ijkl}(\mathbf{x}, \omega)$. Assuming that the stress-strain relation remains local, the equation for displacement variables is

$$-\partial_j [K_{ijkl}(\mathbf{x}, \omega) \partial_{\mathbf{k}} \mathbf{u_l}] = \mathbf{f_i}(\mathbf{x}, \omega), \tag{2.71}$$

where $f_i(\mathbf{x}, \omega)$ is the force density that acts on the surface of the particles. The displacement responses of the collection of particles to forces upon them can be described by the two-particle

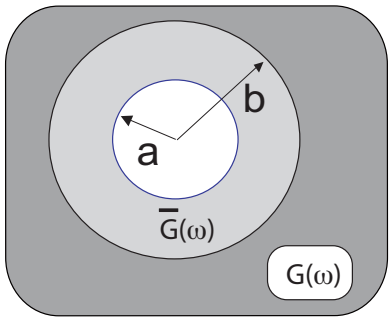

Figure 2.11: Schematic of a particle of radius a embedded in a viscoelastic medium with shear modulus $G(\omega)$. The presence of the particle perturbs the medium out to a spherical pocket of radius b with a modified shear modulus $\overline{G}(\omega)$.

response function or compliance tensor $\alpha_{ij}^{(nm)}$:

$$R_i^n(\omega) = \alpha_{ij}^{(nm)}(\mathbf{r^n} - \mathbf{r^m}, \omega)\mathbf{F_j^m}(\omega), \tag{2.72}$$

where R_i^n is the displacement vector of nth particle and F_j^m is the force on the mth particle. The central question is whether the self components of the compliance tensor $\alpha_{ij}^{(nn)}$ have a different dependence on the bead imposed heterogeneities of $K_{ijkl}(\mathbf{x}, \omega)$ than the distinct components $\alpha_{ij}^{(nm)}$ do. If so, then it will be possible to distinguish the bulk homogeneous part from the local bead imposed part by measuring the different components of $\alpha_{ij}^{(nm)}$.

In order to address this question, Levine and Lubensky [59,61] made an analogy to a simpler, but related, problem encountered in electrostatics, that of determining the bulk dielectric constant of a medium by measuring the self- and mutual- capacitances of metal spheres whose presence perturbs the dielectric constant in their vicinity. If the dielectric constant, $\epsilon(\mathbf{x}, \omega)$, remains local, then the potential, $\phi(\mathbf{x}, \omega)$, satisfies

$$-\nabla \cdot [\epsilon(\mathbf{x}, \omega)\nabla\phi(\mathbf{x}, \omega)] = \mathbf{4}\pi\rho(\mathbf{x}), \tag{2.73}$$

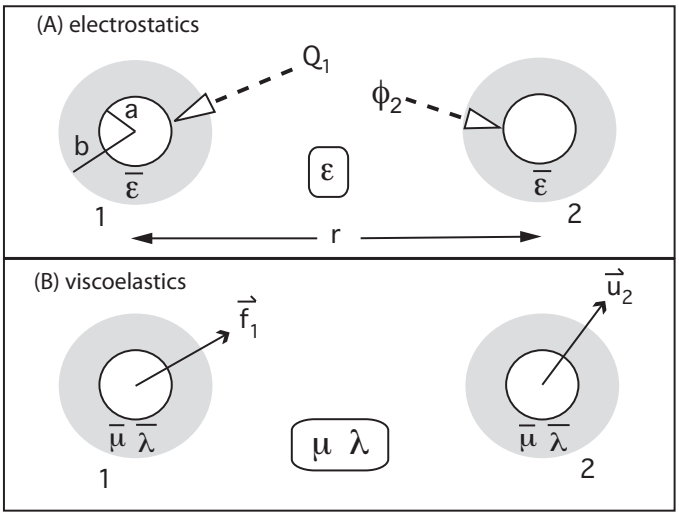

Figure 2.12: (A) Schematic of electrostatic system in which conducting sphere of radius a perturb an otherwise uniform medium of dielectric constant ϵ out to a radius b with dielectric constant $\overline{\epsilon}$. (B) Similar schematic of elastic system in which rigid spheres perturb an elastic medium with Lamé coefficients $\mu,\ \lambda$ out to a spherical region with Lamé coefficients $\overline{\mu},\ \overline{\lambda}$. Adapted from Fig. 1 of Ref. [59].

where $\rho(\mathbf{x})$ is the charge density at $\mathbf{x}$. It is clear from the structure of Eq. 2.71 and Eq. 2.73 that there is an analogy between the electrical and rheological problems with the identification: $\phi \longleftrightarrow \mathbf{u}$, $\epsilon \longleftrightarrow K_{ijkl}$, and $\rho \longleftrightarrow \mathbf{f}$. Thus, solving the simpler electrostatic problem for these quantities will yield insight into the complementary quantities in the elastic problem. For example, the total charge Q on a metal sphere is the analog of the total force $\mathbf{F}$ on a bead in the viscoelastic medium. The inverse capacitance tensor C^{-1}_{nm} defined by

$$\phi_n = C^{-1}_{nm} Q_m, , \tag{2.74}$$

where ϕ_n is the potential on bead n and Q_m is the total charge on bead m, is the analog of the compliance tensor: $C^{-1}_{nm} \longleftrightarrow \alpha^{(nm)}_{ij}(\omega)$. This electrostatic analogy is illustrated in Figure 2.12

and summarized in Table 2.2.

Electrostatics	**Viscoelastics**
Potential $\phi(\mathbf{x})$	Displacement $u_i(\mathbf{x})$
Charge Density $\rho(\mathbf{x})$	Force density $f_i(\mathbf{x})$
Dielectric tensor $\epsilon_{ij}(\mathbf{x},\omega)$	Elastic tensor $K_{ijkl}(\mathbf{x},\omega)$
Inverse capacitance tensor C^{-1}_{nm}	Compliance tensor $\alpha^{(nm)}_{ij}(\omega)$

Table 2.2: Correspondence between electrostatics and viscoelastics.

To solve Eq. 2.74 for C^{-1}_{ij}, the method of images can be used to iteratively fix the potential ($\phi = const$) on each conducting sphere induced by the charge from the other spheres and from induced charges in its own cavity. The resulting convergent series may be truncated at the lowest order in reflections. In general, each higher order of reflection leads to a multiplicative factor of a/r or b/r in the series, which become negligible in the limit of interest $a/r \longrightarrow 0$. Levine and Lubensky found that to lowest order in a/r, the inverse self-capacitance is

$$C^{-1}_{11} = \frac{1}{4\pi\epsilon a}\left[1 + \left(\frac{b}{a} - 1\right)\left(1 - \frac{\epsilon}{\overline{\epsilon}}\right)\right]. \tag{2.75}$$

This result shows that fluctuations of a single bead are sensitive to both the local dielectric constant ($\overline{\epsilon}$) and bulk dielectric constant (ϵ) around the bead and therefore do not permit an unambiguous determination of the bulk dielectric constant ϵ. On the other hand, the inverse mutual capacitance

$$C^{-1}_{12} = \frac{1}{4\pi\epsilon r}\left[1 + O\left(\frac{a}{r}\right)\right], \tag{2.76}$$

depends only on the bulk dielectric constant to leading order in a/r. Thus correlated voltage

fluctuations, $\langle \phi_1(\omega)\phi_2(-\omega)\rangle = 2(T/\omega)\mathrm{Im}C_{12}^{-1}(\omega)$, yield a direct measurement of $\epsilon(\omega)$ provided the beads are far enough apart that $C_{12}^{-1} \sim 1/r$. Based on these results for the electrostatic problem, it is expected that similar dependencies will be found for the two-particle response tensor $\alpha_{ij}^{(nm)}$. The calculation is more complicated in the elastic problem since the displacement field, the quantity analogous to the potential, has more components and hence more boundary conditions at the interfaces. Nonetheless, carrying out a similar analysis for the elastic problem, Levine and Lubensky [61] find for the self-component $\alpha_{ij}^{(1,1)}$ of the response function in the two-shell medium of Figure 2.12B:

$$\alpha_{ij}^{(11)} = \frac{1}{6\pi\mu(\omega)a} Z(\lambda, \overline{\lambda}, \mu, \overline{\mu}, a, b)\delta_{ij}. \tag{2.77}$$

Here Z is a numerical factor that depends on the size of the perturbed pocket and both the bulk ($\mu(\omega), \lambda(\omega)$) and local ($\overline{\mu}(\omega), \overline{\lambda}(\omega)$) Lamé coefficients. As in the electrostatic case, fluctuations of a single bead will not yield unambiguous measurements of the bulk rheology unless $b = a$ and $(\mu, \lambda) = (\overline{\mu}, \overline{\lambda})$.

To compute the cross component, $\alpha_{ij}^{(21)}$, of the response tensor relating the displacement of bead 2 to the force applied on bead 1, it was found that the response could be decomposed into parallel ($\alpha_\parallel$) and perpendicular ($\alpha_\perp$) components along the separation vector $\mathbf{r}$ connecting the center of the two spheres:

$$\alpha_{ij}^{(21)} = \alpha_\parallel(r)\hat{r}\hat{r} + \alpha_\perp(r)(\delta_{ij} - \hat{r}_i\hat{r}_j), \tag{2.78}$$

where, to lowest order in a/r, the response along the line of centers is given by

$$\alpha_{\parallel} = \frac{1}{4\pi r \mu(\omega)}, \tag{2.79}$$

and the response perpendicular to the line of centers is

$$\alpha_{\perp} = \frac{1}{8\pi r \mu(\omega)} \left[\frac{\lambda(\omega) + 3\mu(\omega)}{\lambda(\omega) + 2\mu(\omega)} \right]. \tag{2.80}$$

Thus fluctuations parallel to the separation vector depend only on the bulk shear modulus, $\mu(\omega) = G(\omega)$, whereas those perpendicular to the line of centers depend on both the bulk λ and μ. The former result is consistent with Eq. 2.63, derived in the previous section for a homogeneous incompressible fluid. The latter result enables an experimental determination of frequency-dependent compressibility in viscoelastic materials via the ratio of $\alpha_{\perp}(\omega)/\alpha_{\parallel}(\omega)$. For incompressible materials $\lambda(\omega) \longrightarrow \infty$, the ratio of responses $\alpha_{\perp}/\alpha_{\parallel} = 1/2$, which is consistent with the results obtained for the ratio of particle diffusivities $D_{\perp}/D_{rr}$ for two-point microrheology in a homogeneous incompressible fluid from the previous section. The ability of two-point microrheology to isolate and measure distinct components of the shear, bulk, and elastic moduli is also a major advantage over one-point techniques. In principle, two-point methods can be extended to determine the elements of the stiffness tensor for lower symmetry phases such as crystalline or nematically-ordered liquid crystalline phases.

2.4 Active Microrheology

So far we have focused on the basic theory of passive microrheology measurements utilizing broadband thermal energy to excite fluctuations that can be related to the materials' underlying

linear rheology via the FDT. An alternative approach is to apply a gentle external force to the particle (via e.g. optical or magnetic tweezers) and to measure the amplitude and phase of its resulting displacement relative to that of the applied external force. The principle is the same as an oscillatory macroscopic rheometry measurement, however there are several notable differences in practice. First, there is a difference in length scales probed. Just as in the case of passive microrheology, the active microrheological measurement is more prone to the confounding effects of micron-scale inhomogeneities than macrorheology. In macrorheology the length scale of the deformation is much larger than any of the material's intrinsic length scales with the consequence that "bulk" rheology is always measured. However, the smaller length scale of active microrheology measurements is not entirely disadvantageous. For example, inertial effects, which arise at high frequencies when the viscous penetration depth is comparable to the sample thickness, can severely limit the upper frequency range of macrorheology measurements (typically $<$ 100 Hz). The micrometer length scales of microrheology measurements enable probing of much higher frequency measurements, owing to the fact that the frequency criterion for the dominance of inertial effects is $\omega \geq \sqrt{G/\rho\ell^2}$ where G is the shear modulus, ρ is the density of the surrounding fluid, and ℓ is the length scale of the shear deformation ($\ell = a$ for microrheology) [36, 60]. Finally, a more subtle effect is that the strain field around an oscillating probe is not viscometric (shear-only) but rather contains both shear and extensional components. At low frequencies in viscoelastic gels, for example, fluid can freely drain from the network, effectively decoupling the two and causing micro/macro disagreement [60]. No analog occurs in macroscopic rheometry as the strain field is viscometric (pure shear).

Active microrheology inherits many of the features of passive microrheology, but offers at

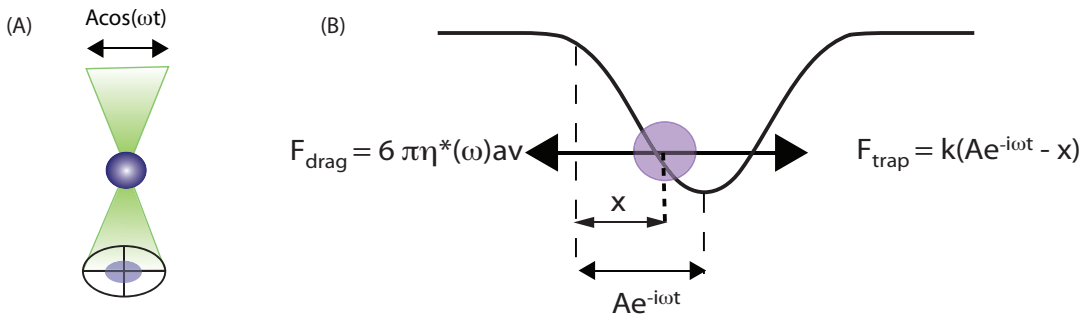

Figure 2.13: (A) Schematic of one-particle active microrheology measurement. An optically trapped particle is driven sinusoidally by the trapping laser and its position is detected. (B) Diagram of forces on a particle in an oscillating optical trap embedded in a viscoelastic medium.

least one potential and significant advantage: because the FDT constrains passive microrheology to the materials' linear response, it is conceivable that active microrheology can be used to extend microrheology to characterize the nonlinear rheology of complex fluids [97, 98]. This could be accomplished using an optical trap, for example, by increasing the amplitude of the trap displacement to be much larger than the probe size over a duration much shorter than the Brownian relaxation time of the material.

To illustrate active microrheology, we work out a simple example of a one-particle measurement using an oscillatory optical tweezer setup, depicted schematically in Figure 2.13A. The forces on the particle are shown in Figure 2.13B.

The probe particle's response is described by the equation of motion

$$m\ddot{x} = -6\pi a\eta^*(\omega)\dot{x} + k(Ae^{-i\omega t} - x), \tag{2.81}$$

where A is the displacement amplitude of the oscillating trap, k is the trap stiffness, a is the particle radius, and $\eta^*(\omega) = \eta'(\omega) - i\eta''(\omega)$ is the complex dynamic viscosity of the viscoelastic

medium. Note that in Eq. 2.81 we are treating the displacement x as a complex quantity as well in order to simplify the mathematical manipulations that follow. The optical trap is approximated as a harmonic well and the restoring force on the particle is given by the difference between the particle's position and the position of the minimum of the oscillating trap. The general solution for the position of the particle is

$$x(t) = D(\omega)e^{-i[\omega t+\delta(\omega)]}, \tag{2.82}$$

where $\delta(\omega)$ is the phase lag between the particle and the trap, and $D(\omega)$ is the frequency-dependent amplitude of the particle's position. Since the system is overdamped, we can safely ignore the $m\ddot{x}$ inertial term in Eq. 2.81 and substitute Eq 2.82 into Eq. 2.81 to solve for $D(\omega)$ and $\delta(\omega)$. This yields

$$D(\omega) = \frac{kAe^{i\delta(\omega)}}{(k - 6\pi a\omega\eta''(\omega)) - i(6\pi a\omega\eta'(\omega))} \tag{2.83}$$

$$\delta(\omega) = \tan^{-1}\left[\frac{6\pi a\omega\eta'(\omega)}{k - 6\pi a\omega\eta''(\omega)}\right]. \tag{2.84}$$

For the simple case of a particle in a Newtonian fluid where $\eta'(\omega) = \eta_0$ and $\eta''(\omega) = 0$, Eqns. 2.83 - 2.84 can be succinctly written

$$d(\omega) = \left|\frac{D(\omega)}{A}\right| = \frac{1}{\sqrt{1 + (\tau\omega)^2}} \tag{2.85}$$

$$\delta(\omega) = \tan^{-1}(\tau\omega), \tag{2.86}$$

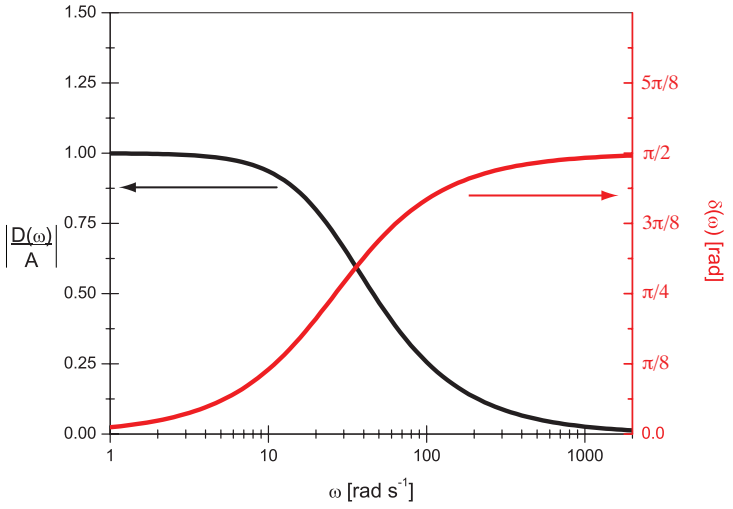

Figure 2.14: Normalized displacement and phase as a function of frequency for typical parameters $a = 2.0\,\mu m$, $\eta_0 = .001\,Pa\,s$, $k = 1 \times 10^{-6}$ N/m.

where $\tau = 6\pi\eta_0 a/k$. Eq. 2.85 is the amplitude of the particle displacement normalized by the amplitude of the oscillating trap. It is clear that for low frequencies ($\omega \ll 1/\tau$), the particle is able to displace with the trap ($D(\omega)/A \approx 1$), whereas for $\omega \gg 1/\tau$, the particle's displacement amplitude will roll off to zero. Concomitantly, the phase lag $\delta(\omega)$ increases from 0 for $\omega \ll 1/\tau$ to $\pi/2$ for $\omega \gg 1/\tau$ as shown in Figure 2.14.

It is also useful to solve for the one-particle response function $\alpha^*(\omega) = \frac{x(\omega)}{F_{trap}(\omega)}$ for the particle in the oscillating trap embedded in a viscoelastic medium

$$\alpha^*(\omega) = \frac{D(\omega)e^{-i\delta}}{kA} = \frac{1}{(k - 6\pi a\omega\eta''(\omega)) - i(6\pi a\omega\eta'(\omega))}. \tag{2.87}$$

Written in terms of real and imaginary components $\alpha^*(\omega) = \alpha'(\omega) + i\alpha''(\omega)$, Eq. 2.87 becomes

$$\alpha'(\omega) = \frac{k - 6\pi a\omega\eta''(\omega)}{(k - 6\pi a\omega\eta''(\omega))^2 + (6\pi a\omega\eta'(\omega))^2} \tag{2.88}$$

$$\alpha''(\omega) = \frac{6\pi a\omega\eta'(\omega)}{(k - 6\pi a\omega\eta''(\omega))^2 + (6\pi a\omega\eta'(\omega))^2}. \tag{2.89}$$

For the simple case of a particle in a Newtonian fluid where $\eta'(\omega) = \eta_0$ and $\eta''(\omega) = 0$, Eqns. 2.88 - 2.89 can be succinctly written

$$\alpha'(\omega) = \frac{1}{k(1 + \tau^2\omega^2)} \tag{2.90}$$

$$\alpha''(\omega) = \frac{\tau\omega}{k(1 + \tau^2\omega^2)}, \tag{2.91}$$

where $\tau = 6\pi\eta_0 a/k$. A typical response function is plotted in Figure 2.15. At low frequencies, the particle is able to follow the trap, resulting in a purely real and flat response function. At higher frequencies, the particle is unable to fully follow the trap and the phase lag increases, resulting in a decrease of the real component and an increase in the imaginary component of the response function. Finally, at the highest frequencies there is complete loss of phase coherence between the particle and the trap with the consequence that the particle's motion approaches that of constrained diffusion along a "line" traced by the trap's spatial trajectory [35]. The latter effect has been exploited to improve statistical power in microscopy-based colloidal interaction studies utilizing line-scanned optical traps [25, 111].

Alternatively, Eqns. 2.81 and 2.82 can be solved directly for the complex shear modulus $G^*(\omega)$ by making use of the relation between the complex shear modulus and complex viscosity

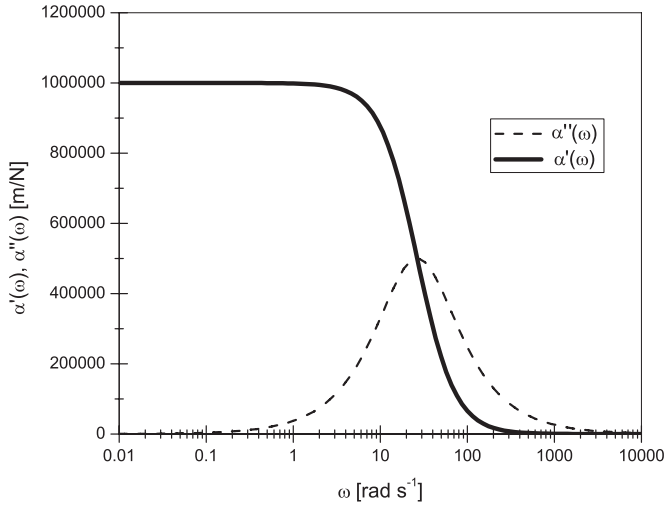

Figure 2.15: Real and Imaginary components of the response function for typical parameters $a = 2.0\,\mu m$, $\eta_0 = .001\,Pa\,s$, $k = 1 \times 10^{-6}$ N/m.

$G^*(\omega) = -i\omega\eta^*(\omega)$. Doing so yields the storage and loss moduli

$$G'(\omega) = \frac{k}{6\pi a}\left[\frac{A\cos\,\delta(\omega)}{D(\omega)} - 1\right]$$
$$G''(\omega) = \frac{k}{6\pi a}\left[\frac{A}{D(\omega)}\sin\,\delta(\omega)\right]. \tag{2.92}$$

Finally, we consider two-particle active microrheology measurements, as illustrated in Figure 2.16A. The only additional consideration in two-particle active microrheology is that the response function becomes tensorial, namely $x_n(\omega) = \alpha_{nm}(\omega)F_m(\omega)$, where x_n is the motion of the nth particle, F_m is the external force on the mth particle, and α_{nm} is the response tensor of the system with $n, m = 1, 2$. Much of the formalism required to understand these considerations has been covered in the previous sections on two-point microrheology and the electrostatic

analogy. Here we simply set up the framework for the determination of α^*_{nm} .

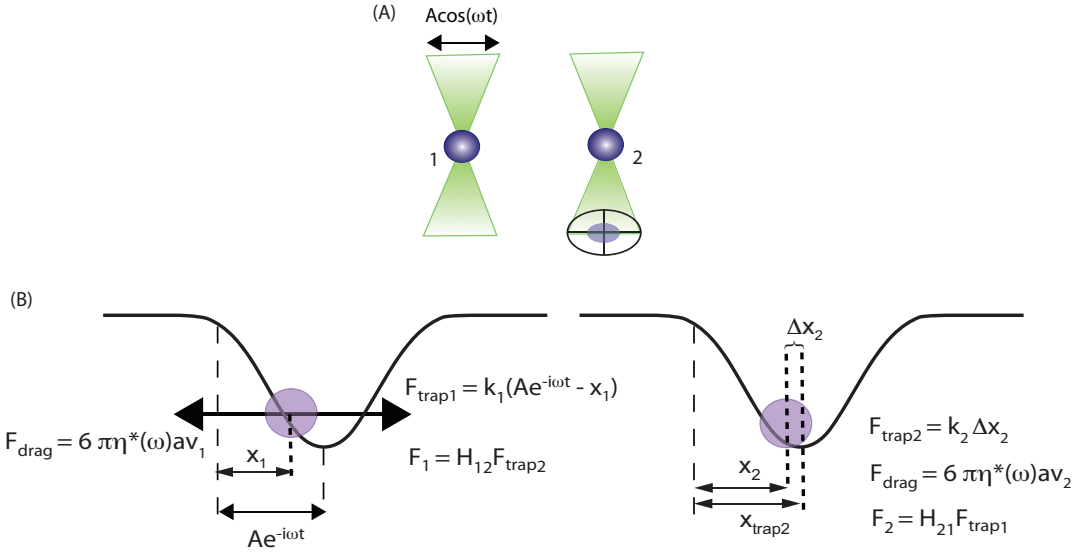

Figure 2.16: (A) Schematic of two-particle active microrheology measurement. Particle 1 is optically trapped and driven sinusoidally by a trapping laser and the position of particle 2 is detected. (B) Diagram of forces on particles where particle 1 is in an oscillating optical trap while particle 2 is held in a stationary trap.

For the situation sketched in Figure 2.16B in which two particles embedded in a homogeneous viscoelastic medium are optically trapped with particle 1 being oscillated while particle two is held fixed, the coupled equations of motion that must be solved are

$$\begin{aligned} \dot{x}_1(t) &= H_{11}[k_1(Ae^{-i\omega t} - x_1)] + H_{12}[k_2\Delta x_2] \\ \dot{x}_2(t) &= H_{21}[k_1(Ae^{-i\omega t} - x_1)] + H_{22}[k_2\Delta x_2] \end{aligned} , \tag{2.93}$$

where

$$H_{11} = H_{22} = \frac{1}{6\pi a\eta(\omega)} , \; H_{12} = H_{21} = \frac{1}{4\pi R\eta(\omega)} \tag{2.94}$$

are the lowest order components, in $1/R$, of the generalized Oseen tensor for motions along the

separation vector $\mathbf{R}$. Note that in writing down Eq. 2.93 we have neglected inertia and random thermal forces. The latter condition tacitly assumes that $F_{trap1,2} \gg F_R$. In order to determine the mutual component of the two-particle response function $\alpha^*_{21}(\omega)$, Eqns. 2.93 must be solved following a similar, albeit more mathematically complicated, protocol as Eqns. 2.81 - 2.89.

A two-particle implementation of active microrheology offers many advantages over one-point active measurements. Just as in the passive case, these include: robustness with respect to tracer boundary conditions, the ability to extract large scale bulk rheology, and the ability to measure compressibility. Moreover, two-point implementations of active microrheology can potentially enable measurement of the linear and nonlinear elasticity of low-symmetry systems such as crystalline or nematic liquid crystalline phases.

Chapter 3

Experimental Methods

3.1 Introduction

The work in this thesis relies heavily on digital video microscopy. This chapter will detail the methods used in the experiments described in Chapters 4-6. In particular, a detailed description of the experimental protocols will be given, along with a discussion about relevant experimental conditions and sources of experimental errors. The general procedures used for sample preparation are also described. Figure 3.1 schematically illustrates the workflow of a typical microrheology experiment. With the exception of the last section, the remainder of this chapter is organized according to the steps in the workflow sequence of Figure 3.1. The last section of this chapter covers active microrheology using oscillating optical tweezers, relevant to the work of Chapter 5.

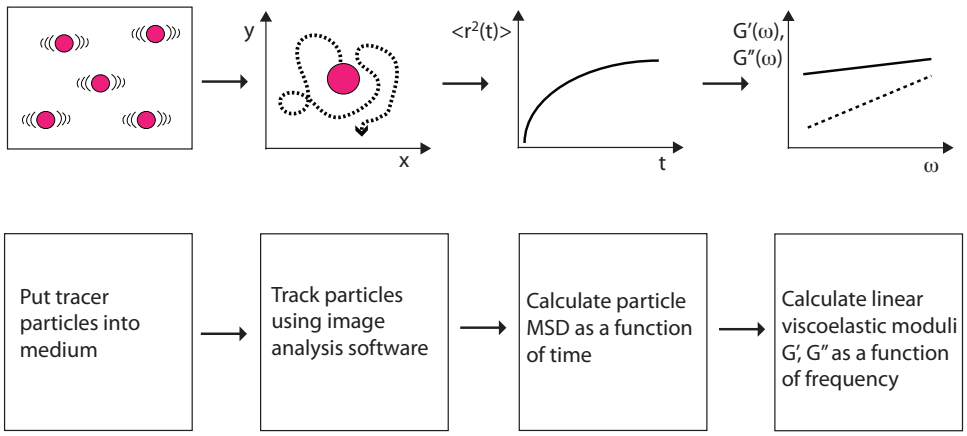

Figure 3.1: Workflow of a typical particle tracking microrheology experiment.

3.2 Selection of Tracer Particles

Choice of tracer particles can critically affect particle tracking microrheology results [109]. Among the most important considerations are size of the tracer particles, density of particle relative to the background fluid, and surface chemistry of the particle.

3.2.1 Tracer Particle Size

The biggest consideration in selecting the tracer particle size is the characteristic size of structures in the material of interest. For example, polymer networks are characterized by a mesh size ξ, which depends in part on the polymer concentration. If information about the bulk rheology of the network is desired, as determined from macrorheology, then the ideal particle will have a radius a that is larger than ξ (Figure 3.2A). If tracers are selected which are much smaller than the mesh size, then they will "slip" through the network, and they will not provide an accurate measure of the bulk rheological response of the network (Figure 3.2B). On the other hand, particles larger than the mesh size can only report the bulk rheological response of the network; their motions will not yield information about the pore size distribution of the material. As a rule, it is

useful to have an idea of the characteristic length scales of the material before choosing the size of the probes. In practice, particle radius a is limited to the range $200\,nm < a < 10\,\mu m$. The lower limit is due to the optical resolution of the microscope. The image processing algorithm requires at least 5 pixels for the particle centroid to be determined with high fidelity. The upper limit arises because to the particles become 'non-Brownian', with thermal fluctuations reduced below a measurable level.

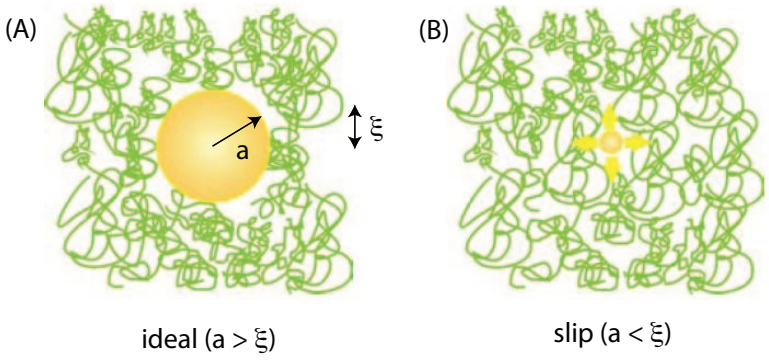

Figure 3.2: (A) The ideal particle for determination of bulk rheology using microrheology is larger than sample mesh size. (B) Particles that are much smaller will "slip" through the network, and their motions not reflect the bulk rheology.

3.2.2 Particle Density

Sedimentation can be a problem in particle-based microrheology measurements. In severe instances, sedimentation can drive the system out of equilibrium and/or limit the probe's residence time in the imaging volume. These effects limit the measurement duration and statistical resolution of the experiment. The velocity (v_{sed}) of a sedimenting probe illuminates the role of various parameters involved. A simple force balance, between gravitational density mismatch and the Stokes drag experienced by a non-interacting single particle in a purely viscous fluid, gives an expression for the sedimentation velocity

$$v_{sed} = \frac{2a^2 \Delta\rho g}{9\eta}, \tag{3.1}$$

where a is the radius, η is the viscosity, g is gravity, V is the particle volume, and $\Delta\rho$ is the difference in density between the particle and the fluid displaced by the particle. In order to minimize sedimentation, density matching of the particle and solvent is the surefire approach. In practice, however, it is often impossible or inconvenient to precisely density match. In this situation, working with smaller particles can decrease the effects of sedimentation. In general, the larger the probe particle, the more precise the density matching must be in order to achieve a given v_{sed}. Other than decreasing the density mismatch, Eq. 3.1 suggests that increasing the viscosity, η, may also counteract sedimentation due to density or size differences.

Another complication of sedimentation in microrheology experiments is that over time the probe particles will settle near the bounding surface of the density mismatched sample. The equilibrium distribution of the particle number density, $N(z)$, as a function of the height z above the bounding surface, is readily predicted by the Boltzmann distribution

$$\frac{N(z)}{N(0)} = e^{-\Delta\rho V g z / k_B T}, \tag{3.2}$$

where $N(0)$ is the probe density at the surface. Ideally, probe concentration should be uniform and low ($\phi \approx 10^{-4}$). Higher densities can render the tracking algorithms inefficient, e.g., by disrupting the unique identification of the particles due to spatial overlap. Moreover, proximity to the boundary can complicate interpretation of microrheology results, as will be discussed in a later section.

3.2.3 Surface Chemistry

Nearly all beads commonly employed in colloidal studies require surface chemistry modifications in order to stabilize them against flocculation. This is most commonly accomplished by coating the particle surface with charged groups or by adding a layer of polymer for steric stabilization. Charge functionalization schemes such as adding carboxylate ($-COOH$), amine ($-NH_4$), or sulfonate ($-SO_4$) groups on polystrene (PS) particles, or hydroxyl ($-OH$) groups on silica (Si) particles, is best for aqueous systems of low ionic strength ($< 10\,mM$). These groups ionize in water, releasing their H^+ counterion, with the result that the particle becomes charged and repulsively stabilized. For a $10\,mM$ NaCl solution, the screening length is ≈ 3 nm. The long range nature of the electrostatic repulsion keeps the particles far apart, keeping the particles from feeling the relatively shorter range minima of nonspecific attractive interactions such as van der Waals and depletion. At higher ionic strengths, or if divalent counterions are present, the charges on the spheres will be screened and flocculation will generically occur. By contrast, steric stabilization is better suited for stabilizing short range attractive forces such as the van der Waals forces that are ubiquitous whenever the particle and solvent are index mismatched. In practice, we have found carboxlyate PS spheres to be the most useful non-stick surface chemistry for most uncharged polymers in aqueous systems such as polyethylene oxide (PEO) under typical conditions. For samples of more highly charged species such as biopolymers or bacteria, Bovine Serum Albumin (BSA) is a useful blocking agent. Typically, incubating the spheres in a 0.1 wt % BSA is sufficient to coat them.

3.2.4 Microscope Slide Chamber

For most of the experiments in this thesis, the samples (i.e., material + particles) were mixed and loaded into microscope chambers made of a microscope slide and coverslip attached with either heated parafilm, 5-minute epoxy, or UV-curable optical glue. A typical chamber construction used for aqueous samples is shown in Figure 3.3. The sample chamber is constructed by sandwiching two parafilm strips cut into an L-shape between a microscope slide and a coverslip. The narrow opening on both opposite ends is necessary for filling the chamber with capillary forces. Heating the construction on a hotplate at a moderate setting for $\sim$ 10 seconds is sufficient to melt the parafilm, and gently pressing on the coverslip with a pair of tweezers is sufficient to adhere the coverslip to the slide. In practice, this procedure reproducibly yields chambers with a thickness of 50 - 80 μm. Thicker samples may be produced by stacking more parafilm layers, with each layer contributing a multiple of 50-80 μm, up to at least 4 layers. After loading the sample chamber, the two open ends can be hermetically sealed with epoxy or UV-curing optical glue. Aqueous samples can last for approximately a week in these chambers with no visible sign of sample evaporation (e.g., air bubbles).

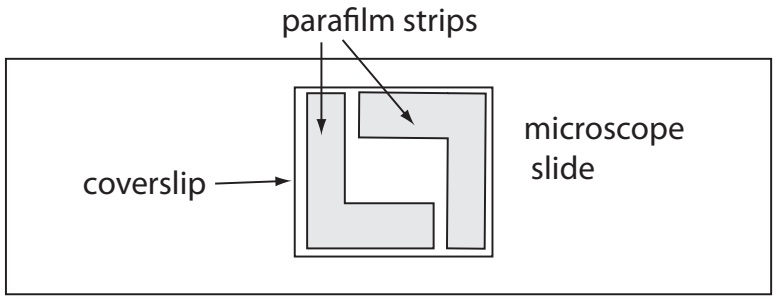

Figure 3.3: Sample chamber construction used in typical experiments.

If longer lifetime chambers are desired or if non-aqueous (e.g. organic solvents) samples are

to be used, then the chamber seals should be constructed of optical glue (Norland) or epoxy (Devcon) instead of parafilm. The principle of the construction is the same, including the necessity of leaving a gap for facile loading. Control of the chamber thickness can be achieved using commerically available spacers (McMaster-Carr). In practice, these chambers can last several weeks without visible evaporation. Ultimately, the lifetime depends on the volatility of the solvent.

3.3 Digital Video Microscopy

The ability to quantitatively track the motion of micron-sized probe particles is critical to our work. To do this, we need an optical microscopy system with high resolution imaging capabilities, and also high-quality image processing algorithms to analyze the recorded image data. In this section, we describe the methods of digital video microscopy that were used to obtain and process the images in this thesis.

Methods of digital video microscopy are by now standard, and detailed information is readily available in the form of textbooks, methods articles, and websites. Much of the descriptions in this section are sourced from these references. For details on the microscope's inner workings, the textbook on video microscopy by Inoué and Spring [51] is an excellent source of information. The best resources for the image processing methods employed in this thesis are the methods articles by Crocker and Grier [23] and, more recently, by Crocker and Hoffman [24]. An excellent systematic study of static and dynamic errors in particle tracking is contained in articles by Savin and Doyle [91, 92]. Eric Week's group maintains a website [115] that is a valuable resource for the particle tracking community. In addition to having a detailed tutorial on particle tracking, it is also an aggregator of source code for particle tracking in IDL, MatLab, and C++. All of the

IDL routines referenced in this chapter are freely available for download there.

The purpose of this section is not to replicate the material in the aforementioned articles, but rather to present a general picture and provide references for the specific details. We will focus instead on highlighting topics that are not addressed in the existing literature and experimental details are particular to the suite of experiments in this thesis.

3.3.1 Microscope

In its simplest form, an optical microscope consists of two positive lenses: an objective lens of short focal length that images the object and a magnifier that functions as an eyepiece. Most modern microscopes use infinity-corrected optics, i.e., the objective forms the intermediate image at infinity (rays are parallel) and another lens to focus the intermediate image before the eyepiece. The advantage of this design is that additional elements (e.g. polarizers, prisms, dichroic flats, spatial filters, etc.) can be inserted into the optical train as needed since the light will remain parallel so long as the elements do not focus the rays.

A bright field microscope image is the consequence of the interference of direct light from the light source and transmitted light diffracted by the specimen. This concept was introduced by Ernst Abbe in 1870 and is illustrated in Figure 3.4. Light from a point source in the form of spherical wavefronts is collimated by a condenser and converted into plane waves which are sent into the specimen. Some of this light is diffracted by regions of varying index of refraction in the specimen while some pass through unaltered. Both the diffracted and undiffracted light are collected by the objective and focused in the Back Focal Plane (BFP) of the objective. The intermediate image is then formed by the interference of the light. Interference is the mechanism by which contrast is generated in the image of the specimen. Thus image contrast depends

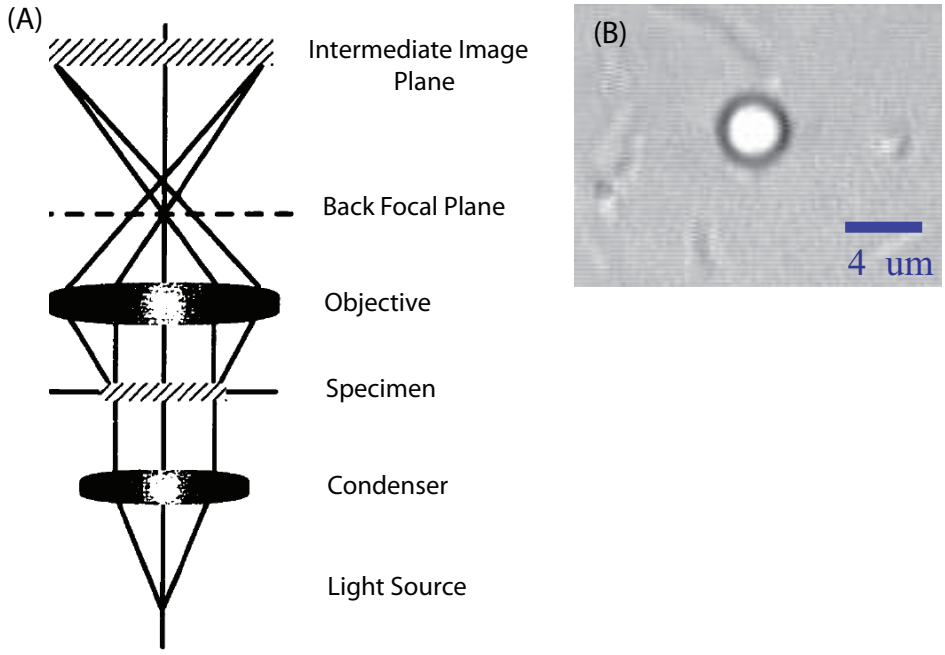

Figure 3.4: (A) Schematic of image formation in a bright field microscope [62]. (B) Bright field image of a 4 μm diameter Polystrene (n = 1.6) particle taken with a 20X water immersion NA = 0.7 objective.

on both the variations in index of refraction of the specimen and also on the coherence of the light source. A concrete example of interference-based image formation process can be found in a bright field image of a particle. As a consequence of interference, the intensity profile of the particle is not a circularly symmetric Gaussian, as is expected for an incoherently self-luminous particle in an aberration-free fluorescence imaging setup, but rather the particle's image is an Airy disk consisting of central bright maximum, surrounded by alternating bright and dark circularly symmetric rings as shown in Figure 3.4B. The rings are the result of interference between the light diffracted from different regions of the particle and the undiffracted light.

The schematic of the simple microscope setup also motivates the concept of reciprocal and conjugate planes in microscopy. Two planes are called reciprocal planes when points in one plane are mapped onto the other via a lens and vice versa. In the setup of Figure 3.4A, the BFP is the reciprocal plane of the specimen image plane. Another way of looking at the relationship between reciprocal planes is as a spatial Fourier transform. For instance, the BFP is the spatial Fourier transform of the specimen image plane since the objective focuses the plane waves from the specimen plane to a point via conversion into spherical waves. By contrast, two planes which share common focus are called conjugate planes. In Figure 3.4A, the specimen and intermediate image planes are conjugate planes, as are the BFP and the light source plane. Modern microscopes typically contain two sets of conjugate planes, image and aperture planes. The images planes include field diaphragm, specimen plane, intermediate image plane, and retina. The aperture plane consists of the light source, condenser diaphragm, objective back focal plane, and pupil. These planes are illustrated in Figure 3.5. Most high-end microscopes, including ours, contain a removable lens known as a Bertrand lens that can be used toggle between the two conjugate planes, permitting the user to observe the back focal plane of the objective. This is useful for aligning the phase ring for phase-contrast microscopy and for doing quick-and-dirty Bragg scattering measurements of e.g. colloidal crystals in a microscope.

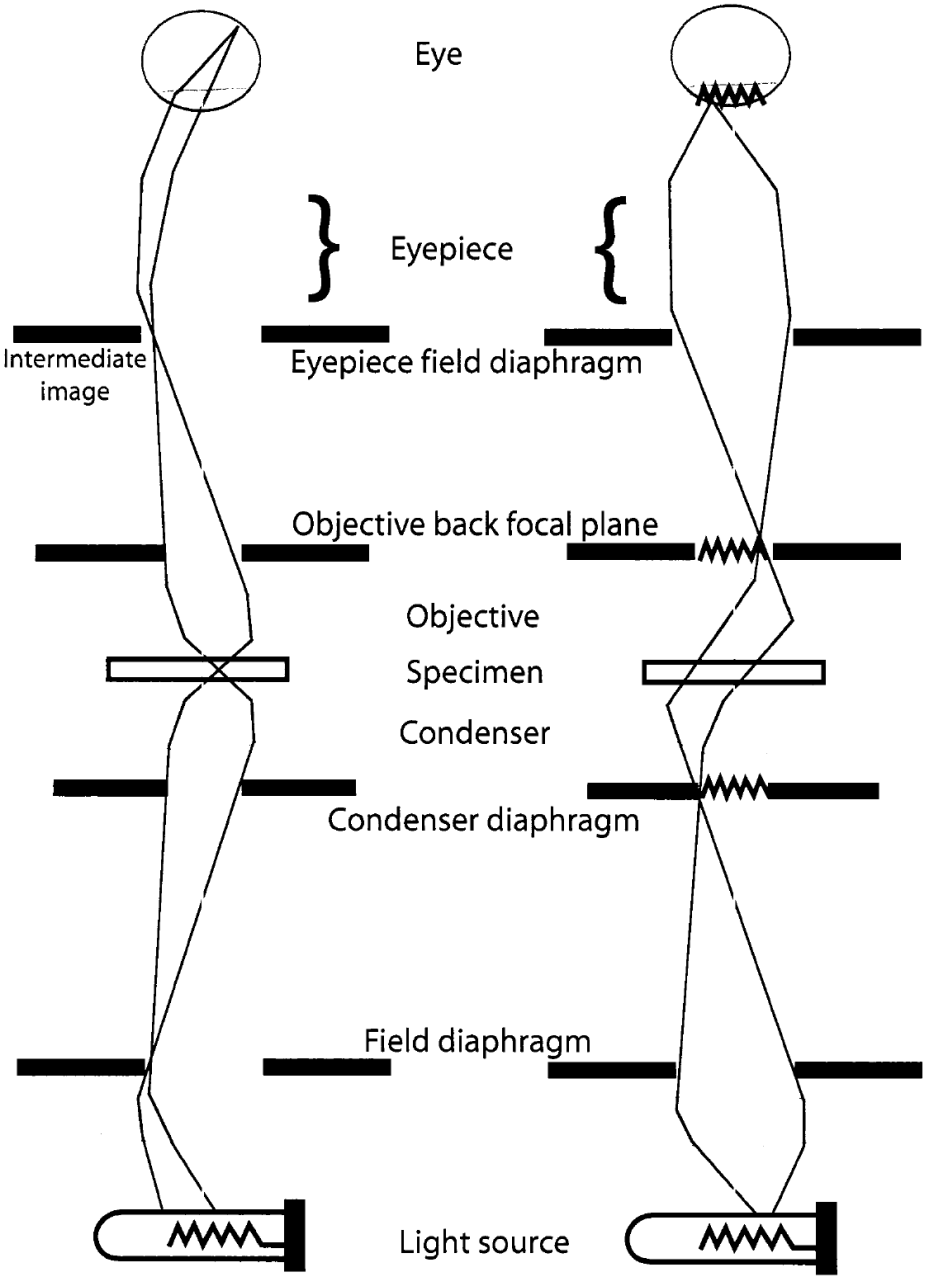

Figure 3.5: Image beam path (left) and illumination beam path (right) in Kohler illumination design [4].

In order to achieve optimal image quality it is important to set up Kohler illumination in the microscope's optical train. Kohler illumination is an alignment protocol that ensures every point in the specimen plane is evenly illuminated with parallel light rays emanating from the lamp filament, as shown in Figure 3.5. Essentially, this makes the illumination plane reciprocal to the image plane, eliminating contamination in the form of granularities from dirty surfaces which may be present in the aperture planes. For instance, this scheme has the effect of ensuring that the lamp filament is not imaged along with the specimen, a major problem in the early days of microscopy. A good step-by-step procedure for achieving Kohler illumination can be found in [82].

The most important optical parameter of a lensing element (e.g. objective or condenser) is the numerical aperture (NA) defined as

$$NA = n \sin \theta, \tag{3.3}$$

where n is the index of refraction of the medium between the objective or condenser and the coverslip and θ is half-cone angle of light captured by the lensing element (Figure 3.6). Common values of n are n = 1.00 (Air), n = 1.33 (water), and n = 1.5 (immersion oil). The system NA sets both the working distance and the lateral resolution of the of the lensing element, i.e., the minimum distance between two diffraction-limited objects that can be resolved in the image plane. For transmitted light (bright field) illumination, this distance is

$$r = 1.22\lambda_0/(NA_{obj} + NA_{cond}). \tag{3.4}$$

For self-luminous objects, as in reflection fluorescence (epi-fluorescence) illumination where the objective focuses both excitation and emission, the resolution r is determined solely by the NA of the objective lens and is

$$r = 1.22\lambda_0/2NA_{obj}. \tag{3.5}$$

Eqns. 3.4 and 3.5 are statements of the Rayleigh criterion which dictates that two non-interfering Airy disks are barely resolvable when the first minimum of one and zeroth-order peak of the other are separated by a distance r. Higher resolution corresponds to a smaller value of r and is produced by increasing the NA. Conversely, lower resolution corresponds to a larger value of r and occurs when the NA is reduced. High-end microscopes contain irises in the condenser back focal plane which can be used to adjust the working NA by the modulating the angle θ, as shown in Figure 3.6. Reducing the condenser iris has the dual effect of reducing the NA_{cond} and increasing the coherence of the illumination light since the light that is collected then originates from a smaller region of the illuminating filament. This reduction of condenser iris diameter has the effect of increasing image contrast due to increased diffraction in the image from the enhanced coherence, but this gain comes at a cost of lower resolution.

Another important optical microscope imaging parameter controlled by the NA is the depth of field, d. The depth of field sets the longitudinal resolution of the optical system. The depth of field is the axial distance from the nearest object plane in focus to the farthest plane that also appears in focus. It is given by

$$d = 1.22\frac{\lambda_0 n}{NA^2} + \frac{n}{M \cdot NA}e, \tag{3.6}$$

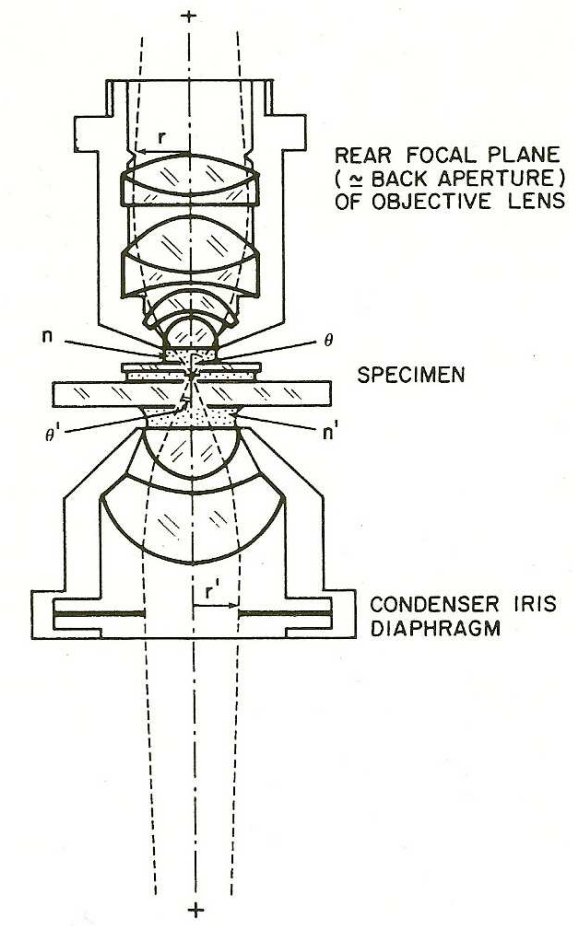

Figure 3.6: Numerical apertures and paths of light rays in the condenser and objective lens. The working numerical aperture of the condenser is $NA_{cond} = n' \sin\theta'$ and the working numerical aperture of the objective is $NA_{obj} = n \sin\theta$. NA_{cond} is proportional to r', the radius of the condenser iris opening [51].

where n and λ_0 are defined as before, and the variable e is the smallest distance that can be resolved by a detector placed in the image plane of the microscope objective whose lateral magnification is M.

3.3.2 Bright field vs Fluorescence Microscopy

Most of the images we used in our studies were acquired with bright field or epi-fluorescence microscopy. There are advantages and disadvantages to both modalities. By far the biggest

drawback of fluorescence is the requirement of a labeling dye to be added to the particle or background. A related drawback of fluorescence is that many of the commonly available dyes exhibit photobleaching over time, requiring the user to monitor the levels of intensity and make adjustments to the microscope or image processing parameters accordingly. In practice, however, commercially available particles such as rhodamine-labeled FluoSpheres (Invitrogen) have a fairly robust fluorescence and do not bleach appreciably over the course of a typical microrheological measurement of duration ≈ 20 minutes. An advantageous feature of fluorescent particles is that they are ideally suited for particle tracking, appearing as nearly circularly symmetric Gaussian spots against a dark background. Moreover, the point spread function in fluorescence imaging is independent of particle size, permitting a wider range of particle sizes to be used. By contrast, the Airy disk profile of coherent bright field particles is a sensitive function of the height of the particle relative to the image focal plane, as shown in Figure 3.7, requiring a careful setting of tracking parameters. In particular, bright field particles below the image plane acquire a "donut" shaped intensity profile which is problematic for centroiding algorithms. Note, the shallower depth of field required in bright field tracking is not entirely disadvantageous. In two-point microrheology measurements, for instance, bright field permits a more precise determination of interparticle separations.

3.3.3 Particle Tracking

The first step in particle tracking is to obtain optimal images of the particles themselves. In practice, this entails setting up the microscope in Kohler illumination and adjusting camera settings (gain, offset, shutter time) to ensure maximal signal-to-noise ratios. For a monochrome 8-bit CCD camera, such as our Hitachi KP-M1 NTSC camera, this means adjusting the gain

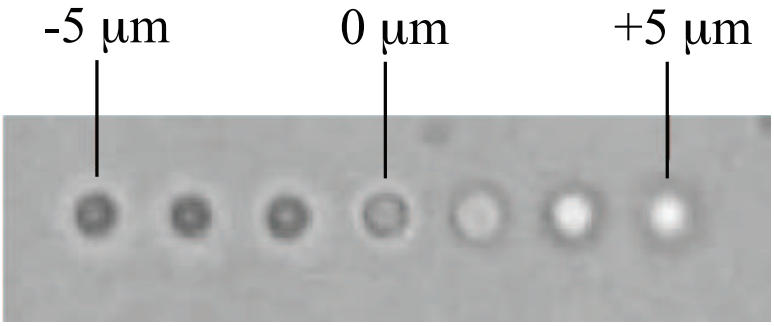

Figure 3.7: Bright field image of seven 1 μm diameter silica spheres held using holographic optical tweezers from 5 μm below to 5 μm above the image focal plane [28].

and offset to get the full linear dynamic range. When this condition is satisfied, a histogram of pixel intensities should span $\approx$ 40 - 200 in intensity values. Ideally, every particle should have an unsaturated (Gaussian) intensity profile, a strong prerequisite for sub-pixel positional accuracy. Oversaturation leads to a clipped, "flat-top" intensity profile for which sub-pixel accuracy on the centroid is compromised. Under optimal illumination conditions, the IDL routines, when properly used, are capable of locating the center of an isolated 1.0 μm particle to within $\approx 10nm$.

Previously, the images in our lab were recorded to an S-VHS videotape deck (Sanyo GVR-S950) and subsequently digitized via a framegrabber card (Scion LG-3) onto hard disk. More recently, circa 2005, we have upgraded to a custom image capture system (Advanced Digital Vision, Natick, MA) that digitizes directly onto a RAID5 hard disk array. This eliminates the electronic noise from the video tape-to-drive read-write transfer step.

After the images are acquired, image processing is done offline using routines written in IDL (Interactive Data Language, ITTVIS Inc.). The process of tracking particles can be broken down into three main stages, as shown in the workflow diagram of Figure 3.8. The first stage, collectively termed pretracking, involves starting from a stack of sequential images and filtering

the images to eliminate noise and unwanted features so that it is readily possible to accurately locate the particle centers in these images. The second stage, tracking, involves linking the features found in the pretracked images to identify each particle uniquely in each successive frame; we thus obtain a trajectory for each particle. Finally, the last stage, broadly termed post-tracking, involves the manipulating the information contained in the trajectories into a form that can be readily compared with model predictions, e.g., MSDs or linear viscoelastic moduli.

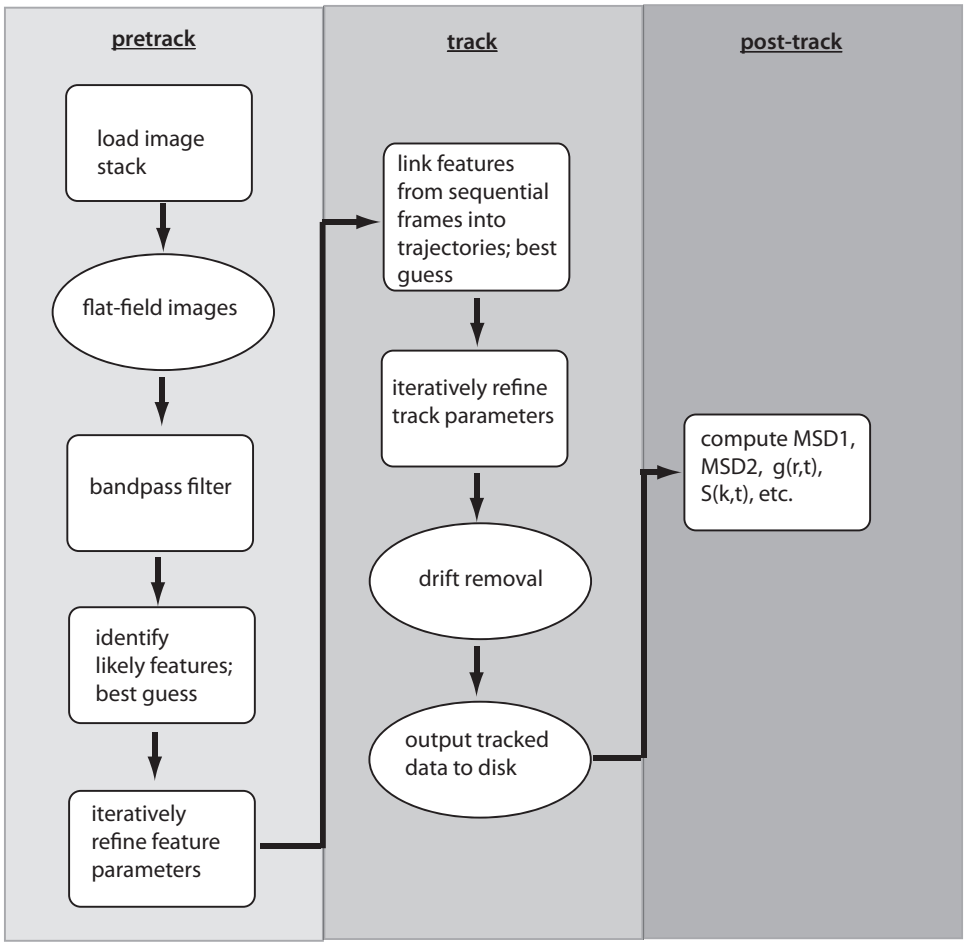

Figure 3.8: Workflow of image processing and particle tracking steps. Elliptical enclosures denote optional steps.

For details on the algorithms used in the image processing steps, the reader is referred to the Weeks group online tutorial [115]. In this tutorial, the reader will find a step-by-step discussion on particle tracking using IDL along with the routines. A thorough discussion of the considerations involved in setting optimal parameters for the routines is contained in [24].

3.3.4 Static and Dynamic Errors in Particle tracking

There are two main categories of error in the determination of particle position: static and dynamic errors. Static error originates from random errors in the determination of particle postition and are "static" in the sense that they occur even in an image of an immobilized particle. These static random errors are the result of photon counting statistics and are intrinsic to the imaging process. Basically, all image processing algorithms determine the position of the particle as the mean, or center of mass, of a distribution of photons hitting the CCD. Accordingly, the standard error on the mean (ε) is subject to statistical fluctuations in photon count number (N) given by

$$\varepsilon = \frac{\sigma}{\sqrt{N}}, \tag{3.7}$$

where σ is the standard deviation of a Gaussian distribution of N photons. Under typical experimental conditions, σ is the apparent radius of the particle a and N is sufficiently large to saturate the dynamic range of the CCD. When the latter condition is met and near-optimal image processing parameters are set, then ε is the spatial resolution of the setup, roughly $1/10$th of a pixel.

The static error results in a random offset, χ, in the measured position, $\overline{x}$, of the particle:

$$\overline{x}(t) = x(t) + \chi(t), \tag{3.8}$$

where $x(t)$ is the true position of the particle center and $\chi(t)$ is a stationary random offset with mean $\langle \chi(t) \rangle = 0$ and variance $\langle \chi^2(t) \rangle = \varepsilon^2$. The static error results in an additive offset to the MSD [66, 92] given by

$$\langle \Delta \overline{x}^2(\tau) \rangle = \langle \Delta x^2(\tau) \rangle + 2\varepsilon^2. \tag{3.9}$$

The error is most apparent at short lag times in highly viscous media for which the diffusive particle displacement in one timestep is comparable to the measurement spatial resolution $\varepsilon \approx$ 1/10th of a pixel. On a log-log plot of the MSD, it manifests as an apparent subdiffusion at early times even in a purely viscous Newtonian fluid, such as a mixture of glycerol and water. The apparent subdiffusion spoofs a short time elastic response characteristic of the MSD expected for entangled polymeric solutions for lag times shorter than the relaxation time, as described by the Maxwell model. In practice, the static error can be subtracted off the measured MSD ($\langle \Delta \overline{x}^2(\tau) \rangle$) to yield the true MSD ($\langle \Delta x^2(\tau) \rangle$). Figure 3.9 shows the effect of the static error in the MSD of a particle in an 80 % glycerol in water mixture before and after the $2\varepsilon^2$ has been subtracted off, recovering the expected linear dependence on τ. Note the false plateau from the noise floor at short lag times in the uncorrected MSD. In general using a higher illumination intensity will reduce the static error, but this approach is ultimately limited by detector saturation and the tradeoff for minimization of dynamic error.

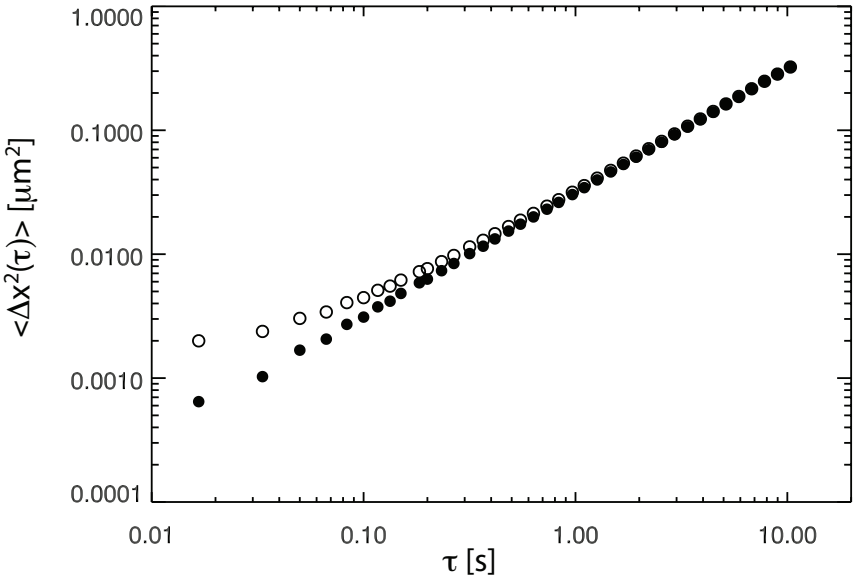

Figure 3.9: Mean square displacement vs. lag time for a $2a$ = 1 μm particle diffusing in 80 wt % glycerol in water mixture with η = .070 Pa s. Open circles are the raw MSD. Solid circles are the MSD with static error $2\varepsilon^2$ subtracted off.

Dynamic error stems from the "smearing" of the particle image that results if a particle moves significantly during the time interval, σ, during which the CCD camera's electronic shutter is open and collecting photons. The position acquired at time t thus contains the history of the successive positions occupied by the particle during the time interval $[t-\sigma, t]$. The particle's measured position, $\overline{x}(t,\sigma)$, can be mathematically described as a convolution of the particle's true position, $x(t)$, with a blur kernel, $H(t)$, accounting for the finite shutter time, σ, via

$$\overline{x}(t,\sigma) = (H * x)(t) \equiv \int H(\xi)x(t-\xi)d\xi, \tag{3.10}$$

where $H(t)$ is defined by

$$H(t) = \begin{cases} \frac{1}{\sigma} & 0 < t \leq \sigma \\ 0 & \text{elsewhere} \end{cases} \tag{3.11}$$

with the result that

$$\overline{x}(t,\sigma) = \frac{1}{\sigma}\int_0^\sigma x(t-\xi)d\xi. \tag{3.12}$$

The smearing affects centroiding that the image processing algorithm uses to determine the position of the particle's center. The net effect of the dynamic error is to systematically cause the apparent displacement of the tracked particle to be smaller than the actual displacement. This effect, in turn, results in a measured mean square displacement $\langle \Delta\overline{x}^2(\tau)\rangle$ with downward curvature at short lag time τ. Savin and Doyle [91,92] have carried out a detailed analysis of the dynamic error on the MSD and obtained a general formula, derived from Eq. 3.12, which yields an expression for the dynamic error-biased MSD:

$$\langle \Delta \overline{x}^2(\tau,\sigma)\rangle = \frac{1}{\sigma^2}\int_0^\sigma [\langle \Delta x^2(\tau+\xi)\rangle + \langle \Delta x^2(\tau-\xi)\rangle - 2\langle \Delta x^2(\xi)\rangle](\sigma-\xi)d\xi. \qquad (3.13)$$

where $\langle \overline{x}^2(\tau,\sigma)\rangle$ is the measured dynamic error-biased MSD, $\langle \Delta x^2(\tau)\rangle$ is the true unbiased MSD, and σ is the shutter time. In theory, any functional form describing the MSD can be plugged into Eq. 3.13 and a functional form for the dynamic error-biased MSD can be obtained. This is the basic procedure that we use for our MSD data of Chapter 6 (detailed in the Appendix). Here we demonstrate its use on experimental data for a relatively simple system - particle diffusion in a Newtonian fluid. In the absence of static and dynamic errors, the measured ensemble-averaged MSD will be described by the functional form: $\langle \Delta x^2(\tau)\rangle = 2D\tau$ where $D = k_bT/(6\pi\eta a)$ is the self-diffusion coefficient with temperature T, viscosity η, and particle radius a. However, in the presence of static and dynamic errors, the measured MSD becomes:

$$\langle \Delta \overline{x}^2(\tau,\sigma)\rangle = 2D(\tau-\sigma/3) + 2\varepsilon^2. \qquad (3.14)$$

where the first term on the right hand side was derived from Eq. 3.11. In the data of Figure 3.10, we have subtracted off the static error, and only the consider the remaining dynamic error.

The dynamic error results in a downward curvature qualitatively resembling superdiffusion in a log-log plot of the MSD, typically most apparent at short lag times, as shown in Figure 3.10 where the open circles are data for 1 μm diameter particles in water with $\sigma = 1/30\,s$. We have plotted the lag time rescaled MSD $\langle \Delta x^2(\tau)\rangle/2\tau$ as a function of τ, in order to highlight

this downward curvature. In the absence of dynamic error, the data should be a flat line with y-intercept D. The solid line is a fit to Eq. 3.14 from which we extract $D = 0.512\,\mu m^2/s$ as expected for a 1 μm diameter particle diffusing at T = 298 K with $\eta = 1\,mPa\,s$. Once D is extracted, the dynamic error can be completely removed by adding $2D\sigma/3$ to the MSD data, and the expected flat line is recovered, as the solid circles in Figure 3.10 attest.

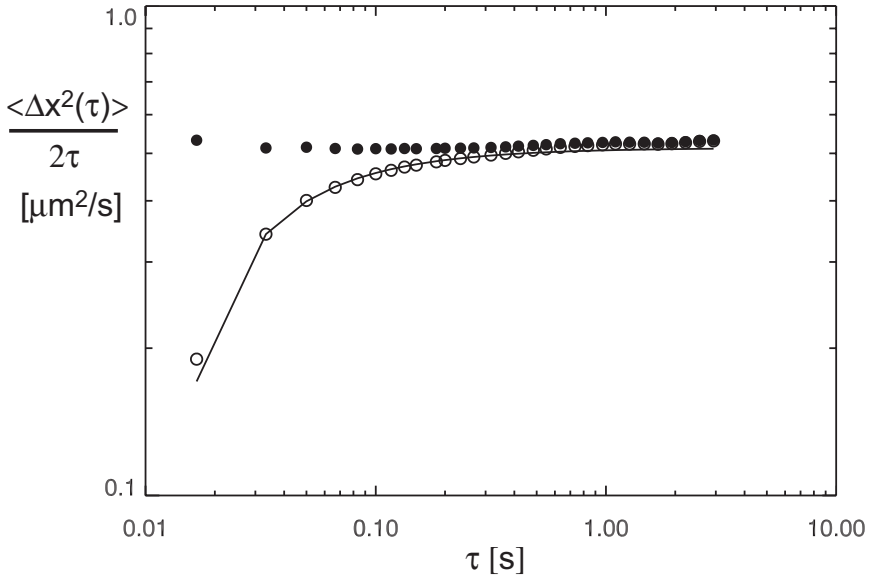

Figure 3.10: Scaled mean square displacement as a function of lag time for a 1 μm particle diffusing in water. Open circles are the msd obtained with $\sigma = 1/30\,s$ on the CCD camera. Solid line is a fit to Eq. 3.14 with $\sigma = 1/30\,s$ yielding $D = 0.512\mu m^2/s$ as expected for a 1 μm diameter particle diffusing at T = 298 K with $\eta = 1\,mPa\,s$. Solid circles are the msd corrected for dynamic error as outlined in the text.

This procedure can be generalized to arbitrary functional forms of the MSD: $f(\tau, \mathbf{x})$ where **x** includes all model parameters. First, $f(\tau, \mathbf{x})$ is convolved with instrumental resolution to yield $f(\tau, \mathbf{x}, \sigma)$. Then $f(\tau, \mathbf{x}, \sigma)$ is fitted to the dynamic error-biased experimental data to extract **x**, the parameters for the unbiased MSD. Note that the derivation of $f(\tau, \mathbf{x}, \sigma)$ does not incur the cost of introducing a new parameter; the value of σ is known. The dynamic error for each lag time $\delta(\tau)$ can then be estimated as $\delta(\tau) = |f(\tau, \mathbf{x}) - f(\tau, \mathbf{x}, \sigma)|$. Once $\delta(\tau)$ is obtained, the

dynamic error corrected MSD: $\langle \Delta x^2(\tau) \rangle = \langle \Delta \overline{x}^2(\tau, \sigma) \rangle + \delta(\tau)$ can be obtained. An example of this procedure can be found in the Appendix, wherein we corrected the MSD data of Chapter 6 for dynamic errors.

3.3.5 Influence of boundaries

The no-slip boundary condition of the fluid's velocity field on the boundaries of the particle and the walls of the sample chamber can affect microrheology measurements. In the simplest case of an isolated sphere of radius, a, in a fluid of viscosity, η_0, at a distance, h, from a planar wall, Faxen's Law [43] gives the drag coefficient ζ as

$$\zeta = \frac{6\pi\eta_0 a}{1 - \frac{9}{16}\left(\frac{a}{h}\right) + \frac{1}{8}\left(\frac{a}{h}\right)^3 - \frac{45}{256}\left(\frac{a}{h}\right)^4 - \frac{1}{16}\left(\frac{a}{h}\right)^5}. \tag{3.15}$$

Here the bare drag coefficient, $6\pi\eta_0 a$, is modified near the wall by higher order terms in powers of a/h. Eq. 3.15 predicts that the effective viscosity η is increased by the presence of the wall. To leading order $\eta = \eta_0(1 + \frac{9}{16}\frac{a}{h})$. It is tempting to simply "double" Eq. 3.15 to calculate the drag for a sphere between two walls, as in a typical sample chamber (Figure 3.11C). However, doing would underestimate the drag coefficient [43].

It is relatively straightforward to account for wall effects in one-point passive microrheology measurements since the particle size and distance of image plane from the walls are both known. For example, this knowledge permits a determination of η from the GSER using the wall-effect modified viscosity of Eq. 3.15 at no additional cost. Additionally, a high NA water immersion objective can be used to minimize refractive aberration in aqueous samples, permitting measurements deep into the chamber. Two-point passive microrheology experiments, by

contrast, present a greater experimental challenge than one-point measurements due to the fact that interpretation of results requires that the longitudinal component of the two-point correlation $D_{rr} \sim 1/R$, where R is the particle separation.

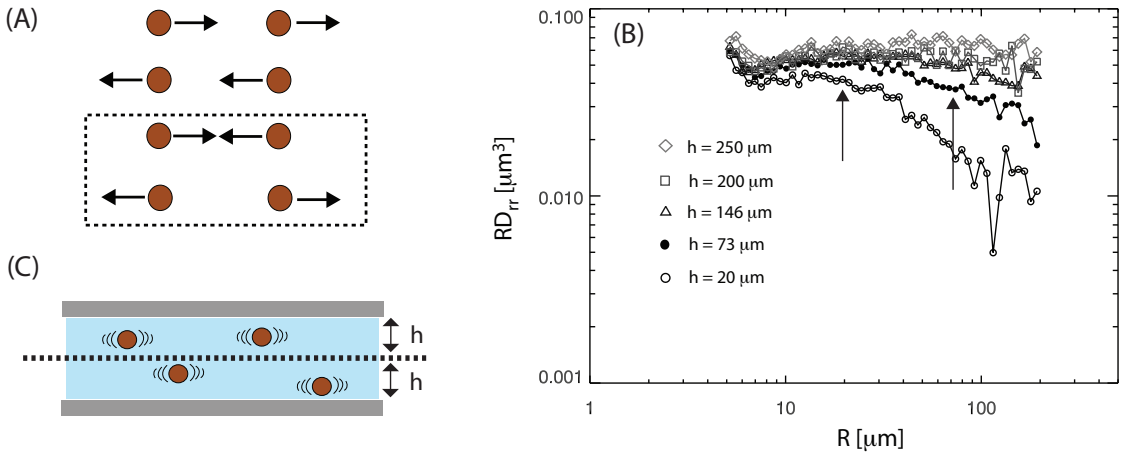

Figure 3.11: (A) Four basic pair motions described by D_{rr}. The relative displacements (boxed) are suppressed to a greater degree from the no-slip fluid boundary interaction than the net translations, for a given amplitude of motion. (B) Plot of the separation scaled two-point correlation $R*D_{rr}(R, \tau = .083s.)$ vs. particle separation R for varying chamber thicknesses h. The arrows indicate $R = 20\,\mu m$ and $R = 73\,\mu m$ corresponding to the distance h of the two thinnest chamber data sets.The particle radius in all the data sets is $a = 1\,\mu m$. (C) Schematic of D_{rr} depth dependence measurement. The image plane is at the center of the sample chamber a distance h from both walls.

Physically, D_{rr} describes four basic motions illustrated in Figure 3.11A. Two are net translations in which the two particles move in the same direction, along their line of separation. Two are relative displacements in which the particles move toward or away from each other, along their line of separation. In an unbounded medium, these motions are excited by thermal fluctuations with equal probability, in harmony with the observation that $D_{rr} \sim 1/R$. In a bounded medium, however, the latter motions require "squeezing out" or "pulling in" the intervening incompressible fluid. The relative motions are therefore strongly suppressed by the no-slip boundary conditions from the walls, whereas the net translational motions are affected to

a lower degree. Thus, the presence of the boundaries breaks the "degeneracy" of these motions, with the consequence that D_{rr} will decay faster than $1/R$, i.e., $D_{rr} \sim 1/R^{\alpha}$ where $\alpha > 1.0$. Figure 3.11B shows $RD_{rr}(R, \tau = .083s)$ plotted as a function of separation R for two-point data taken from the middle of the chamber for varying thicknesses h, as illustrated in Figure 3.11C. The image plane of the microscope was at a distance h from the walls, exactly at the middle of the chamber with total thickness $2h$. The data clearly show a depth dependence in the scaling behavior of D_{rr}. In Figure 3.11B, the thickest chambers (in which $h > R$) were nearly flat over the entire range of R whereas the thinner chambers (in which $h < R$) exhibit an initially flat RD_{rr} at low R that begins to roll off when $R \approx h$. This demonstrates that hydrodynamic interactions with the boundaries suppresses relative displacements along the line of separation of two particles, resulting in $D_{rr} \sim 1/R^{\alpha}$ where $\alpha > 1$ for separations larger than the distance to the nearest boundary. Qualitatively similar conclusions were reached in experiments utilizing blinking optical tweezers to carefully study the dependence of particle pair diffusivity as a function of distance from the wall [33]. Thus, the range of useful R in two-point measurements is practically limited by the thickness of the chamber and this factor must be carefully considered in experimental design and data analysis.

One- and two- particle optical trap-based active microrheology measurements are also subject to the same depth considerations as passive measurements. However, they present even more stringent experimental requirements, since the need for high light gradient forces necessitates trapping to within ($< 10\mu m$) of the coverslip, and thus precludes the use of all but the highest NA oil-immersion objectives.

3.3.6 MSD Inversion procedures

Passive thermal microrheology relies on the generalized Stokes-Einstein relation (GSER), detailed in Chapter 2, to relate the probe particle MSD to the linear viscoelastic shear modulus of the material. Briefly, the GSER yields the shear modulus in terms of Laplace transformed quantities as

$$\tilde{G}(s) = \frac{k_B T}{\pi a s \langle \Delta \tilde{r}^2(s) \rangle}, \tag{3.16}$$

and in terms of comparable Fourier transformed quantities as

$$G^*(\omega) = \frac{k_B T}{\pi a i \omega \langle \Delta r^2(\omega) \rangle}, \tag{3.17}$$

where $\tilde{G}(s)$, $\tilde{G}(\omega)$ and $\langle \Delta \tilde{r}^2(s) \rangle$, $\langle \Delta r^2(\omega) \rangle$ are the Laplace and Fourier transformed shear modulus and MSD, respectively. Note that although $G^*(\omega)$ is a complex quantity with real and imaginary components, it does not contain any more information than $\tilde{G}(s)$ since both are derived from the shear relaxation modulus $G(t)$.

Image-based passive microrheology schemes typically report the MSD in terms of time, i.e., $\langle \Delta r^2(\tau) \rangle$. It is clear from Eqns. 3.16 and 3.17 that in order to determine the frequency-dependent shear modulus from $\langle \Delta r^2(\tau) \rangle$ (a procedure we term inversion), the MSD must first be converted to a frequency-space representation (Laplace or Fourier). Conventional image-based methods yield MSD data that are limited to < 5 decades of temporal dynamic range, precluding direct numerical calculation of the transform using either numerical integration or Fast Fourier Transform (FFT) algorithms. In both cases, truncation of the data introduces substantial errors

into the transformed MSD, particularly near the dynamic range extrema, which can then be propagated into the moduli.

One early approach attempted to circumvent the problem by fitting an empirical functional form to either $\langle \Delta r^2(\tau) \rangle$ or $\langle \Delta \tilde{r}^2(s) \rangle$, and then using the empirical functional form with fitted parameters in place of the experimental MSD to compute the transform analytically [70]. The weakness of this approach is that it requires the choice of an arbitrary functional form that can potentially distort the data by, for instance, smoothing out subtle features of the data. More recent approaches have instead determined $\langle \Delta r^2(\omega) \rangle$ from $\langle \Delta r^2(\tau) \rangle$ algebraically using local power law approximations [68]. The first step is to expand $\langle \Delta r^2(\tau) \rangle$ locally around the frequency of interest, ω, using a power law and retaining the leading term:

$$\langle \Delta r^2(\tau) \rangle \approx \langle \Delta r^2(1/\omega) \rangle (\omega t)^{\alpha}, \tag{3.18}$$

where $\langle \Delta r^2(1/\omega) \rangle$ is the magnitude of $\langle \Delta r^2(\tau) \rangle$ at $\tau = 1/\omega$ and

$$\alpha(\tau) = \frac{d \, \ln \langle \Delta r^2(\tau) \rangle}{d \, \ln \tau} \, |_{\tau = 1/\omega}, \tag{3.19}$$

is the power law exponent describing the logarithmic slope of $\langle \Delta r^2(\tau) \rangle$ at $\tau = 1/\omega$. In practice, the slope is obtained by fitting the logarithm of $\langle \Delta r^2(\tau) \rangle$ in a local neighborhood of each τ. Note that Eq. 3.18 is an identity if the MSD is an exact power law, i.e., $\langle \Delta r^2(\tau) \rangle \sim \tau^{\alpha}$. Thus Eq. 3.18 is a good approximation for near power law functional forms of the MSD. For thermally-driven spheres, α must lie between zero and one, corresponding to a particle embedded in a Newtonian fluid and Hookean solid, respectively. Substitution of Eq. 3.18 into the evaluation of

the unilateral Fourier transform

$$\langle \Delta r^2(\omega) \rangle = \int_0^\infty \langle \Delta r^2(\tau) \rangle e^{i\omega\tau} d\tau \approx \langle \Delta r^2(1/\omega) \rangle \int_0^\infty (\omega\tau)^\alpha e^{-i\omega\tau} d\tau, \tag{3.20}$$

leads to

$$\langle \Delta r^2(\omega) \rangle \approx (i\omega)^{-1} \langle \Delta r^2(1/\omega) \rangle \Gamma[1 + \alpha(1/\omega)] \exp[-i\pi\alpha(1/\omega)/2], \tag{3.21}$$

where Γ is the gamma function, $\Gamma(z) = \int_0^\infty \tau^{z-1} e^{-\tau} d\tau$. Substitution of Eq. 3.21 into Eq. 3.17 yields

$$G^*(\omega) = \frac{k_B T}{\pi a \langle \Delta r^2(1/\omega) \rangle \Gamma[1 + \alpha(1/\omega)]} \exp[i\pi\alpha(1/\omega)/2], \tag{3.22}$$

for the complex shear modulus. The elastic (G') and loss (G'') moduli are

$$\begin{aligned} G'(\omega) &= G(\omega) \cos[\pi\alpha(1/\omega)/2] \\ G''(\omega) &= G(\omega) \sin[\pi\alpha(1/\omega)/2] \end{aligned}, \tag{3.23}$$

where

$$G(\omega) = \frac{k_B T}{\pi a \langle \Delta r^2(1/\omega) \rangle \Gamma[1 + \alpha(1/\omega)]}. \tag{3.24}$$

Eqns. 3.23 provide physical intuition into the relation between the moduli in terms of the power law behavior of $\langle \Delta r^2(\tau) \rangle$. For the case of a Newtonian fluid, $\alpha = 1$, and the $G^*(\omega)$ is purely G''. Conversely for the limit of a Hookean solid, $\alpha = 0$ and $G^*(\omega)$ is purely G'. Note that Eqns. 3.23 and 3.24 yield an exact value for $G^*(\omega)$ whenever the MSD is an exact power

law, i.e., $\langle \Delta r^2(\tau) \rangle \sim \tau^{\alpha}$ and provide an excellent approximation for slowly varying power laws. However, when the MSD contains regions of high curvature, as in the case of the MSD for a harmonically bound particle in a viscous fluid where $\langle \Delta r^2(\tau) \rangle = r_0^2[1 - \exp(-\tau/\tau_0)]$, Eqns. 3.23 and 3.24 can be in error by $\approx 15\%$ at $\omega = 1/\tau_0$. Another limitation is that the weaker of the two moduli always contains larger error. To remedy these situations, Crocker has derived empirically modified versions of Eqns. 3.23 and 3.24 which include second order logarithmic time derivatives of the MSD [29]. This modification helps to better account for curvature, gives a better estimate of the moduli in curved regions of the data, and improves the results for the weaker component of the modulus. The scheme works best with at least 7-10 points per decade; however, it is sensitive to long wavelength ripples in the data. The modified equations that are used for extracting the moduli are

$$\begin{aligned} G'(\omega) &= G(\omega)\{1/[1+\beta'(\omega)]\} \cos\left[\tfrac{\pi\alpha'(\omega)}{2} - \beta'(\omega)\alpha'(\omega)(\tfrac{\pi}{2} - 1)\right] \\ G''(\omega) &= G(\omega)\{1/[1+\beta'(\omega)]\} \sin\left[\tfrac{\pi\alpha'(\omega)}{2} - \beta'(\omega)[1-\alpha'(\omega)](\tfrac{\pi}{2} - 1)\right] \end{aligned}, \tag{3.25}$$

where

$$G(\omega) = \frac{k_B T}{\pi a \langle \Delta r^2(1/\omega) \rangle \Gamma[1 + \alpha(1/\omega)][1 + \beta(\omega)/2]}. \tag{3.26}$$

The second-order logarithmic time derivative of the MSD is denoted by $\beta(\omega)$, while $\alpha'(\omega)$ and $\beta'(\omega)$ denote the local first- and second- order logarithmic derivatives of $G(\omega)$, i.e., $\alpha'(\omega) = \frac{d \ln G(\omega)}{d \ln \omega}$ and $\beta'(\omega) = \frac{d^2 \ln G(\omega)}{d(\ln \omega)^2}$. Crocker tested the accuracy of these equations using simulated data of the form

$$G^*(\omega) = (i\omega)^a + (i\omega)^b, \tag{3.27}$$

which broadly captures the power law crossover behavior encountered in many soft materials. Slopes of one and zero capture viscous fluids and elastic solids, respectively. The sum of the two components captures the crossover between the two extreme limits. Materials that are neither strongly elastic nor predominantly viscous will lie in the knee region of the complex modulus. The exponents a and b were varied from 0 to 1 in steps of 0.05 and the frequency range chosen for the test ranged from $10^{-5}\, rad/s$ to $10^{5}\, rad/s$. Figure 3.12 shows the error surface computed by taking the difference between the exact value given by Eq. 3.27 and the approximation given by Eqns. 3.25 and 3.26. The error is normalized by the larger of the two moduli at that frequency. The maximum error in each modulus is less than 4 % over the whole frequency range for the family of curves represented by Eq. 3.27. By contrast, the same error surface procedure using Eqns. 3.23 and 3.24 yields a maximum error of 40 % over the same parametric range.

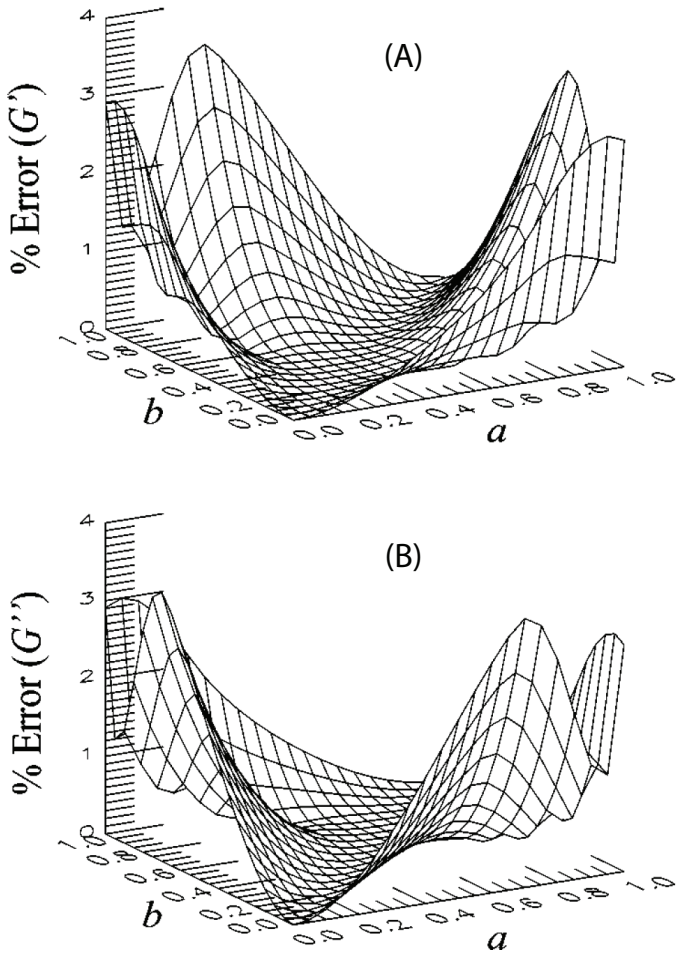

Figure 3.12: Surface plot of the maximum error over the entire frequency range of the (A) elastic and (B) viscous moduli obtained from data simulated using Eq. 3.17. The x and y axes denote the difference between the values calculated using Eqns. 3.25 and 3.26. The accuracy of the estimated elastic and loss moduli lies within 4 % of the exact value over the entire parameter space. The error is normalized by the larger of the two moduli. From Ref. [29].

3.4 Active Microrheology

The common version of active microrheology involves using an optical tweezer to grab a particle and to exert local stresses on the surrounding material in order to probe rheological response. For the active micrheology measurements of Chapter 5, we used an oscillating optical tweezer instrument built around an inverted microscope that was modified from an existing line trapping setup detailed in [110]. Electronic detection was added to the setup based in large part on the scheme developed by the Ou-Yang group [48, 108].

3.4.1 Optical Tweezers

The use of a highly focused beam of light to trap micron-scale dielectric particles was pioneered by Ashkin and coworkers at Bell Labs in the 70's and 80's [7, 8]. Since then, optical tweezers have become a standard tool for measuring and manipulating sub-picoNewton scale forces on micron scale objects. It has enabled many notable discoveries in biological systems [73]. It has also been employed in various forms for measurement of colloidal interactions across a wide range of soft materials [25, 45, 72]. In the soft matter community, recent innovations using holographic methods to generate multiple steerable traps have provided a powerful suite of tools for probing soft materials [28, 42]. A detailed review of the principles and technical aspects of optical trapping can be found in Ref. [77].

An optical trap is formed by tightly focusing a laser beam with an objective lens of high NA. When such a beam is focused near a dielectric particle, it exerts two kinds of optical forces on the particle: (1) a scattering force which pushes the particle in the direction of propagation of the light beam and (2) a gradient force which pulls the particle in the direction of the light

intensity gradient. The scattering force arises from a net momentum transfer to the particle from the photons impinging on it. The gradient force arises from the fact that a dipole in an inhomogeneous electric field experiences a force in the direction of the field gradient. In an optical trap the laser effectively induces fluctuating dipoles within the particle which interact with the field (also oscillating at some frequency). In order for the particle to be stably trapped by the beam in three dimensions, it is necessary for the axial component of the gradient force to exceed the axial component of the scattering force. This condition requires a very steep gradient produced by sharply focusing a laser beam to a diffraction-limited spot using a high-NA objective. Once trapped, the particle can be held in position and manipulated by moving the focus of the laser beam. When the particle experiences slight displacements from the focus of the light beam, it experiences a restoring force which push it back toward the focus (Figure 3.13). For small displacements (Δx), the trap acts as a Hookean spring whose characteristic stiffness (k) is proportional to the light intensity (I_0), i.e., $F_{trap} = -k\Delta x$, where $k \propto \nabla I_0$.

Theoretical descriptions of F_{trap} are usually given in two limiting regimes: (1) the ray optics regime wherein the radius of the particle is much greater than the wavelength of the light, $a \gg \lambda$, and (2) the Rayleigh scattering regime when $a \ll \lambda$. In the first case, the net force on the particle can be calculated by summing the momentum change experienced by the particle as it refracts each incident ray. When the index of the particle is higher than the medium, the net force on the particle is always in the direction of increasing intensity gradient, as shown in Figure 3.13. The opposite situation in which the particle has lower n than the medium results in the particle being pushed away from the intensity gradient maximum. A complete mathematical description of the resulting force can be found in Ref. [103]. For case (2), the particle can be approximated

as a point-like dielectric sphere and the total force exerted by the trap is readily separated into a scattering force (F_{scatt}) and gradient force (F_{grad}) given by [8]

$$F_{trap} = F_{scatt} + F_{grad} = \frac{\mathbf{E}^2}{c}\frac{128\pi^5 a^6}{3\lambda^4}\left(\frac{m^2-1}{m^2+2}\right)^2 n_0 - \frac{n_0^3 a^3}{2}\left(\frac{m^2-1}{m^2+2}\right)(\nabla \mathbf{E})^2, \quad (3.28)$$

where n_0 is the index of the medium and m is the ratio of the index of the particle to the index of the medium (n/n_0).

In practice, Eq. 3.28 is useful to get a qualitative sense for how the trapping force depends on various physical parameters, but it is not exact. This is due to the fact that most particles of interest fall into an intermediate size range (0.1 - 10λ) where neither regime is strictly valid. Nonetheless, Eq. 3.28 reveals the balance of microscopic parameters that control the optical trap's stiffness. It is clear from Eq. 3.13 that in order to make a stronger trap, one should maximize the NA, the laser power, and index mismatch between the particle and medium. Trapping as close to the laser as possible is also important, because longitudinal spherical aberration increases with depth into the sample, distorting the beam profile and degrading trap stability.

From Figure 3.13 we see that if the particle moves out of the beam focus, restoring forces act to pull it back to the focus. Consequently, if the trap is scanned back and forth within the image plane, then the particle should follow the focus provided the scanning is sufficiently slow. However, if the trap moves too fast then the particle will not be able follow the trap and will escape from the trap. The criteria for the speed is given by the balance of the the Stokes drag force $F_{Stokes} = 6\pi\eta a v$, where η is the viscosity of the medium, and F_{trap}. This is the conceptual basis behind using an oscillating optical trap for active microrheology; in the simplest case of

a particle in a viscous fluid, the velocity with which the particle escapes from the trap yields a measurement of the viscosity, provided k and a are known. A natural generalization of this basic measurement to soft materials having a complex, frequency-dependent viscosity $\eta^*(\omega)$ is to scan the trap sinusoidally for a range of frequencies and to measure the displacement and phase of the particle in response to the trap. The details of this scenario have been worked out previously in the active microrheology section of Chapter Two (Section 2.4).

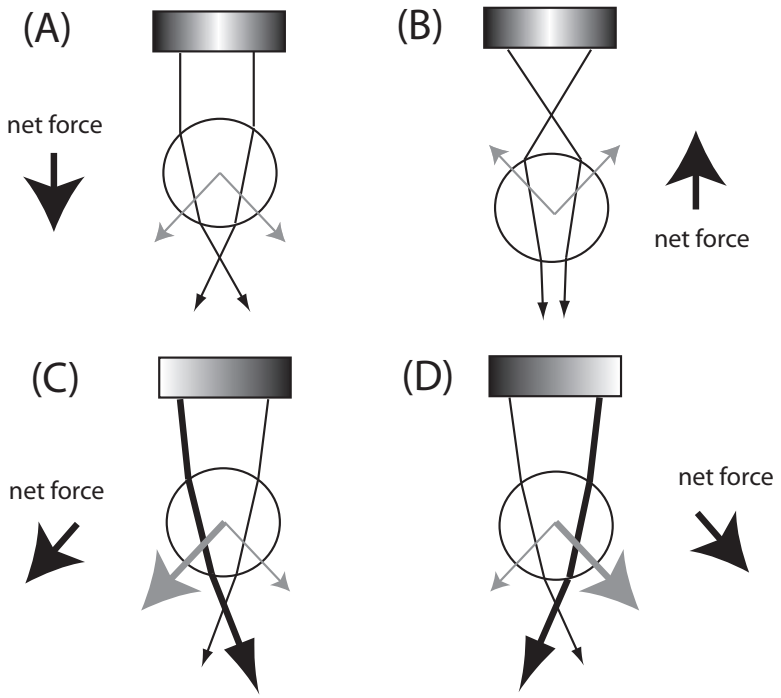

Figure 3.13: Ray optics description of the forces on a dielectric sphere with higher index of refraction than the medium. The boxes above the spheres represents the light gradient where white is high intensity and black is low intensity. Two rays from the light source (represented by black lines of different thicknesses) are shown. The refraction of the light by the bead changes the momentum of the photons equal to the change in direction of the incident and refracted rays. By Newton's third law, the momentum of the bead must change by an equal amount, exerting a equal and opposite force on the bead shown by the grey arrows. (A) The particle sits below the laser focus and the net force pushes the particle toward the focus. (B) The particle sits in front of the focus and the net force pulls the particle up toward the focus. In (C) and (D) the particle is off-axis relative to the beam intensity maximum and the net lateral force brings the particle back toward the beam intensity maximum. In all cases, the net forces bring the particle back to the stable equilibrium point at the focus of the beam.

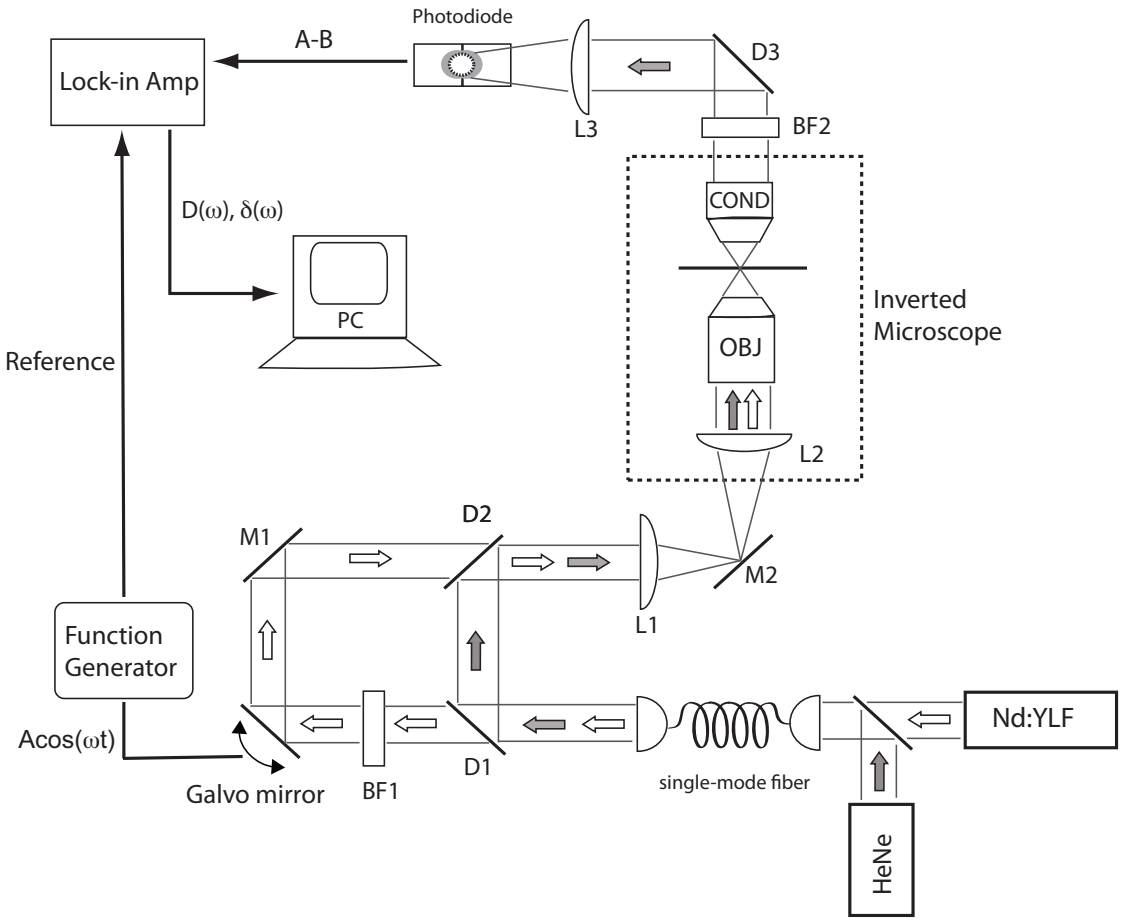

Figure 3.14: Schematic of oscillating optical tweezer setup. The trapping laser (Nd:YLF $\lambda_t = 1054\,nm$) and detection laser (HeNe $\lambda_d = 633\,nm$) are coupled into a single-mode optical fiber. The emitted, collimated light from the fiber containing both wavelengths is split by a dichroic mirror (D1) which transmits λ_t and reflects λ_d. The trapping component is passed through a barrier filter (BF1) which further attenuates λ_d before going into a galvanometer-driven scanning mirror set to sinusoidally oscillate at frequency ω by a function generator. The trapping component is directed by a fixed mirror (M1) into an identical dichroic mirror (D2) which co-linearly recombines the oscillating trapping laser and stationary detection laser. The two components are steered into a Zeiss inverted microscope with a fixed mirror (M2) situated between a telescope lens pair (L1-L2) which expands the beam to overfill the back aperture of the microscope objective (OBJ). The back aperture is conjugate to the galvo-mirror such that small deflections of the mirror results in translation of the trapping laser's focus in the image plane. The beam is collected by the condenser (COND) and the trapping component is attenuated by passing through a barrier filter (BF2) and dichroic mirror (D3). The detected component consists of the "shadow" of the moving trapped particle illuminated by the stationary detection beam. The detected component is projected with a collection lens (L3) onto a split photodiode. The A-B voltage components of the split PD are fed into a lock-in amplifier which extracts the components of the differential voltage signal at frequency ω via the reference signal from the function generator. The DC analog outputs of the lock-in are contain the displacement and phase shift of the signal ($D(\omega)$, $\delta(\omega)$) which is digitized using a PC running Labview.

The experimental setup for our active microrheology measurements reported in Chapter Five is shown in Figure 3.14. To create the trap, we used the CW output of an Nd:YLF laser (Quantronix) at its fundamental frequency $\lambda = 1054\,nm$. We also used a HeNe laser (Hughes) that is collinear with the IR trapping beam to provide a stationary reference for detecting the displacement of the particle in the lab frame. Both lasers are coupled into a single mode fiber before entering the active optical train of the setup. The fiber serves two important purposes: (1) to act as a spatial filter to clean up the beam and, more importantly, (2) to ensure that the trapping beam is a TEM_{00} mode having a Gaussian intensity profile that is optimal for stable trapping.

After entering the active optical train, the $\lambda_d = 633\,nm$ detection component and the $\lambda_t = 1054\,nm$ trapping component are separated so that the trapping beam can be scanned by the galvanometer-driven mirror independent of the detection beam. To accomplish this, a dichroic mirror (D1) reflecting 633 nm and transmitting 1054 nm is placed into the beam path. A subsequent barrier filter (BF1) further attenuates any residual 633 nm remaining in the trapping beam's optical path. The galvo-mirror is conjugate to the back focal plane of the objective, with the result that small deflections of the mirror (driven via a function generator) translates the trap's focus in the image plane. In our measurements, we typically drive the mirror to displace the trap with a sinusoidal amplitude $A = 0.25\mu m$. Using $a = 2\mu m$ PS particles, this induces $A/a = 0.25\mu m/2.0\mu m = 12.5\%$ maximum strain at the particle level.

After the scanning mirror, the trapping beam is steered (M1) to recombine with the detection beam at dichroic mirror (D2). The combined beam is then expanded using a telescope pair (L1-L2) to overfill the BFP of the objective and steered into the fluorescence port of an inverted microscope (Zeiss Axiovert 135). The power of the trapping laser is typically $\approx 40mW$ going

into the objective while the detection beam is typically $\approx 10\mu W$. The trapping is monitored via the microscope's bright field (transmitted) light imaging setup (not shown). Once trapped, the forward scattered light from the detection laser on the trapped particle forms a geometrical "shadow" which is collimated by the condenser. Note that for our $2a = 4\mu m$ particles, the forward scattered light is very shadow-like owing to the fact that we are in the ray-optics regime ($a > 633nm$). Whereas for smaller particles ($a \approx 633nm$), the forward scattered image is more closely resembles interference fringes rather than a circular shadow. To eliminate crosstalk, the IR trapping component is removed via a barrier filter (BF2) and dichroic mirror (D3) before being projected onto a split photodiode (Hamamatsu S4204). The split photodiode is centered so that when the trapped particle is not oscillating, the voltage difference between the two halves |A-B| is minimized. The voltages from the two halves of the split are then fed into a Lock-in amplifier (SR530, Stanford Research Systems) which extracts the displacement $D(\omega)$ and phase $\delta(\omega)$ at frequency ω by homodyning the A-B difference voltage signal with the function generator reference, followed by low-pass filtering. The output of the lock-in is digitized onto a PC running Labview.

Chapter 4

Rheological Microscopy: Bulk and Local Properties from Microrheology

4.1 Introduction

The microscopic propagation of force in mechanically inhomogeneous materials is central to many issues in condensed-matter research, including force chains in granular and jamming materials, dynamical heterogeneity in glassy systems, and the behavior of nanocomposite materials. In a different vein, cell biologists have discovered that many aspects of a cells gene expression, locomotion, differentiation, and apoptosis are governed at least in part by the stress and elasticity of its surroundings, through a coupling of intracellular stress and biochemical signaling pathways. Experimental methods for directly studying microscopic stress and viscoelasticity, however, have been slow to appear.

The past decade has seen the development of microrheology, which uses tracer motion to

assess rheology in much smaller samples and over a broader range of frequencies than conventional rheometry. Typically, the frequency-dependent shear modulus of a material is derived by tracking the driven [34, 49] or thermal [40, 69, 70, 93, 120] motions of embedded micron-sized tracers. To date, microrheology has been applied to biopolymer solutions [40, 69, 70, 93], concentrated emulsions [70], gels [19, 55], and the cytoskeleton of living cells [34, 57]. Tracers naturally probe viscoelasticity on length scales comparable to their size. In materials that are heterogeneous on these scales, tracer motion depends on both the local and the bulk rheology in a complex way [59, 61]. This fact has largely precluded the use and interpretability of microrheology in mechanically heterogeneous materials where such microscopic information is most needed.

In this chapter, we introduce and demonstrate an analytical framework to separately determine the local and the bulk mechanical properties from microrheology data. We call the method "rheological microscopy." Elaborations of this approach provide routes to understanding nonuniform force propagation in a variety of heterogeneous media. We demonstrate rheological microscopy on a model system of polystyrene spheres in an aqueous semidilute solution of nonadsorbing, monodisperse semiflexible polymer λ-DNA. Previous experiments have characterized this model semidilute polymer solution, determining correlation length and, ergo, the microstructure of the depletion layer surrounding the embedded particles, as a function of polymer concentration [111,112]. Measurements were performed at a variety of sphere diameters and polymer concentrations, permitting us to vary the bulk solution viscoelasticity and the depletion layer thickness relative to the particle size. Experiments reveal the extent of the rheologically

distinct layer, which was approximately 2 times the correlation length in the semi-dilute polymer solution, significantly different from the predictions of mean-field theory. The computed bulk rheology is in excellent agreement with independent measurements made using two-point microrheology [26].

4.2 Background

4.2.1 Depletion

In a binary suspension of small and large hard-spheres interacting via steric interactions alone, there exists a spherical shell around the large particles with thickness $\approx a_s$, the radius of the smaller particle, from which the smaller particles are excluded [see Figure 4.1A]. This "depletion layer" exists because the particles are rigid and the smaller particles cannot approach the larger particles within a distance a_s without interpenetration or deformation. This fact has dramatic consequences for phase behavior of the suspension. One immediate consequence is that when two larger particles are close enough such that their depletion layers overlap, then there will be an imbalance of forces on the particles between the overlapping and non-overlapping regions and this leads to a net force that pushes them together, as shown in Figure 4.1B. The depletion force range is typically short ranged, $\approx 2a_s$. There are two equivalent descriptions of the depletion force. One is in terms of osmotic pressure imbalances, as we have presented above. The other is in terms of entropy: when the two large spheres are driven together the loss in their configurational entropy is offset by the gain in entropy for the small spheres, resulting in a net gain of entropy for the entire system. The gain in entropy of the small spheres is due to the gain in their free volume and is thus proportional to the overlap volume of the depletion layers

surrounding the large spheres.

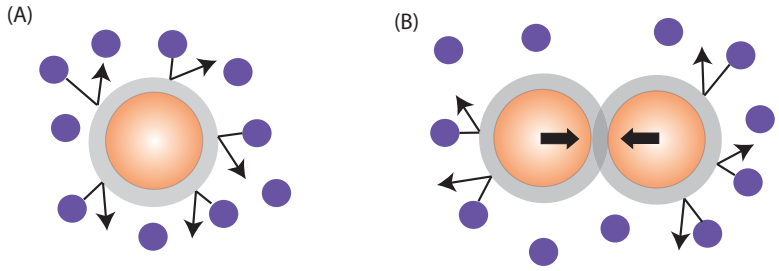

Figure 4.1: Depletion in a binary suspension of hard spheres. (A) Isolated large sphere of radius a_L is bombarded isotropically by small spheres of radius a_s. A spherical shell of thickness a_s surrounds the large sphere (shaded region) corresponding to a depletion layer where the centers of small spheres cannot penetrate due to hard sphere interactions. (B) Two large spheres approach such that their excluded volume regions overlap, leading to an imbalance of collisions with small spheres between the overlapping and non-overlapping regions. A net attraction between the larger spheres ensues.

A dilute polymer solution can be modeled as an ideal gas of hard spheres with a mean size given by the radius of gyration of the individual polymer coils, R_g. The case of attractive interactions between two spheres in a dilute polymer suspension was first considered theoretically by Asakura and Oosawa (AO) [6]. Unlike hard spheres, polymers in solution can interpenetrate, significantly reducing any effects due to liquid structure [25]. The experimental situation is depicted in Figure 4.2A. The centers of the polymer "spheres" are excluded from a region of thickness R_g surrounding the colloidal particles. When the depletion layers surrounding the two spheres overlap, the free volume accessible to the polymer increases, leading to a gain in the system entropy. This produces an attractive interaction between the two spheres. When the polymer concentration is increased above the critical overlap concentration, c^*, entanglement effects become important. In this semidilute regime the polymer is characterized by a correlation length ξ rather than by R_g. The length scale ξ may be thought of as the average spatial distance between two neighboring entanglement points. The correlation length decreases with

increasing concentration above c^*, scaling as $\xi \sim c^{-1/2}$. Equivalently, ξ describes the mean size of a "blob" [30] within which a section of the polymer chain still behaves as an independent coil, as illustrated in the inset of Figure 4.2B. If the polymer-colloid interaction is repulsive, a "depletion layer" with a thickness proportional to ξ [see Figure 4.2B] develops around each sphere. A suite of experiments utilizing line-scanned optical tweezers to quantititatively measure the ensuing attractive potential between colloidal spheres immersed in suspensions of λ-DNA provided strong evidence that depletion occurs well into the semidilute regime and exhibits scaling consistent with the AO model using blobs of radius $\approx \xi$ in place of R_g [110–112]. Thus, depletion interactions are a robust phenomena in colloidal mixtures.

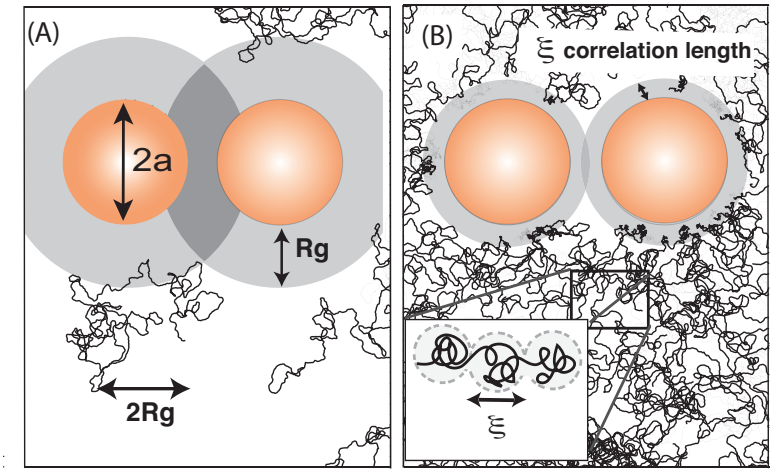

Figure 4.2: Polymer depletion in the (A) dilute and (B) semi-dilute regimes [111]. The shaded region around the particles corresponds to the depletion layer and the overlap region corresponds to the free volume accessible to the polymer.

In our experiments, we use the particle and depletion layer as a model system to test the predictions of the electrostatic analogy of Levine and Lubensky discussed in Section 2.3.8. Indeed, the particle and depletion layer closely resembles idealization of the shell model depicted in Figures 2.11 and 4.6C. Our system is ideal for testing the theory because both particle size and

depletion layer thickness can be varied independently. The depletion layer thickness is set by the concentration of DNA . For this situation we expect that the one-point MSD (MSD1) will be larger than the two-point MSD (MSD2), as is indeed observed in our raw MSD data for a typical concentration used in our experiments [see Figure 4.3]. This suggests that the MSD1 is more sensitive to the local shell than the MSD2, which probes the bulk DNA solution. As a control, we also plot the MSD1 and MSD2 for a particle in water and find, as expected, MSD1 = MSD2.

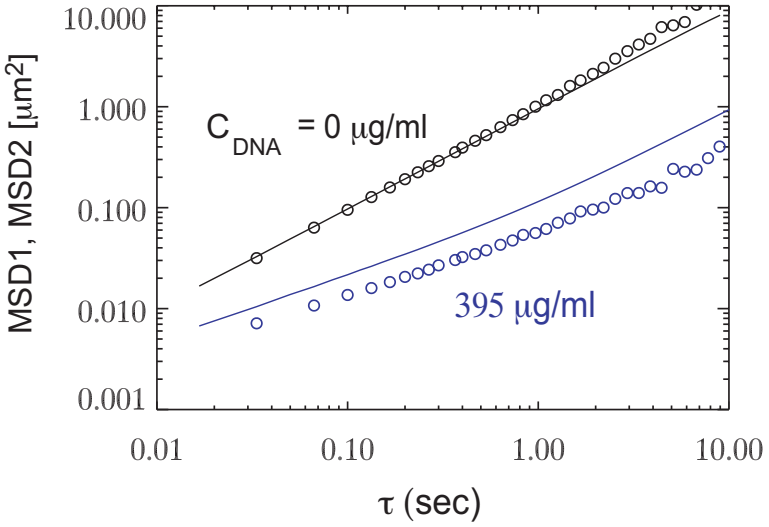

Figure 4.3: MSD1 (lines) and MSD2 (circles) for $2a = 0.97\mu m$ tracer particles in two samples: one with no DNA (top) and one with $c_{DNA} = 397$ μg/ml (bottom). MSD1 = MSD2 as expected for the no DNA control sample whereas MSD1$>$ MSD2 for the $c_{DNA} = 397$ μg/ml sample.

4.3 Sample Preparation

Our experiments were carried out on solutions of bacteriophage lambda DNA (λ-DNA; New England Biolabs Inc.) whose single-stranded ends were filled in with standard techniques [90], suspended in a 10 mM TE buffer (10 mM tris-HCl, 0.1 mM EDTA, pH = 8.0). λ-DNA has a persistence length of 50 nm, a contour length of 16.5 μm and a radius of gyration of $R_g \sim 500$nm

[111]. We worked with four semi-dilute DNA concentrations ($30, 104, 190, 397\mu$g/ml). The polymer correlation length has been measured to be $350, 190, 130,$ and 90 nm, respectively, for these concentrations [111]. The critical overlap concentration c^*, is roughly $30\ \mu$g/ml [81]. Thus all our samples, except the lowest concentration ($30\,\mu$g/ml) are well in the semidilute regime ($c > c^*$) .

We used fluorescent beads as tracers (Molecular Probes, Rhodamine Red-X labeled carboxylate-modified polystyrene). Beads of three different diameters ($2a = 2.0, 0.97, 0.46\ \mu$m) were dispersed in the DNA solutions at a volume fraction, $\phi \sim 10^{-4}$. D_2O was used for density matching. We imaged the samples either with bright field microscopy ($2a = 0.97\mu$m) or epi-fluorescence microscopy ($2a = 0.46, 2.0\mu$m), with the temperature controlled to 28°C. We used a 63X water-immersion objective (NA = 1.2) for the samples with 0.46 and 0.97 μm tracers and a 20X (NA = 0.7) multi-immersion objective for the sample with 2.0 μm tracer, adjusting the particle volume fraction so there were about 100 tracers in each image. For the two largest particle sizes and two highest polymer concentrations the number of usable tracers fell to ~ 50 due to the formation of depletion-induced aggregates, which were screened automatically by our analysis software. To minimize wall effects, we focused roughly 60 μm into the 120 μm thick sealed sample chambers. To avoid skewing the dynamics, we used a 2 msec shutter setting on our NTSC video camera. After recording on an S-VHS video deck, the images were digitized and analyzed off-line, using methods described in Chapter 3. One hour of video was recorded for each sample yielding $\sim 10^7$ particle positions with 20 nm spatial resolution and 1/60 second temporal resolution.

4.4 Results and Discussion

In Figure 4.4 we exhibit the MSD1 and MSD2 for the three different particle sizes at the highest DNA concentration (397 μg/ml, $c \sim 13\,c^*$). We have rescaled both sets of curves by $a/2\tau$ in order to highlight the deviations from diffusion wherein the MSD $\sim \tau$, resulting in a horizontal line in this rescaled plot. Both MSDs exhibit functional dependencies on τ which are typical of weakly entangled polymer solutions descibed by a Maxwell-type model (described in Chapter 2). At early lag times, the subdiffusive behavior ($\sim \tau^{\alpha}, \alpha \leq 1$) of the MSDs reflect an elastic response arising from topological entanglements in the polymer network. At longer times, the MSDs approach diffusive behavior and become horizontal, reflecting the relaxation of entanglement stresses via a reptation mechanism [30, 32, 87]. The two-point data (MSD2) collapse onto a single curve, separated from the one-point data. This is expected since the MSD2 probes the longer length scale bulk properties of the solution, independent of particle size.

The collapse enabled us to globally determine a master MSD2 curve for each concentration by averaging the individual MSD2 obtained from different particle sizes. This effectively extends the temporal range of the smallest particles' trajectories, which was limited as a result of their more rapid diffusion out of the focal plane. The one-point data differ primarily because the particle to depletion cavity size ratio differs for the different particle sizes. Agreement between MSD2 and MSD1 is best for the largest particle size where the ratio of particle-plus-depletion layer diameter to particle diameter is closest to unity. The disagreement reflects an effective "slip" between the particles and the bulk DNA network, due to depletion.

We determined the frequency-dependent complex shear moduli ($G_1^*(\omega), G_2^*(\omega)$) using the

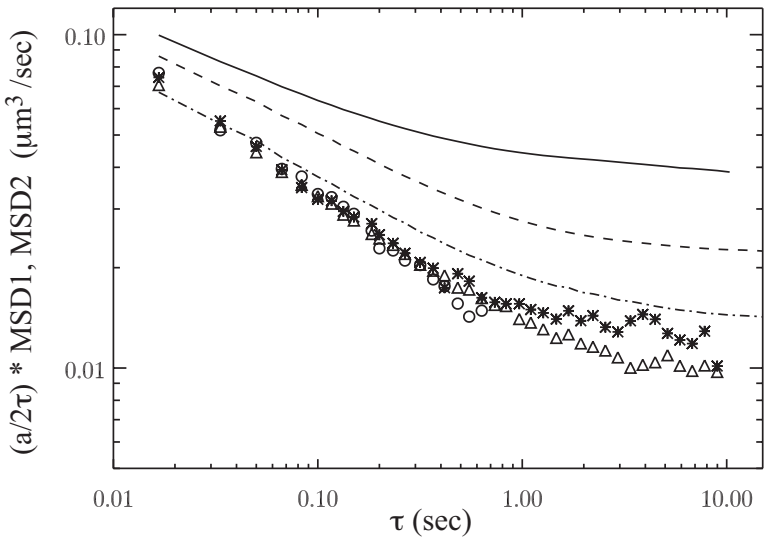

Figure 4.4: MSD1 (lines) and MSD2 (symbols) rescaled by $a/2\tau$ for fixed DNA concentration (397 μg/ml, $c \sim 13\,c^*$) and varying particle size [see text]. Solid, dashed, and dot-dash lines are MSD1 for $2a = 0.46, 0.97,$ and 2.0 μm respectively. Circles, triangles, and stars are MSD2 for $2a = 0.46, 0.97,$ and 2.0 μm respectively. Notice, the MSD2 data collapse onto a single master curve under the rescaling whereas the MSD1 data do not.

procedure described in Section 3.3.6. Figure 4.5A shows the results for three particle sizes derived from MSD1 and the master MSD2 for a DNA concentration of 397 μg/ml ($c \approx 13\,c^*$). Figure 4.5B shows the moduli for the next lower concentration, 190 μg/ml ($c \approx 6\,c^*$). In both cases the one-point measurements produce a family of curves that are clearly displaced from one another, and from the two-point results. From this observation, we infer that the G_1 underestimates the bulk moduli to a greater degree as particle size decreases.

Levine and Lubensky have computed both the effective one- and two- particle viscoelastic response functions for a minimal model of depletion layer inhomogeneity –tracers surrounded by shells whose rheological properties differ from the bulk [61]. The major parameters of the model are defined in Fig. 4.6C, including the particle-cavity composite radius $b = a + \Delta$, the local cavity shear modulus G^*_{loc}, and the bulk shear modulus G^*_{bulk}. Using the electrostatic analogy

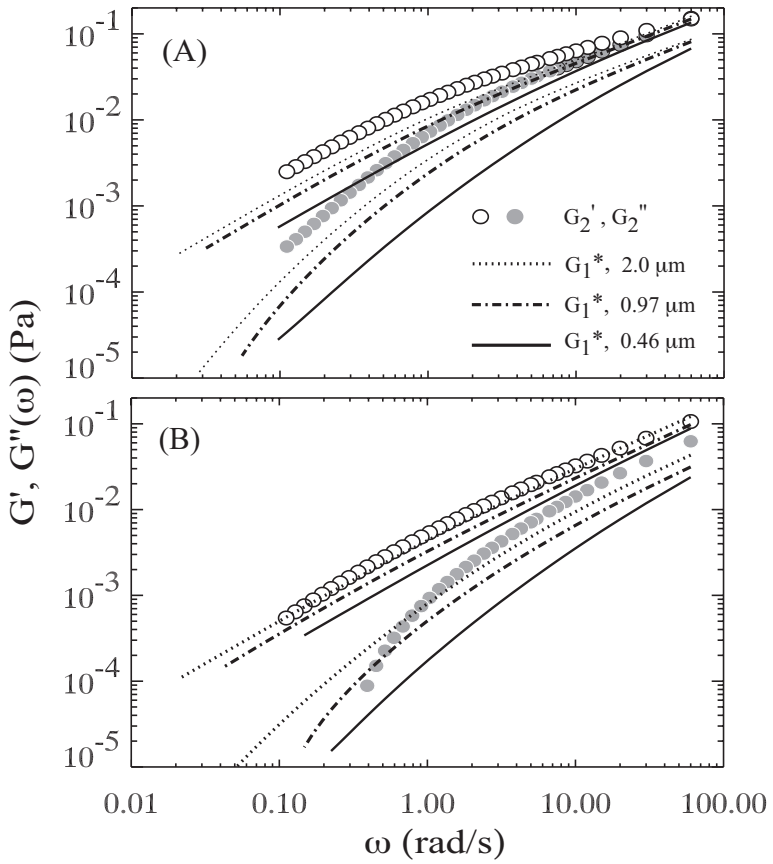

Figure 4.5: (A) MSD1 and MSD2-derived bulk shear moduli $G_1^*(\omega), G_2^*(\omega)$ for $c_{DNA} = 397$ μg/ml, and different particle sizes. G'' (open circles), G' (filled circles) from master MSD2. Dotted, dash-dot, solid lines are G_1^* for $2a = 2.0, 0.97, 0.46$ μm particles respectively. The upper group of lines are G'' while the lower group are G'. (B) $G_1^*(\omega), G_2^*(\omega)$ for $c_{DNA} = 190$ μg/ml.

elaborated in section 2.3.8, they demonstrated that two particle correlations for $R \gg a, b$ reflect predominantly the bulk responses whereas the single particle measurement is sensitive to both bulk and local rheologies. They provide a formula relating the one- and two- point microrheology derived shear moduli ($G_1^*(\omega), G_2^*(\omega)$). For a shell model assuming incompressibility, they find

$$\frac{G_2^*(\omega)}{G_1^*(\omega)} = \frac{4\beta^6\kappa'^2 - 9\beta^5\kappa\kappa' + 10\beta^3\kappa\kappa' - 9\beta\kappa'^2 - 15\beta\kappa' + 2\kappa\kappa''}{2[\kappa'' - 2\beta^5\kappa']}. \tag{4.1}$$

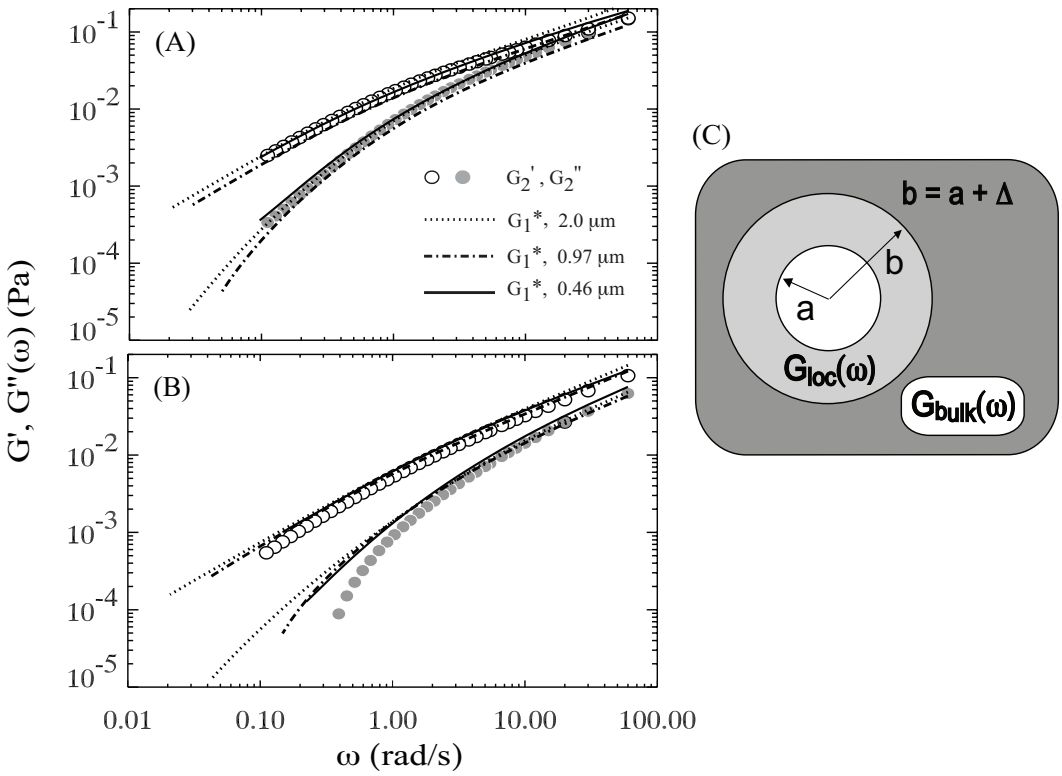

Figure 4.6: (A) $G_2^*(\omega)$ obtained from shell model using the collapse of the G_1 data for $c_{DNA} = 397$ μg/ml. Circles are the measured G', G'' (open, filled). Lines are different particle diameters 2.0, 0.97, 0.46 μm (dotted, dash-dot, solid). Lines were computed from Eq. 4.1 using an effective shell thickness Δ = 194 nm and solvent viscosity η_0 = 0.94 mPa s assuming $G_{loc}^*(\omega) = -i\omega\eta_0$. The lines agree with the measured bulk moduli from two- point, $G_2^*(\omega)$ (open, filled circles). (B) Results for $c_{DNA} = 190$ μg/ml obtained with Δ = 336 nm. (C) Shell model of Levine and Lubensky [61].

Here $\beta = a/b$, $\kappa = G_{bulk}^*(\omega)/G_{loc}^*(\omega)$, $\kappa' = \kappa - 1$, and $\kappa'' = 3 + 2\kappa$. Rheological microscopy uses this relation along with our one- and two- point measurements to probe the depletion- induced mechanical heterogeneity.

If the shell model is valid, then the $G_2^*(\omega)$ generated from the $G_1^*(\omega)$ using Eq. 4.1 for different particle diameters should collapse onto each other for a value of the shell thickness Δ that corresponds to the effective depletion layer thickness for a given concentration, independent of particle size. Our scheme for rheological microscopy in this paper aims to find an effective

layer thickness Δ from the 'blind' collapse of the synthetic $G_2^*(\omega)$ determined for different tracer diameters. We expect the Δ to be on the order of the correlation length ξ of the DNA solutions based on a simple model of the viscosity dependence with distance from a planar wall for non-adsorbing flexible polymers [61] (see Figure 4.7B). Furthermore, we expect the curves to collapse onto the bulk modulus $G_{bulk}^*(\omega)$, inferred here from the measured $G_2^*(\omega)$. This approach thus affords a simultaneous determination of the spatial extent of the depletion cavity and the bulk rheological response from one-point microrheological data.

We determined the collapse of the data for our three particle sizes by treating Δ as a free parameter in the minimization of the standard deviation of the synthetic $G_2^*(\omega)$. We assume that the local modulus is predominantly that of a viscous fluid with the viscosity of the solvent, namely $G_{loc}^*(\omega) = -i\omega\eta_0$ with η_0 = 0.94 mPa s. In Figure 4.6A we exhibit the results of the minimization for c_{DNA} = 397 μg/ml where $c \approx 13\, c^*$. We found the collapse to be nearly perfect with Δ = 194 nm. Significantly, the crossover of G' and G'', which reflects a typical relaxation time for the network, is captured in the measured and one-point derived G_2 but undetected in the raw G_1 data. As a further check of our method, we apply it to the next lower concentration c_{DNA} = 190 μg/ml where $c \approx 6\, c^*$. The results, exhibited in Figure 4.6B, again show a good agreement between all particle sizes and two-point results. The fact that the synthetic G_2 agrees with the $G_{bulk}^*(\omega)$ determined from two-point microrheology verifies the applicability of the shell model for a polymer network with depletion induced inhomogeneities.

Lastly, we relate the Δ to our previously measured ξ for all our concentrations. In Figure 4.7A we show a plot of Δ vs ξ. Our values for Δ are closer to $2\,\xi$ (dotted line in Figure 4.7A) suggesting that the "rheological" cavity size for the depleted particles are of order ξ, albeit a bit

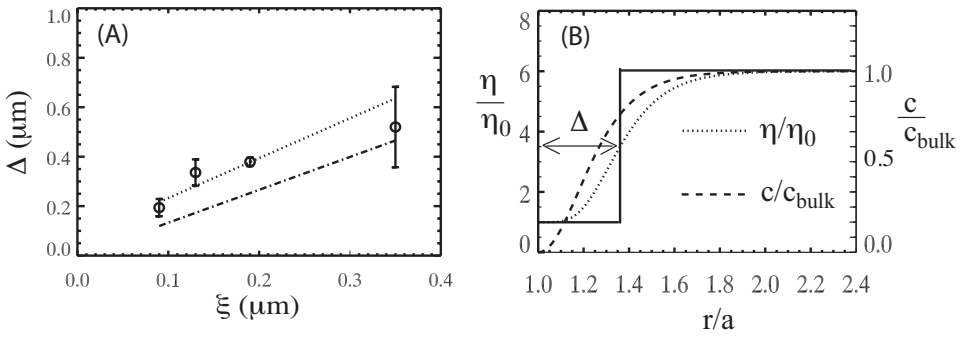

Figure 4.7: (A) Effective layer thickness Δ determined from optimal collapse of the G_1 data for all particle sizes vs measured correlation length ξ. Dash-dot line: $\Delta = 1.33\,\xi$. Dotted Line: $\Delta = 2\,\xi$. (B) Variation of solution viscosity (dotted line) and DNA concentration (dashed line) with dimensionless distance from the sphere for $c = 190$ μg/ml, $2a = 0.97$ μm. The width at half maximum of the viscosity profile is used to define an effective cavity thickness Δ for the shell model (solid line).

larger. A naive mean field treatment (see the width-at-half-max of the local viscosity in Figure 4.7B) leads to $\Delta = 1.33\,\xi$, which is drawn with the dash-dot line. We see that our values for Δ are closer to $2\,\xi$ as shown with the dotted line. This overestimation of the Δ could arise from hydrodynamic penetration of the bead-induced solvent flow into the outer shell, as illustrated in Figure 4.8. Thus, Δ is a rheological slip length corresponding to the distance at which the velocity field of the fluid hydrodynamically "locks in" to the network rather than the correlation length characterizing the static thickness of the depletion layer. This higher-order effect is not captured in the shell model.

4.5 Conclusion

We have demonstrated that concurrent one- and two- point microrheological measurements and theory can be used to determine the local microstructure of the depletion induced layers surrounding a tracer particle embedded in a semi-dilute polymer solution. Our results furthermore

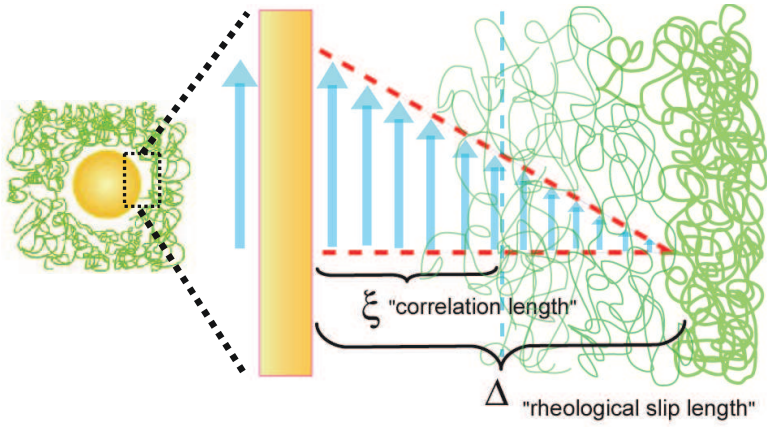

Figure 4.8: Cartoon illustrating difference between rheological slip length Δ and correlation length ξ in the depletion layer of a moving particle.

show that conventional one-point microrheological measurements can be applied to extract the bulk viscoelastic modulus, a quantity which has heretofore been unambiguously accessible only to two-point measurements in such systems. Equivalently, if one has knowledge of the cavity size, the local rheological properties of the layers can be deduced in an analogous way. Refinements, both theoretical and experimental, of the basic 'rheological microscopy' method we have presented here should enable its extension to the study of more complex media.

Chapter 5

Fluctuations and Rheology in Active Bacterial Suspensions

Support Bacteria. They're the only culture some people have.

Steven Wright

5.1 Introduction

Active complex fluid systems such as living cells [15, 57], assemblies of motors and filaments [41], flocks of birds [105], and vibrated granular media [75] differ from conventional equilibrium media in that some of their components consume and dissipate energy, thereby creating a state that is far from equilibrium. An understanding of model active systems, even at a phenomenological level, provides insight about fundamental non-equilibrium statistical physics and, potentially, about the inner workings of biological systems. Bacterial baths [12, 96, 106, 118] are

attractive model active systems because energy input is homogeneous, because individual bacteria can be directly observed, and because critical parameters such as density, activity, and swimming behavior can be brought under experimental control. Earlier experiments have reported on a rich variety of non-equilibrium phenomena in this system class including anomalous diffusion [118] and pattern formation [79, 106], while theories of self-propelled organisms readily predict ordered phases such as "flocks" [104],

In this chapter, we describe microrheological measurements of the fluctuations and mechanical responses of an active bacterial suspension. In contrast to previous work [96, 106, 118], we concurrently measure the one- and two-point correlation functions of embedded passive tracer particles to assess material fluctuations over a wide range of length scales. We found that, similar to equilibrium systems such as the λ-DNA of Chapter 2, one-point measurements are sensitive to the local environment of the probe while two-point measurements automatically average over system inhomogeneities and provide an unambiguous measure of the parameters characterizing the bulk rheological properties of the bacterial bath. Whereas previous tracer-based measurements on bacterial baths have exclusively utilized one-point approaches, our results raise new questions about the applicability of one-point measurements as a probe of bacterial dynamics. We independently measure the effective viscosity of the bacterial bath by using optical tweezer-based active microrheology as described in Chapter 3. We found that even at a low volume fraction ($\phi \sim 10^{-3}$) of bacteria, fluctuations in the medium are substantially greater than they are in the absence of bacteria while rheological response is unchanged, implying a breakdown of the fluctuation-dissipation theorem (FDT). This confirms that the bacterial bath is a far-from-equilibrium system.

We found that he mean-square displacements (MSDs) of tracer particles as a function of lag time Δt, depend strongly on swimming behavior. For wild-type bacteria that both run and tumble, the MSD extracted from two-point correlations scale superdiffusively as $\Delta t^{3/2}$ over the time scale of our experiments, and the stress power spectrum $\Delta(\omega)$ [57] as a function of frequency, ω, scales accordingly as $\phi/\sqrt{\omega}$. For constitutively tumbling bacteria, by contrast, both one- and two-point MSDs exhibited a crossover between super-diffusive and diffusive regimes that could be completely characterized using a *single* time-scale, τ, and the $\Delta(\omega)$ was well-described by a functional form a constant plus a Lorentzian with a knee frequency $\approx 1/\tau$.

5.2 Background

Many species of bacteria, such as *E. coli* are rodlike, single-celled organisms that actively navigate their environment by swimming [12]. A common mechanism for motility is based on the rotation of bacterial flagella propelled by the action of rotary motors embedded in the cell wall. When all the motors rotate counterclockwise, the flagella bundle up and propel a bacterium forward in the direction of its long axis. This is called a "run". When some of the flagella rotate clockwise, the flagella unbundle and the cell body spins or "tumbles". These motions are illustrated in Figure 5.1. Tumbles randomize the bacterium's swimming direction. By "tasting" its local environment and using the chemical signal to tune the relative frequencies of runs and tumbles, a bacterium is able to direct its average motion toward increasing spatial nutrient gradients, a process known as chemotaxis. On average, a bacterium tumbles for about 0.1 s before it "runs" in a different (random) direction; the typical run time is about 1-10 s. Therefore, at long time, a bacterium appears to perform a sort of random walk. With a typical size of a bacterium, ℓ, of the

order of microns, a typical speed, v, of the order of 10 μm/s, and a density ρ comparable to that of water (1000 kg/m^3), the Reynolds number (Re = $\rho v \ell/\eta$) is much less than 1.

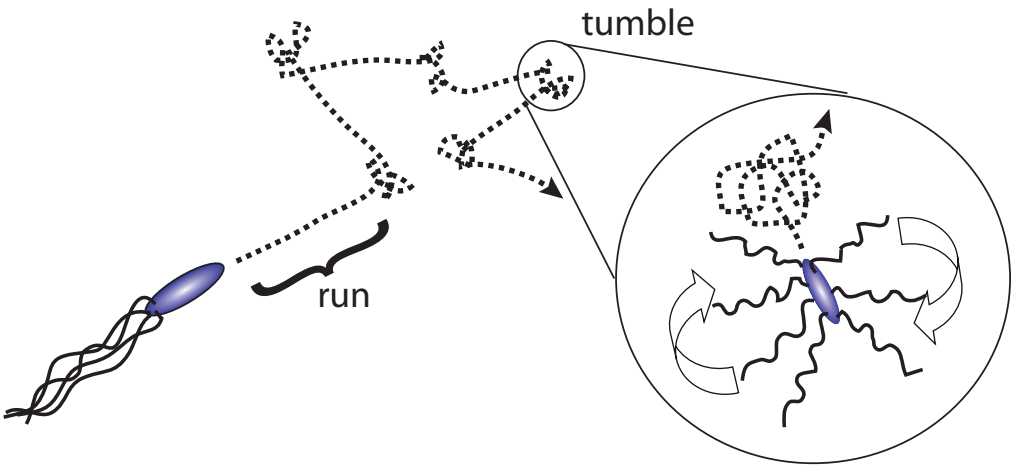

Figure 5.1: Illustration of running and tumbling motions of bacterium like *E. coli*.

Early experimental studies utilizing light-scattering techniques demonstrated that the velocity distribution of motile microorganisms, in general, and bacteria, in particular, is not Maxwellian [13], indicating that their motion is far more complex than that of Brownian particles [78]. A key question is: what is the large-scale flow behavior of a collection of swimming microorganisms? Experiments on dense suspensions in a variety of different geometries including soap films [95, 118], sessile drops [106], and semi-solid agar substrates [121] point to a consensus that collective motion in the form of jets and swirls is a generic feature of active swimmer suspensions at sufficiently high densities. Thus, active swimmer suspensions, despite being at low Reynolds number, are a breeding ground for "exotic" fluid phenomena more commonly associated with systems at higher Reynolds number. This richness is due in large part to the fact that they are internally driven to a non-equilibrium regime wherein the usual, familiar balance of energy scales

is disrupted. Moreover, even a minimal model of interacting swimmers must reckon with nonlinear couplings of orientational order, concentration fluctuations, and long-range hydrodynamic interactions. One class of models, termed active hydrodynamics [44, 94], describes the collective motion of active suspensions by constructing hydrodynamic equations augmented with dynamical equations accounting for orientational and concentration couplings. This phenomenological framework leads to many interesting predictions for the behavior of active suspensions, including instabilities [94], giant density fluctuations [17, 76], and novel rheological effects [44]. One of the most dramatic predictions of Ref. [44] is viscosity enhancement or reduction by activity. This effect can be qualitatively and simply understood by considering the detailed nature of the force that an active swimmer exerts on the fluid.

Swimmers that propel themselves through a fluid can be broadly classified as either "pushers," which propel themselves using rear-mounted flagella like the bacterium *E. coli* in a "run" state, or "pullers," like the algae *Chlamydamonas reinhardtii* which use front-mounted flagella the way a human swimmer uses her/his arms. These two types of organisms exert different forces on the surrounding fluid. Pushers force fluid back behind them with their propellers and also push it forward with their bodies as they move, so that the fluid is brought in at the sides and moves away at the front and back. Pullers pull fluid towards them with their flagella and drag it along with them from behind, so that fluid flows in at the front and back and away at the sides. These two types of swimmers, along with the fluid flows they excite, are illustrated in Figure 5.2.

This flow pattern can affect the large-scale flow of a fluid provided the suspension contains enough of these swimmers and provided the swimmers are rod-shaped. Imagine that the fluid

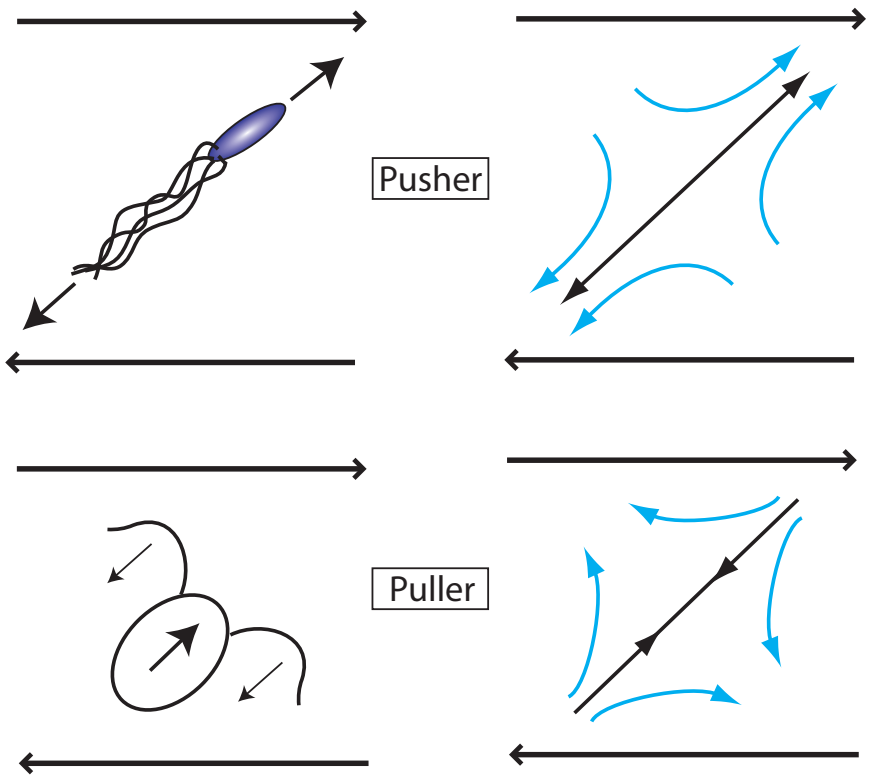

Figure 5.2: Types of swimmers and the fluid flow fields (blue arrows) they generate in an imposed shear flow. Pusher type swimmers like *E. coli* (top) enhance the imposed shear flow. Puller type swimmers like *Chlamydamonas* (bottom) fight back against the imposed shear flow.

above the rod is moving to the right, while the fluid below is moving to the left. This is the prototypical situation in shear flow, either imposed externally or generated by collective motion of nearby swimmers. According to standard theory, in this flow, a rod (even a passive, non-living rod) tends to align at a fixed angle, tilted to the right of vertical. In this orientation, a pusher rod increases the flow velocities above and below, enhancing the shear flow. This enhancement further increases the orientation of the swimmers, thus implying instability with respect to shear perturbations of the homogeneous isotropic state. A puller reduces the imposed flow velocities since the flows it produces by swimming tend to cancel out the imposed shear flow. Viscosity is a measure of the ease with which the fluid moves in such a shear flow in response to applied shear

forces. So a rod-shaped pusher ought to decrease overall fluid viscosity, whereas a rod-shaped puller ought to decrease it.

These dramatic effects on viscosity have been recently observed experimentally for high concentrations ($\phi > .05$) of pushers [95] and pullers [84]. While interesting and relevant to the work described in this thesis on the whole, the work described in this chapter instead focuses on the effects of non-thermal noise in dilute ($\phi < .01$) swimmer suspensions with the aim of advancing a detailed understanding of fluctuations in swimmer suspensions. One of the primary motivations of our work is to advance the development of a phenomenological framework for fluctuating active hydrodynamics [58]. This theoretical work extends earlier active hydrodynamic theories [44] by accounting for previously unconsidered effects of noise terms and concentration fluctuations in the equations governing the dynamics of the bacterial bath. One notable prediction of the theory of Ref. [58] is the scaling of the power spectrum $\Delta(\omega) \sim \phi/\sqrt{\omega}$ observed in microrheology measurements on wild-type bacteria arises only when concentration fluctuations are considered. Active hydrodynamic theories that do not include concentration fluctuations [44] do not predict the observed scaling. Another notable result is that the superdiffusive MSDs observed for both wild-type and tumbler bacterial baths arises naturally from the fluctuating active hydrodynamic theory. Existing theories of active media [94] predict long-time tails and anomalous corrections to diffusion but not superdiffusion.

5.3 Materials and Sample Preparation

We used two strains of *E. coli*, a rod-shaped bacterium with dimensions $3 \times 1\,\mu$m, in our studies: RP437, the "wild-type", which runs and tumbles [80] and RP1616, the "tumbler", which

predominantly tumbles [3]. Overnight cultures in stationary phase were diluted 1/300 in Luria Broth (Difco) and grown aerobically at $25\,^{\circ}$C under 220 RPM shaking for 6 hrs. Subsequently, they were centrifuged for 10 minutes at 5000 RPM and resuspended to the desired concentration in a buffer comprised of 10 mM K_2HPO_4, 0.1 mM EDTA, and 0.2 wt % glucose (pH = 8.2), which was added to maintain vigorous bacterial motility under the anaerobic conditions of our sample chambers [1]. We determined the concentration of *E. coli* in our experiments by direct counting under a microscope. The bacterial suspension was diluted 1/200 in a pluronic surfactant F127 (BASF). The pluronic has the useful property that it is solid at room temperature and liquid at $\approx\ 4^{\circ}$ C. This enabled us to immobilze the bacteria, facilitating counting. The diluted bacterial suspension was mixed into the pluronic in a freezer at 4° C, loaded into a microscope slide, and then counted under a microscope at room temperature. Typically, 5 randomly selected subvolumes of the sample were counted and averaged for each run to determine the concentration.

We added a small amount ($\phi_s = 10^{-4}$) of fluorescently labeled polystyrene spheres (Duke Scientific) of diameter $2a = 2 - 10\,\mu m$ to the bacterial suspension, and to density match them, we added 15 wt % sucrose to the solution. To prevent bacterial adhesion, we prepared the chambers from BSA coated glass slides and coverslips. We used parafilm spacers to bring the thickness of the chambers to $\approx 240\,\mu$m. Images were recorded via quasi-2D image slices from the middle of the 3D chamber. Samples were loaded into the chamber and sealed with optical glue just prior to each run.

5.4 Results and Discussion

We quantified the fluctuations in the bacterial bath by computing MSDs from the motions of embedded micron-sized tracers [26]. The one-point displacement (MSD1) is defined by $\langle \Delta r_x^2(\Delta t) \rangle = \langle \Delta r_x(t, \Delta t) \Delta r_x(t, \Delta t) \rangle$, where $\Delta r_x(t, \Delta t) = r_x(t + \Delta t) - r_x(t)$ is the particle displacement in the x-direction during lag time Δt. The *two-point* displacement (MSD2) is defined as $\langle \Delta \mathbf{r}^2(\Delta t) \rangle_2 = (2R/a)\, D_{rr}(R, \Delta t)$, where $D_{rr}(R, \Delta t)$ is the longitudinal component of $D_{ij}(R, \Delta t) = \langle \Delta r_i^{(1)}(t, \Delta t) \Delta r_j^{(2)}(t, \Delta t) \rangle$, which measures correlations of two distinct particles $(1, 2)$ with an initial separation $\mathbf{R}$. Over the time scale of our experiments, $\mathbf{R}$ lies in the focus plane of our microscope and its magnitude $R \equiv |\mathbf{R}|$ is greater than that of individual particles' displacements. The main advantage of two-point microrheology is that it provides a more reliable measure of length scale dependent fluctuations in media where the length scale of heterogeneities and tracer boundary conditions are not *a priori* known [26, 57]. Indeed, since $D_{ij}(R, \Delta t)$ is ensemble averaged over tracer pairs with $R \gg a$, it reflects the dynamics of the medium on larger length scales than the tracer size, permitting quantitative measurements even in the presence of heterogeneities. In general, MSD2 will equal MSD1 if heterogeneities in the medium have length scales smaller than the tracer size, otherwise they will differ in both magnitude and functional form.

Typical MSD data are presented in Figure 5.3, which shows that the one-point MSD in both bacterial strains displays a crossover from superdiffusive behavior at short lag times ($\langle \Delta r^2 \rangle_1 \sim \Delta t^\alpha, 1 < \alpha < 1.5$) to diffusive behavior ($\alpha = 1$) at long lag times. The diffusivity of identical particles in water is constant and about an order of magnitude lower than the bacterial bath at long times. These observations are similar to that of Ref. [118] in which one-point measurements

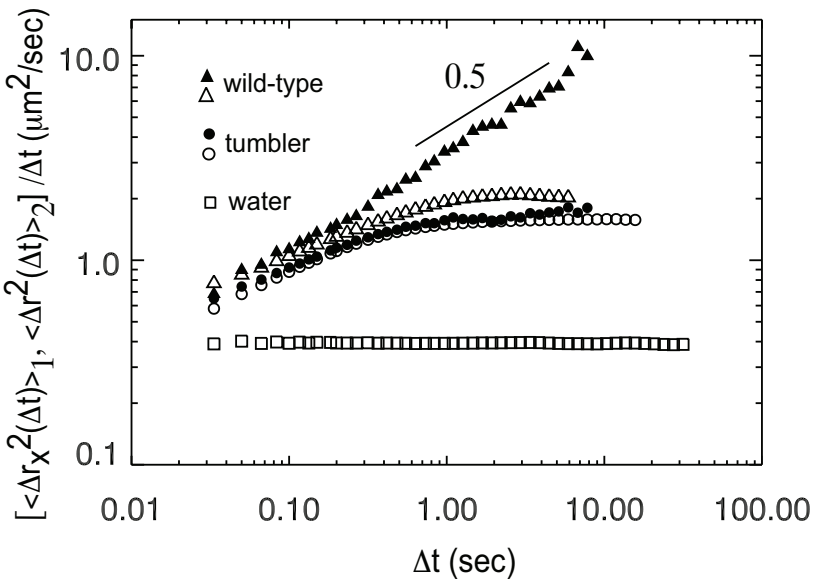

Figure 5.3: MSD for particles in bacterial baths. 1-pt (open symbols) and 2-pt (closed symbols) mean square displacements divided by the lag time, Δt, for 2a = 2 μm particles in bath of wild-type RP437 (triangles) and tumbler RP1616 (circles) bacteria at ϕ = .003. MSD1 for 2a = 2 μm particles in water (squares) is a flat line in this rescaled plot.

were made of bacterial baths in soap films. However, our two-point data for the wild-type, by contrast, exhibit a nearly power-law superdiffusion ($\langle \Delta r^2 \rangle_2 \sim \Delta t^{1.5}$) over 2.5 decades of observation time. We also verified that $D_{rr}(R, \Delta t) \sim 1/R$ [see Figure 5.4] for both wild-type and tumbler baths, indicating that the bacterial bath, though an active medium, can be treated on the separation scale R as a coarse-grained continuum whose properties can be probed with two-point microrheology [26, 57]. Theoretical predictions [58] and simulations [107] have corroborated that equal-time correlation functions of an active swimmer suspension's velocity field on intermediate length scales should decay as 1/R, at least above an orientational decay length, ξ_U, accounting for orientational alignment of the rod-shaped bacteria. ξ_U is further discussed in Section 5.5. That MSDs exhibit superdiffusion is suggestive of but not a proof of the breakdown of the FDT, which requires an independent measurement of the rheological

response function.

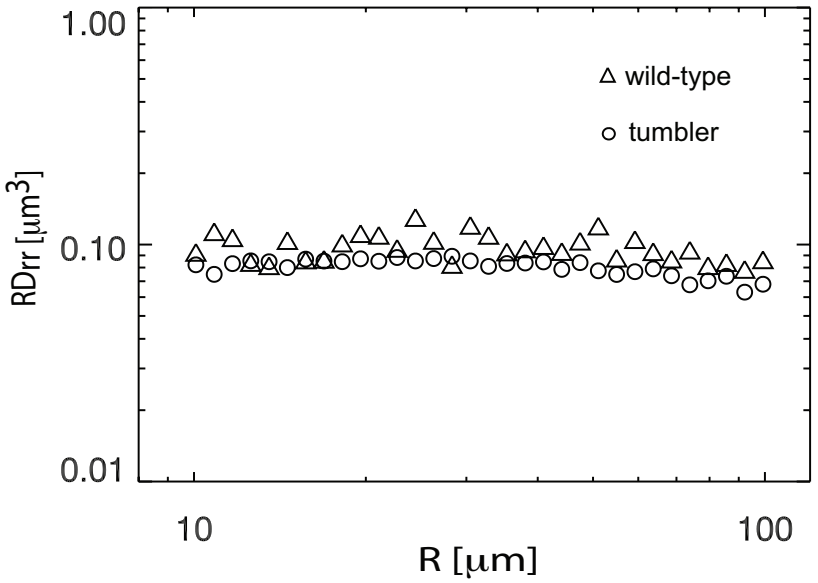

Figure 5.4: Rescaled two-point correlation $RD_{rr}(R, \Delta t = .067\,\text{sec})$ vs R for wild-type (triangles) and tumbler (circles) bacterial baths both at a volume fraction $\phi = .003$. The data demonstrates $D_{rr} \sim 1/R$ for $R \geq 10\,\mu$m, and implies orientational decay length $\xi_U \leq 10\,\mu m$.

Response measurements were performed using the oscillating optical tweezer setup of Figure 3.14 in Section 3.4.1. Briefly, an optical trap with typical trap stiffness of $\sim 1 \times 10^{-3}$ pN/nm was formed by focusing an ~ 100 mW laser beam ($\lambda = 1054\,$nm) through a 1.3 NA oil immersion objective (Zeiss). The trapping beam position was sinusoidally scanned using a galvanometer-drvien mirror at frequencies from 0.5 to 500 Hz. A $2a = 4.0\,\mu$m PS sphere was trapped $\sim 6\,\mu$m from the coverslip. The position of the tracer was detected using forward scattered light from a co-linearly aligned HeNe laser beam focused onto a split photodiode (Hamamatsu S4204). The photodiode signal was fed into a lock-in amplifier (Stanford Research Systems 530) along with the reference from the driving function generator signal. The displacement and phase of the trapped particle output by the lock-in amplifier were logged into a PC running LabView (National Instruments).

The equation of motion for a particle of radius a trapped in an oscillating harmonic potential may be written as: $6\pi\eta a\dot{x} = -k\,[x - A\cos(\omega t)]$, where η is the viscosity of the medium, k is the stiffness of the trap, and A is the driving amplitude. Its steady state solution yields the normalized displacement of the sphere in the trap: $d(\omega) = \left\{1 + [\,6\pi a\eta(\omega)\omega/k\,]^2\right\}^{-1/2}$. For a more detailed discussion see Section 3.4.1.

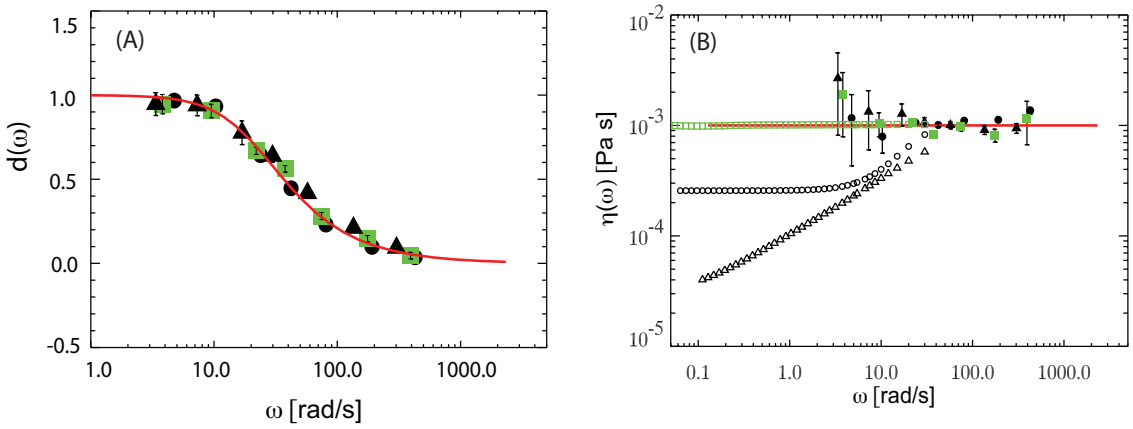

Figure 5.5: (A) Normalized Displacement of a 4.0 μm diameter sphere in the optical trap as a function of driving frequency for wild-type (triangles), tumbler (circles), and water (squares). Line is a fit to $d(\omega)$ (see text). (B) Frequency dependent viscosity derived from oscillating trap measurements for 4.0 μm diameter sphere in water (solid squares), the tumbler (solid circles), and the wild-type (solid triangles) bath at ϕ = .003. Viscosities $\eta_2(\omega)$ derived from the averaged two-point measurements using the generalized Stokes-Einstein relation are plotted for the tumbler (open circles), the wild-type (open triangles), and a bead in water (open squares).

Figure 5.5A shows the raw normalized displacement data for a particle in water and in active bacterial baths of tumblers and wild-types. The solid line is a fit to $d(\omega)$ with $\eta = 0.001\,\text{Pa}\cdot\text{s}$, trap stiffness $k = 8\times10^{-4}\,\text{pN/nm}$, and radius $a = 2.0\,\mu\text{m}$. The experimental data agree with each other and with the theoretical curve. From them, we extract the viscosity $\eta(\omega)$ shown in Figure 5.5B. Clearly, the presence of actively swimming bacteria at volume fraction 10^{-3} does not modify the viscosity of the medium significantly from that of water, $\eta(\omega) = \eta_0 = 0.001\,\text{Pa}\cdot\text{s}$.

While recent theories of pusher type active swimmers predict novel reduction in the viscosity [44], our experiments are well below the concentration at which these effects are observable. Instead, our results are consistent with the Einstein result for hard spheres: $\eta = \eta_0(1 + \frac{5}{2}\phi)$, namely, a negligible modification in the viscosity for $\phi \sim 10^{-3}$. Moreover, assuming for the moment the generalized Stokes-Einstein relation, we can extract the (FDT consistent) response from the collapsed two-point displacement (MSD2) [57]: $\eta_2(\omega) = k_B T/3\pi\omega^2 a\langle\Delta r^2(\omega)\rangle_2$, as shown in Figure 5.5. The difference between $\eta(\omega)$ and $\eta_2(\omega)$ explicitly indicates a strong violation of FDT. We can moreover conclude that the superdiffusion in the MSDs is due purely to noise and not a novel viscosity enhancement as predicted by Ref. [44] and qualitatively considered in Section 5.2. The apparent importance of noise even at dilute densities of swimmers motivated Lau and Lubensky [58] to augment the equations of active hydrodynamics with noise terms, discussed in detail in Section 5.5.

Next, to access the heterogeneity of the bacterial bath, we explored the length-scale dependence of fluctuations by systematically varying the size of the tracers at a fixed bacterial concentration. Figure 5.6A shows MSDs obtained for spheres in the tumbler bath. All samples and all tracer sizes exhibit a crossover from superdiffusion to diffusion on similar timescales, with an enhanced diffusion coefficient $D = \gamma D_T$, where $\gamma = 4.3$ and $D_T = k_B T/(6\pi\eta_0 a)$ is the equilibrium coefficient. Moreover, MSD1 and MSD2 are nearly equal in magnitude and functional form, suggesting that the activity in the tumbler bath is homogeneous. Rescaling time by the crossover time τ and the MSDs by $2D_T\Delta t$ collapses all the data onto a master curve: $[\langle\Delta r_x^2(\Delta t)\rangle_1, \langle\Delta r^2(\Delta t)\rangle_2]/(2D_T\Delta t) = \gamma + (\,1-\gamma\,)(\,1-e^{-x}\,)/x$, where $x = \Delta t/\tau$. Figure 5.6B shows the collapsed MSD data along with the master curve with $\tau = 0.1\,\mathrm{s}$.

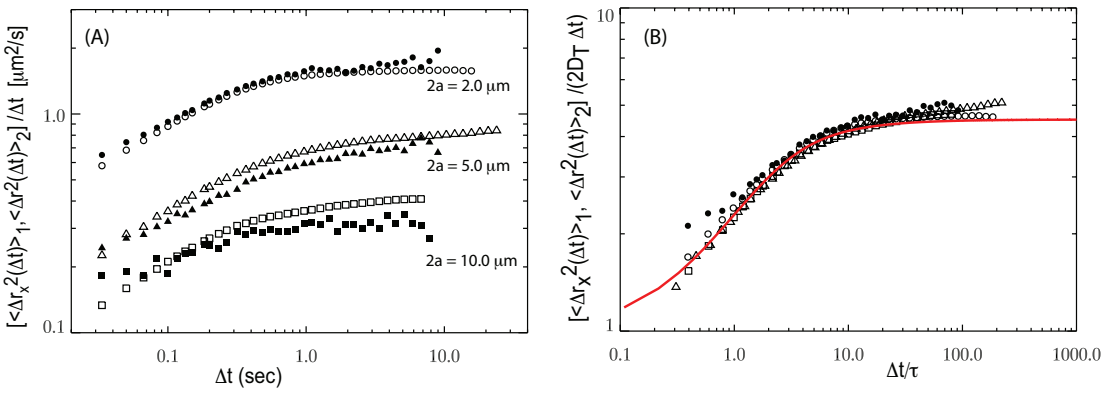

Figure 5.6: (A) Raw 1-pt (open symbols) and 2-pt (closed symbols) MSDs for tumblers. Circles, triangles, and squares are for particle diameters $2a = 2.0, 5.0,$ and 10.0 μm, respectively. (B) Collapsed 1-pt (open symbols) and radius collapsed averaged 2-pt (closed symbols) MSDs for the tumblers at ϕ = .003. The solid line is the master curve: $\gamma + (1-\gamma)(1-e^{-x})/x$ (see text).

The functional form of the master curve can be derived from the generalized Langevin equation (GLE) in the overdamped limit with thermal and active noise terms: $\int_{-\infty}^{t} dt' \zeta(t-t')\mathbf{v}(t') = \mathbf{f}_T(t) + \mathbf{f}_A(t)$. Here $\zeta(t-t')$ is the probe resistance, $\mathbf{f}_T(t)$ is the thermal noise, and $\mathbf{f}_A(t)$ is the active noise due to the bacteria. The noise terms have the following properties: $\langle f_T(t)\rangle = 0$, $\langle f_A(t)\rangle = 0$, $\langle f_T(t) f_A(t)\rangle = 0$, $\langle f_T(t) f_T(t')\rangle = 2D_T\delta(t-t')$, $\langle f_A(t) f_A(t')\rangle = \frac{2D_A}{\tau} e^{-|t-t'|/\tau}$ where τ is a time scale characterizing bacterial activity [96, 118]. It follows that the MSD1 derived from the GLE has the following form [86, 118]:

$$\langle \Delta r_x^2(\Delta t)\rangle_1 = 2D_T\Delta t + 2D_A\tau\,[\Delta t/\tau - 1 + \exp(-\Delta t/\tau)], \tag{5.1}$$

which yields the tumbler master curve upon rescaling both sides of the equation by $1/2D_T\Delta t$ and substituting the variables $x = \Delta t/\tau$ and $\gamma = (D_A + D_T)/D_T$. We can draw two important conclusions from the fact that the one and two-point MSDs for the tumblers can be collapsed by such a functional form. The first is that the activity in the tumbler bath is well described by

a *single* timescale τ. The second is that the activity in the tumbler bath is homogeneous since the MSD2, averaged over large length scales ($10\,\mu m < R < 100\,\mu m$), is trivially related to the MSD1 via affine extrapolation (MSD1 = $(2R/a) * D_{rr}$), as in equilibrium homogeneous media.

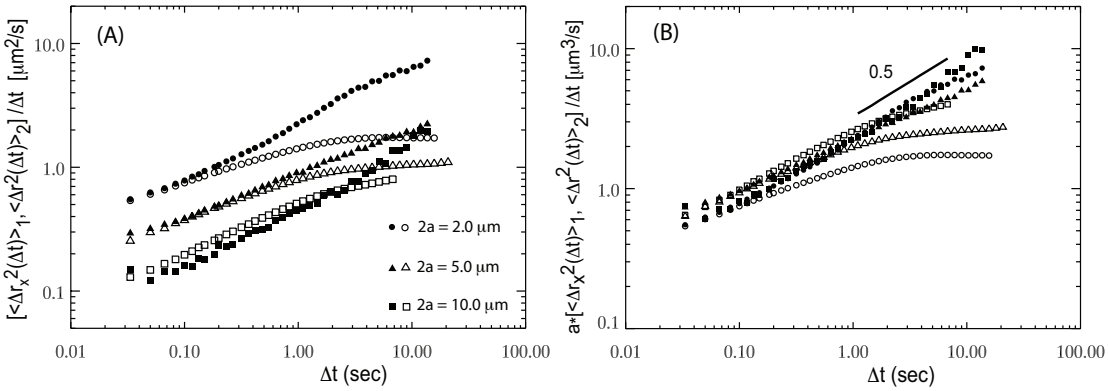

Figure 5.7: (A) Raw 1-pt (open symbols) and 2-pt (closed symbols) MSDs for wild-type bacteria. (B) Radius rescaled 1-pt(open symbols) and 2-pt (closed symbols) MSDs for the wild-types at ϕ = .003. Circles, triangles, and squares are for particle diameters $2a = 2.0, 5.0,$ and 10.0 μm, respectively.

The MSD behavior for the wild-type bacteria are strikingly different: the MSD1 exhibits a crossover dependent on tracer size, while all of the MSD2 exhibit superdiffusion with nearly the same exponent of 1.5 over 2.5 decades of time, independent of the tracer size, as shown in Figure 5.7A. Fits of the wild-type MSD1 to Eq. 5.1 were poor, suggesting that the activity in the wild-type bath cannot be described in terms of a single relaxation time τ. We found that the trivial rescaling $a\langle\Delta r^2(\Delta t)\rangle_2/\Delta t$ collapsed the respective MSD2 data [see Figure 5.7B]. Under this rescaling, however, (and other simple scaling functional forms as well) the wild-type MSD1 failed to collapse, signaling the presence of heterogeneity on the tracer length scale. The superdiffusive exponent of the MSD1 approaches that of the two-point data ($\alpha \sim 1.5$) as a increases. This suggests that one-point measurements are intrinsically ambiguous: the activity inferred depends on the tracer size and boundary conditions [18, 57]. Two-point measurements,

in contrast, provide a more robust characterization of the long-wavelength fluctuations of the medium than one-point measurements.

We employ a recently developed phenomenological theoretical framework for an active medium to interpret the experimental MSD data [57, 58]. The bacterial activity gives rise to non-thermal stress fluctuations whose power spectrum $\Delta(\omega)$ can unambiguously be extracted from *two-point* microrheology data via

$$D_{rr}(R,\omega) = \frac{\Delta(\omega)}{6\pi\omega^2\, R\,|\,\eta^*(\omega)|^2}. \tag{5.2}$$

The power spectrum $\Delta(\omega)$ can be interpreted as a frequency-dependent effective temperature which quantifies the departure from equilibrium. For thermal systems in equilibrium, the FDT relates the noise power spectrum to the viscosity of the medium, resulting in $\Delta(\omega) = \Delta_T$ where $\Delta_T \equiv 2k_BTRe[\eta^*(\omega)]$.

Our results are exhibited in Figure 5.8A. For water, we find that the power spectrum is flat. This is expected since particles diffusing in water are in equilibrium and viscosity is a constant, i.e., $\eta(\omega) = \eta_0$ implying $\Delta_T = 2\eta_0 k_B T$. This can be explicitly shown as well since the MSD2 is linear in Δt, implying $D_{rr}(R,\Delta t) \sim \Delta t$ for purely diffusive systems, resulting in a frequency dependence after Fourier transformation given by $D_{rr}(R,\omega) \sim \omega^{-2}$. The frequency dependence thus cancels out in Eq. 5.2. For the tumblers, both MSD1 and MSD2 have functional forms described by Eq. 5.1, resulting in a $\Delta(\omega)$ that is a constant plus a Lorentzian, flat at low frequencies with a knee at higher frequencies. The Lorentzian is the Fourier transform of the exponential term in Eq. 5.1 and originates from the exponentially correlated active noise term in the GLE. For wild-types, the MSD2 $\sim \Delta t^{1.5}$ implying that $\Delta(\omega)$ also exhibits power-law

behavior, $\Delta(\omega) \sim \omega^{-0.5}$, over 2.5 decades. In both tumbler and wild-type cases $\Delta(\omega) > \Delta_T$, with a greater deviation occuring at low frequencies. For the wild-type, the prefactor Δ_0 of $\Delta(\omega) = \Delta_0/\sqrt{\omega}$ rises linearly with the bacterial concentration, as shown in Figure 5.8B. In the following section, we discuss the microscopic origins of the scaling observed for $\Delta(\omega)$ using a fluctuating active hydrodynamic theory developed to understand microrheology in active swimmer suspensions.

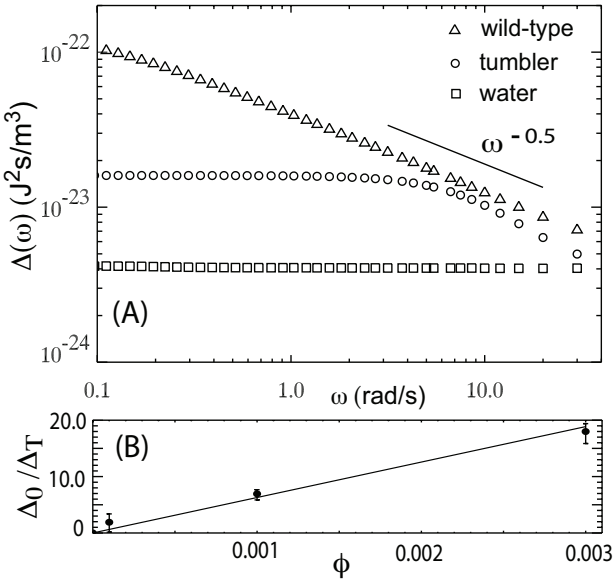

Figure 5.8: (A) The spectrum $\Delta(\omega)$ of active stress fluctuations obtained from two-point microrheology and active response measurements. The triangles are the wild-types, circles are the tumblers (both $\phi = .003$), squares are water ($\phi = 0$). (B) Linear dependence of the prefactor Δ_0 in $\Delta(\omega)$ on the volume fraction ϕ of the wild-type bacteria; $\Delta_T \equiv 2\eta_0 k_B T$.

5.5 Theory of Fluctuating Active Hydrodynamics

An active medium comprised of rod-like swimming organisms can be modeled by constructing dynamical equations which couple concentration and orientational dynamics of the swimmers with a Navier-Stokes equation for the velocity field, **v**, of the suspension. Essentially, the equations stem from the key assumption that the active bacterial bath can be modeled via a two-fluid description wherein one component is a thermal fluid (solvent) while the other is an active fluid comprised of force dipoles with nematic order (bacteria). Additionally, we include noise terms in the equations and consider density fluctuations of the bacteria, which were not considered in Ref. [44]. These additional terms were necessary to account for our observations in the tumbler and wild-type bacterial bath measurements. The reader is referred to Ref. [58] for the full details of how the equations are built up from "first-principles". In order to give the reader a bird's-eye view of the structure of the theory, we begin, *in medias res*, by writing down the linearized governing equations used to account for our observations:

Momentum of fluid
$$\rho\partial_t v_i = \underbrace{\eta\nabla^2 v_i}_{\substack{viscous\\stress}} - \underbrace{\partial_i p}_{pressure} + \underbrace{\partial_j \sigma^T_{ij}}_{\substack{thermal\\stress}} + \underbrace{\partial_j \sigma^A_{ij}}_{\substack{active\\stress}} \tag{5.3}$$

Orientational dynamics
$$\partial_t \underbrace{Q_{ij}}_{\substack{force\\dipole\\density}} = -\underbrace{\tau_Q^{-1}}_{\substack{relaxation\\time}}(1 - \underbrace{\xi_Q^2}_{\substack{correlation\\length}}\nabla^2)Q_{ij} + \underbrace{s_{ij}}_{\substack{random\\noise}} \tag{5.4}$$

Concentration dynamics
$$\partial_t \delta c = \underbrace{D\nabla^2\delta c}_{\substack{diffusion\\term}} + \underbrace{\alpha c\partial_i\partial_j Q_{ij}}_{\substack{active\\current}} + \nabla\cdot\underbrace{\delta\mathbf{J}}_{\substack{random\\current}} \tag{5.5}$$

Eq. 5.3 is essentially the linearized Navier-Stokes equation accounting for momentum balance with two additional noise terms, one due to thermal and one due to active noise. In principle, there is another term in Eq. 5.3 that is required to account for the torque that a velocity gradient exerts on the nematic order parameter, as expected for liquid crystalline systems in the isotropic phase. However, we have set that term to zero, since it predicts a very strong viscosity renormalization, whereas our results indicate that the viscosity of the bacterial bath is indistinguishable that of water [Figure 5.5]. In the process of tumbling or swimming, the bacteria generates an active force density $f_A(\mathbf{x},t) = -\nabla \cdot \sigma^A$ which contributes the active stress term in Eq. 5.3. The active stress tensor, σ^A_{ij}, is

$$\sigma^A_{ij} = W c(\mathbf{x},t) Q_{ij}(\mathbf{x},t), \tag{5.6}$$

where $c(\mathbf{x},t)$ is the concentration of the bacteria, Q_{ij} is a traceless, symmetric force-dipole density whose dynamics in given by Eq. 5.4, and W is strength of the force dipole characterizing the swimmer, positive for pushers and negative for pullers [see Figure 5.2].

When this form of the active stress tensor is considered, it is clear that Eqns. 5.3-5.5 are coupled, i.e., each equation contains at least one parameter contained in the others. The form of the active stress term in Eq. 5.6 was first considered by Hatwalne and Ramaswamy [44]. In their active stress term, however, the concentration was assumed to be constant, i.e., $c(\mathbf{x},t) = c_0$. In Lau and Lubensky [58], the concentration is decomposed into a constant and a fluctuating part: $c(\mathbf{x},t) = c_0 + \delta c(\mathbf{x},t)$ which leads to a full active stress $\sigma^A_{ij}(\mathbf{x},t) = W c_0 Q_{ij}(\mathbf{x},t) + W \delta c(\mathbf{x},t) Q_{ij}(\mathbf{x},t)$ with the consequence that active stress fluctuations become $\langle\, \delta\sigma^A_{ij}(\mathbf{q},\omega)\delta\sigma^A_{kl}(-\mathbf{q},-\omega)\,\rangle / W^2$ =

$c_0^2\langle Q_{ij}(\mathbf{q},\omega)Q_{kl}(-\mathbf{q},-\omega)\rangle + \langle\, \delta c(\mathbf{q},\omega)\delta c(-\mathbf{q},-\omega)\,\rangle\langle Q_{ij}(\mathbf{q},\omega)Q_{kl}(-\mathbf{q},-\omega)\rangle +$

$\langle\, \delta c(\mathbf{q},\omega)Q_{kl}(-\mathbf{q},-\omega)\,\rangle\langle Q_{ij}(\mathbf{q},\omega)\delta c(-\mathbf{q},-\omega)\,\rangle$ after Gaussian decoupling. Active processes enhance stress fluctuations, and assuming long-range isotropy, the active stress fluctuations can be expressed as $\langle\, \delta\sigma_{ij}^A(\mathbf{q},\omega)\delta\sigma_{kl}^A(-\mathbf{q},-\omega)\,\rangle = \Delta_A(q,\omega)\left[\delta_{ik}\delta_{jl} + \delta_{il}\delta_{jk} - \frac{2}{3}\,\delta_{ij}\delta_{kl}\right]$ for both tumblers and wild-types. The power spectrum in Eq. 5.2 is related to $\Delta_A(q,\omega)$ by $\Delta(\omega) = \Delta_A(\mathbf{q}=0,\omega)$, i.e., in the long wavelength limit. The long-wavelength limit is probed by two-point measurements, but not by one-point measurements. For the tumblers, the power spectrum is nearly Lorentzian with $\Delta(\omega) = \Delta_T + W^2c_0^2\tau^2(k_BT/\gamma)/[1+(\omega\tau)^2]$, where $\Delta_T \equiv 2\eta_0 k_BT$ is the thermal contribution. The non-thermal term comes from ignoring the concentration fluctuations and considering only the $c(\mathbf{x},t) = c_0$ contribution to $\Delta_A(q=0,\omega)$. While this assumption seems reasonable for tumblers since they do not move around much, it seems unreasonable for wild-types. Since the wild-types are swimming around, it is conceivable that their density fluctuates in space and time. Consideration of the $c(\mathbf{x},t) = \delta c(\mathbf{x},t)$ contribution to $\Delta_A(q=0,\omega)$ leads to $\Delta(\omega) \sim \phi/\sqrt{\omega}$ observed in two-point measurements in the wild-type bath [Figure 5.8].

Next, we turn to discussion of orientational dynamics of the bacterial governed by Eq. 5.4. Active swimmers have no monopole moment because mutual forces of swimmer and fluid cancel by Newton's third law. The minimal description of an active swimmer is thus a permanent force dipole. In wild types and tumblers, forces are directed, respectively, along and perpendicular to the long-bacterial axes, as illustrated in Figure 5.9. Thus, in wild-types, Q_{ij} is equal to the uniaxial nematic order parameter Q_{ij}^U whereas in tumblers, it is equal to a biaxial order parameter Q_{ij}^B. The equation governing the dynamics of Q_{ij} is assumed to be the same as for equilibrium

nematics in the isotropic phase [58]. To allow for the possibility of two order parameters Eq. 5.4 becomes

$$\partial_t Q_{ij}^A = -\tau_A^{-1}\left(1 - \xi_A^2 \nabla^2\right) Q_{ij}^A + s_{ij}, \tag{5.7}$$

where A = (U, B) denoting either uniaxial or biaxial quantities. τ_A is the relaxation time, ξ_A the correlation length of Q_{ij}^A, and s_{ij} is a spatial-temporal white noise with zero mean. Although both wild-type and tumbler bacteria obey Eq. 5.7, the detailed forms of Q_{ij}^U and Q_{ij}^B are quite different [58]. Importantly, interactions among bacteria favor long-range order in Q_{ij}^U but not in Q_{ij}^B, implying that $\tau_B \ll \tau_U$ and $\xi_B \ll \xi_U$. This fact is crucial to the explanation for the difference in the behavior of the MSDs between the tumbler and wild-type bacteria shown in Figures 5.6 and 5.7. Notably, the wild-type bacterial bath exhibits a length scale dependence, possibly in the form of jets and swirls, that leads to a tracer size-dependent MSD1 and to MSD2 $\neq$ MSD1. For the tumblers, by contrast, MSD2 = MSD1 for all tracer sizes, implying that $\xi_B < 2\,\mu m$, the diameter of the smallest tracer in our studies. Thus the physical picture of the tumbler bath is that of a fluid homogeneously stirred at small scales by a random force with a characteristic relaxation time $\tau_B \approx 0.1$ seconds. For the wild-type bath, $\tau_U > 10$ seconds since the MSD2 is superdiffusive up until that time [Figure 5.7B]. Furthermore, our measurement of $D_{rr} \sim 1/R$ for $R > 10\,\mu m$ in Figure 5.4 constrains $\xi_{B,U} < 10\,\mu m$.

Eq. 5.5 is an advection-diffusion equation with an active advection term and an additional noise current term (δJ) describing concentration dynamics of the bacteria . For both wild-types and tumblers, the concentration of bacteria obeys the continuity equation: $\partial_t \delta c = -\nabla \cdot \mathbf{J}$ with $J_i = -D\partial_i \delta c - \alpha c_0 \partial_j Q_{ij}^A + \delta J_i$, where c_0 is the average concentration, D is the diffusion

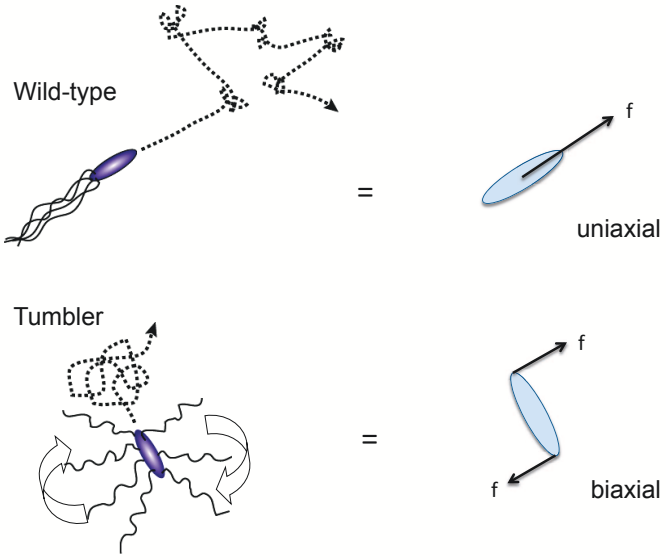

Figure 5.9: Cartoon of wild-type and tumbler bacteria swimming motions. For wild-type bacteria, motion is primarily translational, directed along its long-axis. Thus the active dipolar stress it exerts on the medium is described by a uniaxial order parameter Q^U_{ij}. For tumblers, the motion is primarily rotational, resulting from flagellar forces oriented perpendicular to its long axis. The resulting active stress is described by a biaxial order parameter Q^B_{ij}.

constant, δJ_i is a random current, and the second term stems from the nonequilibrium driving of mass flow [104, 105].

The use of nematic order to model the bacteria, rather than polar order, as might be expected for swimmers that move unidirectionally, is somewhat controversial. Both polar [5] and nematic [44, 94] order have been employed in the literature to model self-propelled organisms. A recent simulation [89] provides evidence that instabilities occuring in self-propelled rods are consistent with both polar and nematic fluctuations. Theoretical studies of active gels [64] also suggest the possibility that there is a region of phase space wherein a system of active polar particles has a

preference for nematic rather than polar order. Ultimately, assuming incipient polar instead of nematic order in our model leads, *inter alia*, to a power spectrum which scales as $\Delta(\omega) \sim \omega^{-3/2}$, in clear disagreement with the $\Delta(\omega) \sim \omega^{-1/2}$ observed in our experiments and obtained with the nematic order in our model.

5.6 Conclusion

Using a combination of passive one- and two-point microrheology and active response measurements, we have observed a number of striking effects in dilute bacterial baths including: (i) superdiffusive scaling of the MSDs that depends on swimming behavior in a length scale dependent manner, (ii) Active stress power spectrum $\Delta(\omega) \sim \phi/\sqrt{\omega}$ for wild-type bacteria and Lorentzian for tumblers, and (iii) breakdown of the FDT resulting from enhanced noise due to activity rather than viscosity enhancement. Importantly, (i) and (ii) suggest that two-point measurements are essential to robustly extract the fluctuations in bacterial baths, surmounting length scale heterogeneities as in equilibrium systems.

A theoretical framework of fluctuating active hydrodynamics coupling concentration fluctuations and orientational dynamics of liquid crystalline systems with hydrodynamic equations was developed and used to explain microrheological measurements in bacterial baths. Although viscosity renormalization is predicted in our theory as well as previous theories, our suspensions were too dilute to observe these effects. Attempts to increase density were hindered by unvigorous motility due to the anaerobic environment of our sample chamber. Potentially, future work reiterating these measurements in soap films, where vigorous aerobic motility and higher densities can be achieved, will observe viscosity enhancement effects.

Chapter 6

Rheology of Carbon Nanotube Networks During Gelation

6.1 Introduction

Filamentous networks play a crucial role in many biological and materials contexts. In living cells, for example, networks of biopolymers facilitate processes such as cell division and motility. Understanding the macroscopic mechanical properties of such networks, even *in vitro*, is challenging because of a complex interplay between the flexural rigidity of constituent filaments and inter-filament interactions such as crosslinking. To date, the most intensively studied model systems are semiflexible filament networks, such as those comprised of F-actin wherein entropic stretching of individual filaments dominates network linear and non-linear viscoelasticity [38, 102]. Rigid rod networks, by contrast, are relatively unexplored and should differ from

their semiflexible counterparts as a result of enthalpic effects associated with bending, compression, and inter-filament bonding. Carbon nanotube networks present opportunities to explore these latter issues. In addition, interest in carbon nanotube networks has grown as a result of their technological potential in composite materials [39, 50, 74]. These applications often depend on network connectivity, thus corroborating the need for a better understanding of network formation in this system class.

In this chapter, we describe work wherein we employ a combination of rheological measurements, analytic theory, and computer simulation to investigate network formation in aqueous dispersions of single wall carbon nanotubes (SWNTs). On the experimental side, an aqueous dispersion of SWNTs in surfactant is prepared, and, over time, the SWNTs crosslink due to strong localized van der Waals interactions at contact [47]. As the dispersion ages, clusters of bonded SWNTs form and eventually percolate across the sample, driving its rheological response from that of a Newtonian fluid to a gel. Microrheological measurements were made on this system at various time points along the sol-gel transition. Observation of time-resolved 'rigidity percolation' in this system of fixed SWNT volume fraction suggests inter-tube bonding as the dominant contributor to the elasticity. We demonstrate experimentally that the rheology of SWNTs can be scaled onto a single time-cure superposition master curve, consistent with other gelling systems [55].

The time-resolved experiments are closely related to the rheometry of fully cured SWNT gels at varying rod volume fractions ϕ [47]. The latter work found that the low-frequency elastic modulus (G') exhibited rigidity percolation above a critical volume fraction ϕ^* with power law form, i.e., $G'(\phi) \sim [(\phi - \phi^*)/\phi^*]^{2.3}$. In this Chapter we introduce a microscopic model to

understand this behavior. The model accounts for the number of inter-tube contacts in a static randomly oriented rod network as a function of rod volume fraction, length, and diameter; it is based on the crossing probability of rods in finite volumes. An assumption about the relative contributions to the shear modulus of bonds of varying degrees of connectivity permits derivation of an analytic expression for the scaling of shear modulus with rod volume fraction.

Finally, we extend the static model to account for time-resolved sol-gel dynamics. By incorporating bonding kinetics into the static model, we predict the variation of bonding between rods as a function of gelation time t. The new model provides a marked improvement over empirical power law forms that can be and often are used to describe the data. In contrast to previous simulations [31,37,116] and rheological measurements [46,47,63] of rigid rod networks, ours is the first study to directly relate the *measured* elasticity of a rigid rod system to its bond connectivity. Importantly, the work provides predictions about the connectivity of rigid rod networks, and potentially, a means for tailoring the mechanical, electrical, and thermal properties in materials comprised of rigid rod networks.

6.2 Experimental Section

6.2.1 Materials

Primary experiments were conducted on dispersions of SWNTs made by the HiPCO process (Carbon Nanotechnologies Inc.) at volume fraction ϕ = 0.0027. The nanotubes were purified and suspended in filtered deionized water (Millipore) with NaDDBS surfactant (Sigma Aldrich) following the protocol outlined in Ref. [52]. Further details of SWNT processing procedures can

be found in Ref. [14]. The ratio of SWNT to NaDDBS was 1:10 by weight. We prepared the dispersion by mechanical agitation for 6 hrs in a high-frequency bath sonicator (Cole-Palmer model 08849-00). A small amount ($\phi \sim .0001$) of fluorescently labeled carboxylated polystyrene spheres (Molecular Probes FluoSpheres) of nominal diameter, 2a = 0.46 μm, was added to the SWNT-NaDDBS dispersion. The samples were then loaded into a chamber and hermetically sealed with optical glue (Norland 63) just prior to each run.

6.2.2 Methods

Particle tracking microrheology [18, 69] was employed to follow the rheological evolution of the network. This method is well suited for measuring viscoelastic moduli of incipient gels, since they are generally fragile under shear and their moduli are often too weak to measure using conventional rheology. Formation of the SWNT bond network was followed by tracking the displacement of ≈ 100 tracer particles in the field of view using digital video microscopy [23]. Typically, 1-5 minutes of video data were obtained every 30 minutes over a 4 hour period spanning the gelation process. For cure times longer than 3 hours, the displacement of the tracers was comparable to the experimental noise; thus we limited the data presented herein to 3 hours or less cure time.

From the tracer trajectories we compute tracer particle mean square displacement (MSD): $\langle \Delta r_x^2(\Delta t) \rangle = \langle \Delta r_x(t, \Delta t) \Delta r_x(t, \Delta t) \rangle$, where $\Delta r_x(t, \Delta t) = r_x(t + \Delta t) - r_x(t)$ is the particle displacement in the x-direction during lag time Δt. Note, we calculated two-point MSDs as well [26] and obtained very similar data, but henceforth only one point MSD results will be shown due to its higher statistical resolution at the longest lag times. Owing to the difficulty of imaging through the strongly absorbing SWNT suspension and to minimize sample heating, it

was necessary for us to use a relatively long camera shutter time of $\sigma = 1/60\,s.$ on the video CCD camera (Hitachi KP-M1) to achieve adequate signal-to-noise levels in imaging. This led to the introduction of dynamic errors in the MSD, as described in Refs. [91, 92]. We have followed the procedure discussed in Ref. [92] to correct MSD data for dynamic error. The details of this procedure can be found in the Appendix. In the MSD results that follow, the data exhibited are dynamic error corrected.

6.2.3 Results and Discussion

As gelation proceeds, both the magnitude and functional form of the MSD changes. In Figure 6.1, we exhibit the particle MSD for different waiting times during gelation. For the earliest cure time (t = 10 min), the MSD is linear over the entire measurement window, corresponding to a particle diffusing in a Newtonian fluid with viscosity roughly three times larger than that of water. This observation indicates that steric entanglements between unbonded SWNTs do not induce non-Newtonian behavior at this volume fraction. As time progresses, the long lag time behavior of the MSD changes markedly, becoming progressively more sub-diffusive at t = 1 hr, and finally exhibiting a nearly flat plateau at t = 3 hr. Thus inter-tube bonding has progressed to modify the medium's rheological response from purely viscous to strongly elastic.

To extract the frequency-dependent (i.e., ω-dependent) viscoelastic moduli, $G^*(\omega)$, from the MSD, we analyze the data using the numerical approximation scheme detailed in Section 3.3.6 of Chapter 3. The moduli, exhibited in Figure 6.2, show clear rheological evidence of the sol-gel transition in the SWNT network as a function of gelation time. Below the critical gelation time 1 hr $< t^* <$ 2 hr, the rheology is dominated by the loss modulus $G''(\omega)$. Above t^*, the elastic modulus $G'(\omega)$ dominates at low frequency. For all gelation times in our data, $G'(\omega)$ exhibits

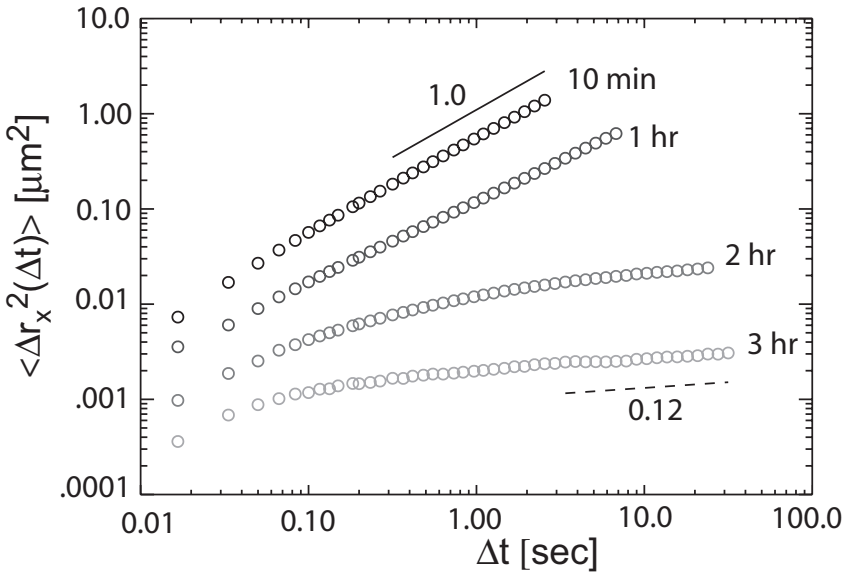

Figure 6.1: Mean Square Displacement for 2a = 0.46 μm particles in ϕ = 0.27 wt $\%$ SWNT, 10:1 NaDDBS:SWNT suspension for t = 10 min, 1 hr , 2hr, 3hr (top to bottom). Solid line is slope = 1.0, dashed line is slope = 0.12.

a weak frequency dependence ($\sim \omega^{0.3}$) characteristic of soft ($G' \approx 1\,Pa$) physical gels and of chemical gels of unbalanced stoichiometry [27]. (Note, we expect for strong gels ($G' \geq 100\,Pa$) that $G'(f = \frac{\omega}{2\pi} = 1\,Hz) = G'(f \to 0) = G'_0$, where G'_0 is the plateau modulus.)

For times longer than t^*, the moduli exhibit a point of crossover at which the viscous and elastic components are equal. This defines a crossover modulus, G_c, and crossover frequency, ω_c, both of which increase with the gelation time above t^*. By scaling the magnitude of G by G_c and the frequency ω by ω_c, we find that the network moduli exhibit a striking collapse. Figure 6.3A shows the data collapse under time-cure superposition [2, 117]. The resulting master curve reveals the viscoelastic relaxation of the NT gel over four decades in frequency. We can collapse the data from different NT concentrations and surfactant ratios onto the same master curve.

We parameterize the extent of the gelation via the dimensionless time parameter $\varepsilon = |t - t^*|/t^*$. Above the gel point, a zero-frequency finite elastic modulus appears and increases as

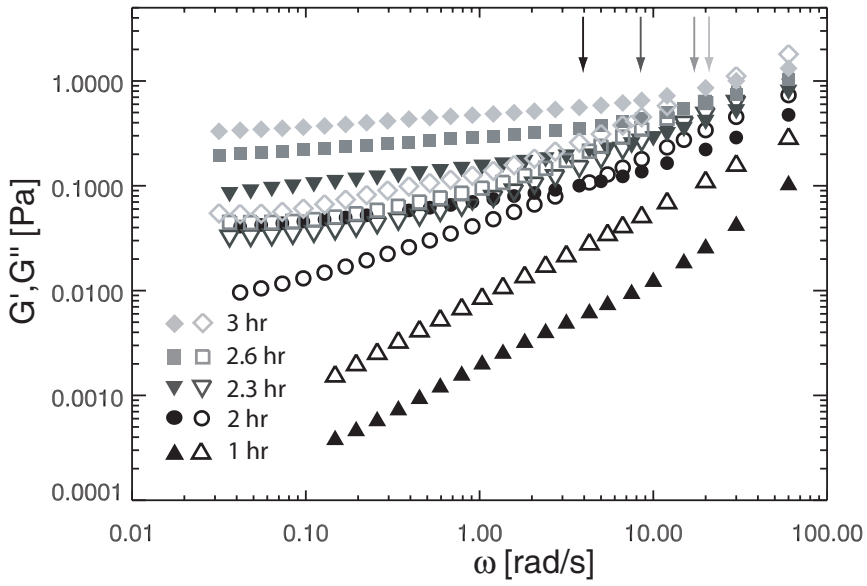

Figure 6.2: Viscoelastic Moduli $G'(\omega)$ (closed symbols) and $G''(\omega)$ (open symbols) derived from the MSD at different gelation times t. $t > 1.5$ hr are in the gel regime ($G' > G''$) data. $t < 1.5$ hr are in the the sol regime ($G' < G''$) data. Note that in the gel regime, there exists a crossover point [ω_c, G_c] where $G'(\omega_c)$ = $G''(\omega_c)$ = G_c indicated by the arrows.

a power law with ε. Experimentally we find $G_c \sim \varepsilon^z$ where $z \approx 1.03$ [Figure 6.3B]. For all gelation times in our data, ω_c is comparable to $\omega \equiv 2\pi f \approx 6.3$ rad/s [Figure 6.3C]; thus G_c and indeed, the low-frequency elastic modulus $G'(t, f = 1\,Hz)$, exhibit very similar scaling with gelation extent.

In any gelling network wherein both ω_c and G_c scale as power laws with the cure time [see Figures 6.3B,C], the viscoelastic moduli should be of similar functional form and should collapse under rescaling. Intuitively, ω_c is related to the mean relaxation time of the bonded rod clusters and G_c is related to their mean elastic modulus, both of which scale with the size of the bonded clusters. Thus the effect of an increase in the number of bonds corresponds, essentially, to a rescaling of time in the curing gel. As gelation proceeds ($t > t^*$) the bonds percolate, producing a change in connectivity without reorganization of the network structure. The collapse of the

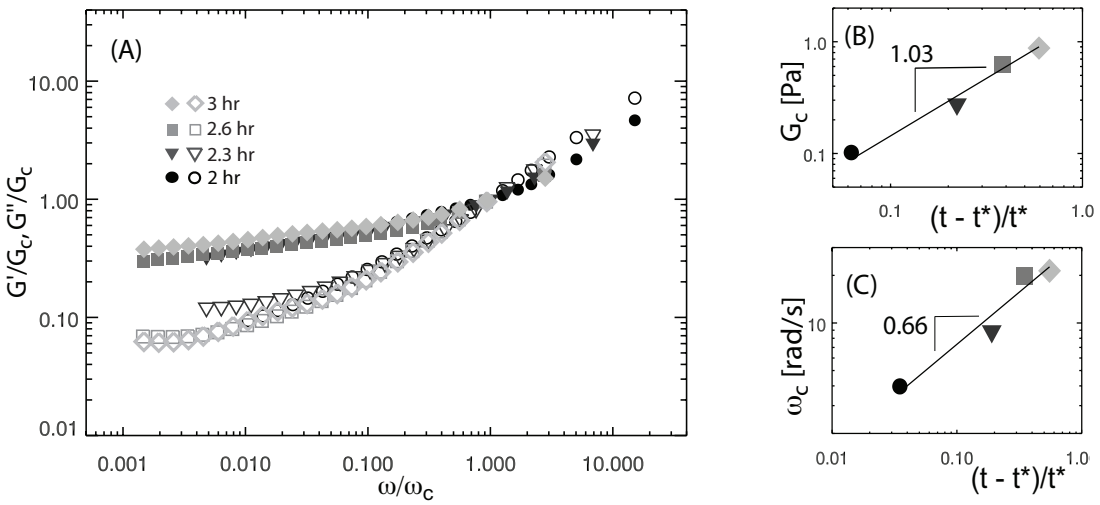

Figure 6.3: (A) Collapsed rheological master curve obtained by scaling $G'(\omega)$ (closed symbols) and $G''(\omega)$ (open symbols) by their respective crossover frequency ω_c and modulus G_c. (B) G_c vs gelation extent, scaling as $G_c \sim [(t-t^*)/t^*]^{1.03}$ with $t^* = 6777\,s$. (C) ω_c vs gelation extent, scaling as $\omega_c \sim [(t-t^*)/t^*]^{0.66}$ with $t^* = 6957\,s$.

viscoelastic moduli for the curing SWNT network under time-cure superposition highlights the crucial role of bonding between rods which we explicate further below.

6.3 Theory Section

Clearly, bonding between rods is the dominant contributor to the elasticity in the gel, since the number of rods is constant in time, whereas G' increases with time. Here we introduce a microscopic theory which establishes the relationship between elastic modulus G' and number of contacts N_c in the system, first for static and then dynamic networks. The first part of the theory derives, from the crossing probability of rods, a relation defining the number of contacts for a given density of randomly oriented rods. We then derive a relation for the shear modulus given an *effective* number of contacts which is a fraction of all contacts. These results are corroborated with computer simulations and are used to fit both static [47] and dynamic experimental rheology

data.

6.3.1 Static Model

The crossing probability of randomly oriented rods confined to a finite volume has an expected number of contacts, N_c, which depends purely on geometric parameters. A simple calculation yields an expression for the number density of contacts:

$$\frac{N_c}{V} = C\frac{L^2\sigma N_{rod}^2}{V^2} \sim \phi^2. \tag{6.1}$$

Here $\phi = \frac{\pi N_{rod} L\sigma^2}{4V}$ is the volume fraction of rods and rod diameter σ is assumed to be constant. Eq. 6.1 predicts the number of contacts in a randomly oriented network of rods as a function of the number of rods N_{rod}, rod length L, and rod diameter σ (note similar $L^2\sigma$ scaling is found in the excluded volume analysis of percolation at large rod aspect ratios [10]). The volume of the sample space is V. A full derivation of Eq. 6.1 is detailed in the remainder of this subsection.

We begin by considering the crossing probability of two rods with length L and center-to-center separation S. Both rods can assume any orientation in 3-dimensional space, and the boundary of possible orientations delimits a sphere of diameter L around each rod center. Clearly, the separation between rod centers must be less than the length of the rods, i.e., $S < L$, in order for them to potentially cross, as illustrated in Figure 6.4A. There are two cases of interest: (i) $0 < S < L/2$ and (ii) $L/2 < S < L$. When (i) is satisfied, the centers of both rods are in the overlap region, regardless of their angular orientations. Therefore, the probability of overlap is one. When (ii) is satisfied, the two spheres will overlap, and the solid angle Ω subtending their overlap region is directly proportional to the fraction of possible angular orientations that each

rod can assume whilst having a non-zero probability of overlapping the other rod. In turn, the probability of overlap P_{over} is just the product of the probabilities of each rod having the same angular restriction. Thus, having both rods in the overlap region is proportional to the square of the solid angle subtended by the overlap region:

$$P_{over} \propto \left(\frac{\Omega}{4\pi}\right)^2 = \frac{1}{(4\pi)^2}\left[\frac{4\pi L(L-S)}{L^2}\right]^2 = \left(1-\frac{S}{L}\right)^2. \tag{6.2}$$

Taken together, the probability of overlap for the two cases is

$$P_{over} = \begin{cases} 1 & \text{if} \quad 0 < S < \frac{L}{2} \quad (i) \\ 4 \times (1-\frac{S}{L})^2 & \text{if} \quad \frac{L}{2} < S < L \quad (ii) \end{cases} \tag{6.3}$$

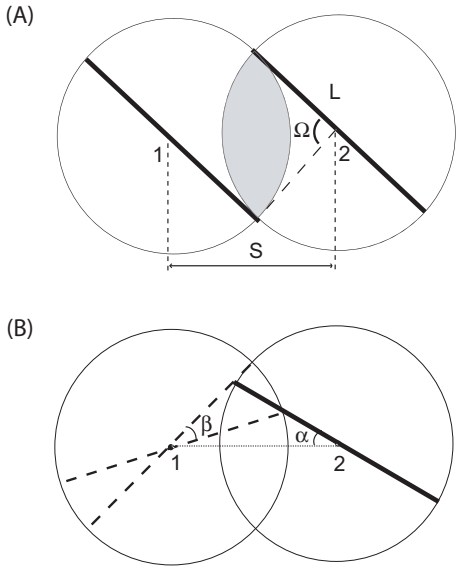

Figure 6.4: (A) Geometry of crossing probability of 2 rods of length L separated by distance S. Shaded region is overlap of the rod's spheres of possible angular orientation. Ω is the solid angle subtended by the overlap region. (B) Angles of possible intersections. β is the angular range of rod 1 that will cross rod 2 given rod 2 forms an angle α with respect to the separation axis.

Having both rods in the overlap region is a necessary but not sufficient condition to guarantee contact. There is an additional probability P_{ang} which depends on the relative angular orientations of the rods. The probability of crossing is given by $P_{cross} = P_{over} \times P_{ang}$. When both rods are in the overlap region, let the angle between rod 2 and the axis connecting two rod centers to be α, as shown in Figure 6.4B. The probability of rod 2 crossing rod 1 is proportional to the angle β subtending the projection of rod 2 onto the sphere of rod 1. Considering rotational symmetry with respect to the axis connecting the centers of rods 1 and 2, and the fact that the diameter of the rods $\sigma << L$, P_{ang} is

$$P_{ang} = \begin{cases} \int_0^{\pi/2} \frac{\beta(\alpha,\frac{S}{L})2\sigma L}{\pi L^2} \frac{\pi L^2 \sin\alpha}{\pi L^2} d\alpha & \text{if } \ 0 < S < \frac{L}{2} \quad (i) \\ \int_0^{\theta} \frac{\beta(\alpha,\frac{S}{L})2\sigma L}{\pi L(L-S)} \frac{\pi L^2 \sin\alpha}{4\pi L(L-S)} d\alpha & \text{if } \ \frac{L}{2} < S < L \quad (ii) \end{cases} \tag{6.4}$$

where for case (ii), θ is the largest angle that rod 2 can adopt whilst making contact with the sphere of rod 1. For case (ii), the angle breaks down into two subcases (iia) $\frac{L}{2} < S < \frac{L}{\sqrt{2}}$ and (iib) $\frac{L}{\sqrt{2}} < S < L$:

$$\theta = \begin{cases} \arcsin(\frac{L}{2S}) & \text{if } \ \frac{L}{2} < S < \frac{L}{\sqrt{2}} \quad (iia) \\ \arccos(\frac{S}{L}) & \text{if } \ \frac{L}{\sqrt{2}} < S < L \quad (iib) \end{cases} \tag{6.5}$$

Therefore, P_{cross} of two rods with length L and separation S is

$$P_{cross} = P_{over} \times P_{ang} = \frac{\sigma}{L} I\left(\frac{S}{L},\right) \tag{6.6}$$

where $I(\frac{S}{L}) = \frac{2}{\pi} \int_0^{\{\frac{\pi}{2},\theta\}} \beta(\alpha, \frac{S}{L}) \sin\alpha \, d\alpha$ for cases (i) and (ii) respectively.

Now consider the number of contacts or crosses one rod can have with other rods in its vicinity. Let the rod number density to be $n = \frac{N_{rod}}{V}$, where N_{rod} is the total number of rods and V is the volume of the gel. The mean number of contacts per rod, $\overline{N}_{c,1}$, is

$$\begin{aligned}
\overline{N}_{c,1} &= \int P_{cross} n dv \\
&= \int \frac{\sigma}{L} I\left(\frac{S}{L}\right) n dv \\
&= \frac{4\pi n\sigma}{L} \int_0^L I\left(\frac{S}{L}\right) S^2 dS \\
&= 4\pi n L^2 \sigma \int_0^1 I(x) x^2 dx. \qquad (6.7)
\end{aligned}$$

The contact density thus is

$$\begin{aligned}
\frac{N_c}{V} &= \frac{N_{rod} \times \overline{N}_{c,1}}{V} \\
&= 4\pi J \frac{L^2 \sigma N_{rod}^2}{V^2} \sim \phi^2, \qquad (6.8)
\end{aligned}$$

where J=$\int_0^1 I(x)x^2dx$=0.0403, and this is Eq. 6.1 above. A value of the numerical factor J obtained from simulations (detailed in the following section) is 0.11. The discrepancy between simulation and numerical evaluation of the integral is likely due to an underestimate of solid angles when α is very small.

6.3.2 Simulations of Rigid Rod Networks

Since we cannot directly observe the bonding between nanoscale rods in solution, computer simulations are employed to test the predictions of this theory. We construct static networks of monodisperse rods of length, $L = 10$, diameter, $\sigma = .05$, and aspect ratio, L/σ = 200, chosen to be comparable to the SWNTs in our experiments. (Note that the SWNTs used in the experiments are polydisperse in length. We also carried out simulations for rods with lengths drawn from a Gaussian distribution of comparable polydispersity to the SWNTs used in the experiments; a significant deviation of N_c/V from the results for monodisperse rods was not found.) The results that follow are from simulations of monodisperse rods.

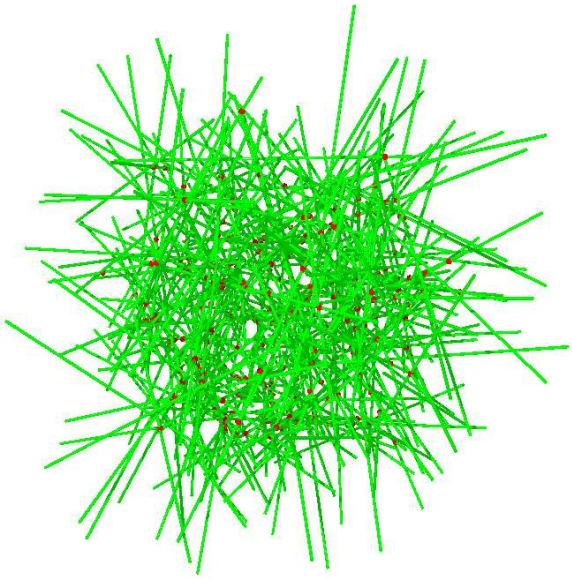

Figure 6.5: Snapshot of simulation for N = 100 rods of aspect ratio $L/\sigma = 200$ confined to a volume $V = 10^3$. Spheres indicate contacts between rods.

Rods are deposited randomly (off-lattice) in a 3-dimensional periodic cube with linear dimension $\ell = 20 - 40$. Then, we determine whether the randomly deposited rod central axes approach one another within a prescribed distance. Physically, we choose this distance to be

the rod diameter. A contact is said to form between two rods when the distance between their points of closest separation is less than or equal to the rod diameter. Note, this definition for contact permits rods to interpenetrate (i.e. soft core). A snapshot taken from a simulation is given in Figure 6.5, where dark spheres mark the points of intersection between rods located by the algorithm.

To test the scaling prediction of Eq. 6.1, we varied the sample volume (V ranged from 20^3 to 40^3) and rod length (L ranged from 5 to 10) while keeping rod diameter constant ($\sigma = .05$) in the simulations. In Figure 6.6A, we plot the number of contacts, N_c, versus the total number of rods, N_{rod}, in our simulations. Rescaling the N_c by V/L^2 in accordance with Eq. 6.1 yields a collapse of the data as shown in Figure 6.6B. This collapse validates the first piece of our theoretical model for the crossing probability of rigid rods. We next extend the model in two successive steps: first, we derive the macroscopic shear modulus from consideration of only elastically effective bonds, and, second, we derive the temporal evolution of elasticity assuming first order bonding kinetics.

Some bonds do not contribute to the shear modulus of the network; e.g., some rods will have only a single bond, and these non-contributing bonds need to be excluded when the shear modulus is computed. Physically, these bonds are akin to 'dangling' strands in polymer melts [30]. In Figure 6.7B, we illustrate two types of bonds that occur in a cluster of rods. The bonds denoted by circles belong to a pair of rods which are both connected to other rods, i.e., multiply connected bonds. The bonds denoted by stars, on the other hand, belong to a pair of rods for which one of the rods is not connected to any other rods, i.e., singly connected bonds. Physically we expect only the multiply connected bonds to respond elastically under shear and thus to contribute to

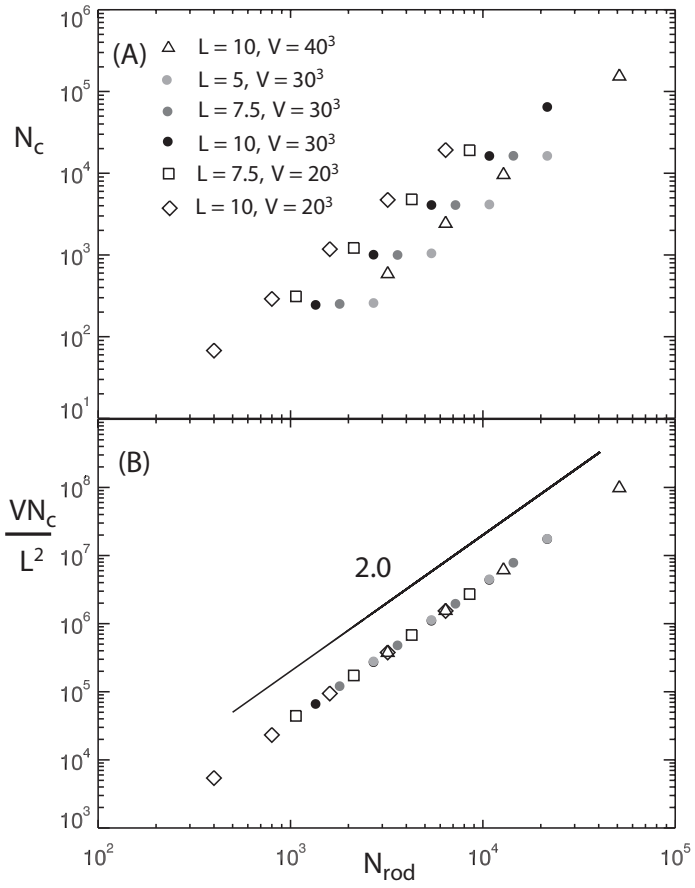

Figure 6.6: (A) Number of contacts vs number of rods in the simulation box. Data shown are for different box volumes and rod lengths. (B) Data collapse under rescaling of contact number by V/L^2. Solid line is slope 2.0.

the measured shear modulus in a rheology measurement, as depicted in Figure 6.7D. We define an exclusion probability $P_{exc} = N_s/N_c$, where N_s is the number of non-contributing bonds. When the volume fraction is low, almost all bonds are non-contributing bonds. The exclusion probability decreases as the packing fraction increases, as it is progressively more difficult for a rod or a cluster of rods to be isolated from the rest of the sample. We extract the volume fraction dependence of the P_{exc} from a simulated network with $V = 20^3$, $L = 10$, $\sigma = .05$. The results, exhibited in Figure 6.7A, show that the exclusion probability is well approximated

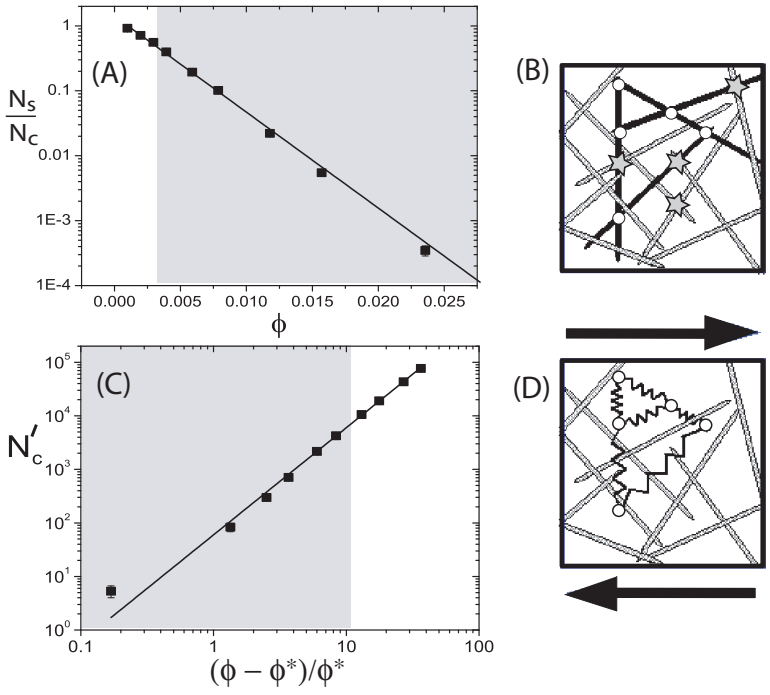

Figure 6.7: (A) Ratio of number of single bonds to number of total contacts (N_s/N_c) vs volume fraction from simulation. Solid line is fit to $e^{-B(\phi-\phi^*)/\phi^*}$ with $\phi^* = (1.0 \pm 0.1) \times 10^{-3}$ and $B = 0.345 \pm 0.036$. Shaded region corresponds to concentration regime of rheology data in Figure 6.8. (B) Cartoon of rod network showing multiply connected bonds (circles) and single bonds (stars). Multiply connected rods are black. (C) Number of contacts with single bonds removed ($N_c^{'} = N_c - N_s$) vs. $(\phi - \phi^*)/\phi^*$ from simulation. Solid line is fit to Eq. 6.9 (see text) with $A = (781.5 \pm 2.2) \times 10^5$, $\phi^* = (8.35 \pm 1.46) \times 10^{-4}$, and $B = 0.253 \pm 0.068$. (D) Cartoon illustrating that only the non-single bonds contribute to an elastic response under shear.

by an exponential function: $P_{exc} = e^{-B(\phi-\phi^*)/\phi^*}$, where ϕ^* is the volume fraction at which the sample starts to develop a shear modulus and B is a dimensionless parameter characterizing the rate of decrease of non-contributing bonds with increasing ϕ. Note, this theoretical form is one of several possible functions; here we chose a natural form with a minimum number of free parameters.

Thus the density of bonds that contribute to the sample shear modulus is

$$\frac{N_c'}{V} = \frac{N_c}{V}(1 - P_{exc})$$
$$= A\phi^2(1 - e^{-B(\frac{\phi-\phi^*}{\phi^*})}), \tag{6.9}$$

where A is a constant of proportionality. The number of elastically effective contacts (N_c') is given by the total number of contacts minus the number of single bonds (i.e. $N_c' = N_c - N_s$). From the simulation data of Figure 6.7A, we obtain the number of effective contacts and plot it versus the volume fraction of rods. The results, exhibited in Figure 6.7C, show that N_c' is well fit by Eq. 6.9.

6.3.3 Comparison with Rheology Experiments

Our previous rheological measurements yielded a scaling of the low frequency elastic modulus $G'(\phi, f = 1\,Hz)$ with rod volume fraction which was well described by the critical power law form $A[(\phi - \phi^*)/\phi^*]^\beta$ with $\phi^* = 0.0027 \pm 0.0002$ and $\beta = 2.3 \pm 0.1$ [47]. It is worth noting that the simple power law $A\phi^2$ does not fit the rheology data at all, confirming that the data are in a regime (indicated in the shaded areas of Figures 6.7A and 6.7C) where we expect a relatively high fraction of single bonds to have a significant effect on the measured shear modulus. It follows that if $G' \sim N_c'$, then Eq. 6.9 should also fit the volume-fraction dependent G' rheological data with only a different constant of proportionality. Indeed, as Figure 6.8 attests, we find comparable fit quality when comparing Eq. 6.9 against $A[(\phi - \phi^*)/\phi^*]^\beta$ for the rheological data of Ref. [47]. Note, both expressions have three free parameters. While the critical power law form is more commonly used to fit scaling data for gelation, it is largely

empirical. Eq. 6.9, on the other hand, has been derived from the crossing probability of rods in a confined geometry, augmented with minimal assumptions about the relative contribution to the shear modulus from bonds with differing degrees of connectivity. The discrepancy between the values of ϕ^* and B obtained from fitting Eq. 6.9 to simulations ($\phi^* = (8.35 \pm 1.46) \times 10^{-4}$, $B = 0.253 \pm 0.068$) and experiments ($\phi^* = 0.0028 \pm 0.0001$, $B = 0.053 \pm 0.007$) is likely due to the fact that our model does not exclude the bonds in higher-order structures such as non-spanning clusters and dangling closed loops. In a real network these structures will not contribute to elasticity, resulting in a higher value for ϕ^*, consistent with our fitted values for ϕ^*. Instead, we have focused on excluding the simplest structures (single bonds) which, while sidestepping complicated considerations such as finite-size effects, may have come at the expense of exact quantitative agreement between ϕ^* and B between the simulations and experiments.

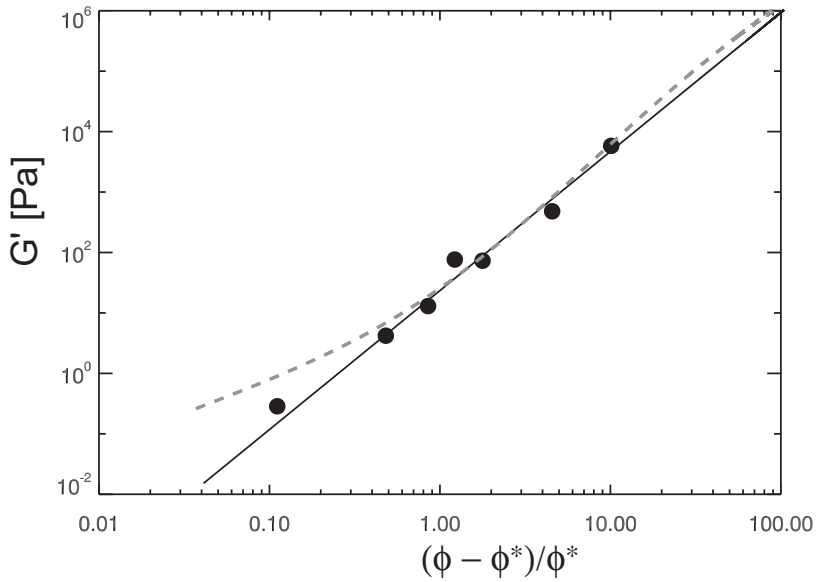

Figure 6.8: Low-frequency elastic modulus $G'(f = 1\,Hz)$ vs. volume fraction from rheology. Data is taken from Ref. [47]. Dashed line is fit to Eq. 6.9 with $\phi^* = 0.0028 \pm 0.0001$ and $B = 0.053 \pm 0.007$. Solid line is fit to critical power law $A[(\phi - \phi^*)/\phi^*]^\beta$ with $\phi^* = .0027 \pm 0.0002$ and $\beta = 2.3 \pm 0.1$.

6.3.4 Comparison with Microrheology Experiments

To compare with the dynamic results from the present microrheology experiments, we extend our theoretical model for static rod networks to account for the time evolution of rod bonding in an adequately dispersed sample. At any given time, N_f free rods are not bonded to any other rods, and N_b rods are bonded, $N_f + N_b = N_{tot}$. At t = 0, we take $N_f = N_{tot}$, and $N_b = 0$. Conversely, at t = ∞, we take $N_b = N_{tot}$, and $N_f = 0$. The rate of bonding is proportional to the number of free rods that are actively seeking bonds and to the total number of rods that are candidates for additional bonding. Accordingly, the time dependence of bond formation is given by the rate equation: $\frac{dN_f}{dt} = -\gamma N_f N_{tot}$ where γ is the bonding rate. Integrating the rate equation and applying boundary conditions yields the number of bonded rods as a function of time:

$$N_b = N_{tot}(1 - e^{-\gamma N_{tot} t}). \tag{6.10}$$

Substituting N_b for N_{rod} in the static analysis of Eqns. 6.1 and 6.9 yields the time evolution of the low-frequency elastic modulus:

$$G' = A\phi^2(1 - e^{-\gamma\phi t})^2 \left[1 - e^{-B(\frac{\phi(1-e^{-\gamma\phi t})-\phi^*}{\phi^*})}\right]. \tag{6.11}$$

Eq. 6.11 suggests that G' will eventually saturate (i.e., $G' \rightarrow A\phi^2$ as $t \rightarrow \infty$) when all possible bonding rods are exhausted. The elastic modulus $G'(t, f = 1\,Hz)$ for different cure times, shown in Figure 6.9, can be fit by a power law form $A[(t - t^*)/t^*]^z$ with $z = 1.3 \pm 0.2$. This is not surprising as the sample is rather dilute, and the time it takes for G' to saturate lies

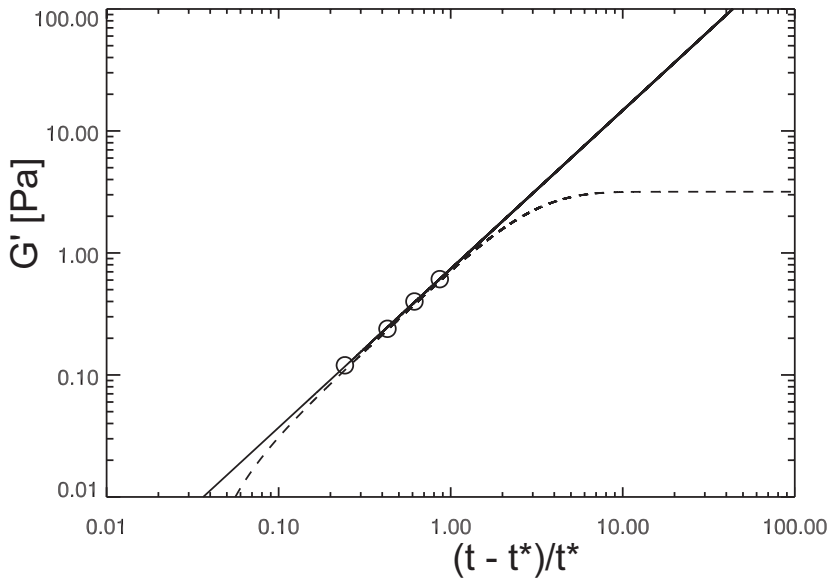

Figure 6.9: Low-frequency elastic modulus $G'(f = 1\,Hz)$ vs. cure time from microrheology. Dashed line is fit to Eq. (6.11) with $\phi = 0.006 \pm 0.001$, $\gamma = 0.0175 \pm 0.007$, $\phi^* = .0028$, and $B = 0.053$. Solid line is fit to power law $A((t - t^*)/t^*)^z$ with $t^* = 5793 \pm 479\,s.$ and $z = 1.3 \pm 0.2$

outside our experimental window. Physically, however, G' must saturate on approach to its fully cured value, corresponding to the modulus at which all available rods are bonded. Clearly this saturation behavior is not captured in the power law, which grows indefinitely ($G' \to A(t/t^*)^z$ as $t \to \infty$). Thus, the power law is at best an empirical local approximation to a saturating functional form. We can fit the microrheology data equally well to either Eq. 6.11 or the power law $A[(t - t^*)/t^*]^z$, as shown in Figure 6.9, due to the limited dynamic range of the data. In fitting Eq. (6.11), we have fixed $\phi^* = .0028$ and $B = 0.053$, the values extracted from the rheology data fitting of Figure 6.8. As a result, both functional forms have three parameters. In principle, we could have further constrained ϕ in Eq. 6.11. However, to account for modulus variations between the two datasets due to sample preparation, it was necessary to let ϕ vary. Nonetheless, the nearly indistinguishable fitting over the dynamic range of our data suggests

that its time dependence is well captured by our model. Measurements for longer cure times are clearly needed to conclusively test Eq. 6.11.

6.4 Conclusions

We have performed microrheological measurements of the gelation of a semidilute suspension of single-wall carbon nanotubes. The results implicate inter-tube bonding as the dominant contributor to elasticity in the system. To elucidate the quantitative dependence of the number of bonds on geometric parameters characterizing the rods, we have derived an expression, based on the crossing probability of rods confined to a finite volume, which yields the dependence of number of contacts on the density, length, and diameter of the constituent rods. The relation is shown to be in agreement with the scaling of the number of contacts for simulated rigid rod networks. To make connection with the shear modulus measured in rheology experiments, we have assumed that only the fraction of bonds belonging to multiply connected rods contribute to the network's elasticity. With this assumption, we derived a relation that fits the static macro- and dynamic micro- rheological data with a goodness-of-fit comparable to empirically derived critical power laws. Future rheological measurements or detailed finite element simulations with larger dynamic range are needed to decisively test the models.

Chapter 7

Conclusions and Future Work

7.1 Summary

In recent years, an interdisciplinary community of physicists, chemical- and bio-engineers, and cell biologists has coalesced around the suite of experimental techniques termed microrheology. What do they, and we, hope to gain from this endeavor? To answer this question, we need only step back and unpack what we have learned from the experiments in this thesis.

We have described experiments in this thesis wherein microrheology has been used to extend the possibilities of traditional macrorheology measurements in soft materials. A unifying theme of our work is that a combination of simple microrheology experiments and theoretical modeling can yield powerful insights into the inner workings of soft materials. In the experiments of Chapter Four on λ-DNA, we have shown how a combination of one- and two-point passive microrheology measurements can be used to extract both local and bulk shear moduli of a polymeric network with depletion-induced mechanical inhomogeneities surrounding the particle. Whereas bulk macrorheology is the *de facto* standard method for obtaining the bulk response

of materials, it remains relatively mute on local material properties. Thus the significance of our work is that we have shown how microrheology, alone, can be used to derive a comprehensive characterization of an inhomogenous soft material. The work was the first systematic measurement in a well-characterized model system to convincingly validate the two-point hypothesis of Crocker [26] and the theoretical framework for understanding one- and two-point microrheology developed by Levine and Lubensky [59–61].

In the bacterial bath experiments described in Chapter Five, we have demonstrated that one- and two-point microrheology can be used fruitfully to characterize the fluctuations and responses of an active non-equilibrium system, comprised of actively swimming bacteria. A bacterial bath constitutes an instance of a frontier class of soft materials, termed active matter, whose utilities and ramifications are just beginning to be explored [85]. Active matter differs from its equilibrium counterpart primarily in that fluctuations and responses are no longer constrained by the Fluctuation-Dissipation Theorem. Our work quantitatively measured the departure from equilibrium for a dilute bacterial bath. We found that the departure form equilibrium depends on the manner in which the bacteria are actively forcing the medium, i.e., whether they are running or tumbling. Whereas previous tracer-based investigations of bacterial baths have relied exclusively on one-point measurements, we have shown that one-point measurements yield results which can depend on the size of the tracer and are thus intrinsically ambiguous in situations wherein tracer and active particle are of comparable size. Two-point measurements, by contrast, yield fluctuations which are independent of tracer size. Thus a significant contribution of our work is to show that two-point measurements are essential to robustly characterize fluctuations

in active swimmer systems, confirming expectations based on earlier studies in passive equilibrium materials [18] and active living cells [57]. Additionally, the phenomenological theoretical framework developed by Lau and Lubensky [58] to understand our results, may also prove useful for other active matter systems such as active gels of biopolymers and motor proteins.

Finally in the work on gelling carbon nanotube networks of Chapter Six, we demonstrated an important application of microrheology: characterization of the process of gelation in rigid rod networks. The process of gelation between macromolecular constituents is relevant in both materials (e.g. composite materials) and biological (e.g. cell motility) contexts. In the former case, the initial stages of gelation are difficult to characterize using traditional macrorheological methods due to the fact that the incipient gel is characterized by extremely small initial moduli and fragile structures that are easily compromised in a typical stress-controlled bulk rheometer. In the latter case, the stringent requirement not to denature biological functionality requires an *in situ* method of characterization such as microrheology, rather than bulk characterization via macrorheology on reconstituted cell lysates. To rationalize our micro- and macro- rheological data for the time and concentration dependence of the shear modulus in the gelling nanotube network, we have utilized computer simulations in concert with analytical modeling; this approach led us to deduce that the number of inter-tube contacts is a key parameter governing the rheological response of the network. Elementary considerations of inter-tube bonding lead to predictions beyond empirical power laws for the scaling of shear modulus with concentration and cure time. For time dependence in particular, consideration of first order bonding kinetics readily predicts saturation in the number of contacts with cure time which should also lead to

saturation in the shear modulus of the gelling network. Decisive tests of our model can be obtained via higher dynamic range rheological measurements in nanotube networks. In principle, electrical and thermal conductivity should depend on inter-tube contacts and thus our model, with modest modifications, should also yield insight into these types of measurements.

7.2 Future Directions

Here we describe new directions for the work in this thesis. New work encompasses both further exploitation of microrheology and also further exploration of the system classes we have considered.

7.2.1 Characterization of inhomogeneities in soft materials

In our study of depletion, we learned that the the hydrodynamic layer is different from the depletion layer. This leads us to consider what other types of local boundary effects may be studied. One possibility arises in particle diffusion in two-fluid systems, where the fluids demix with one fluid component preferentially wetting the particle surface, leading to a shell of different fluid composition surrounding the particle. This situation is encountered in, e.g., water-lutidine mixtures close to the critical temperature [45]. Thus, a microrheological analysis similar to ours may be useful to characterize the thickness of the fluid boundary layer in this system class.

While we have worked out the detailed case of depletion in Chapter Four, there remain many other possibilities for the mechanical inhomogeneities surrounding a probe particle which have yet to be carefully considered. This class of phenomena has relevance for probe-based microrheology measurements and also for study of inclusions in composite materials and transport

in crowded environments, e.g., in the interior of cells. A simple and potentially interesting related experiment could explore whether a local shell of higher density, as expected for a particle with attractive interactions with the medium, would lead to an inverse situation in which one-point measurements overestimate the bulk rheology. And if so, whether the basic shell model of Levine and Lubensky [61], with modest modifications, could also quantitatively account for the measured particle mobilities. To date, this scenario has not been experimentally considered.

7.2.2 Active Matter: active depletion and time-reversal microrheology

The study of active matter is currently in its infancy and, consequently, many opportunities exist for microrheological techniques to contribute to our understanding. A general avenue of investigation under consideration in the community concerns whether active systems can be harnessed to enable self-assembly beyond what is possible in equilibrium systems. In equilibrium systems, for example, depletion interactions can be used to assemble large particles in a suspension of smaller particles. What would happen if the smaller particles were active? Alternatively, what happens to the depletion phenomena in systems at high Peclet number, wherein the sea of smaller particles constitutes an 'active fluid' microstructure driven out of equilibrium via active internal forces. Viewed in this way, the depletion force induced by the active smaller particles on the larger particles might be more appropriately described as Bernoulli-like forces in which an imbalance between the velocity of the flowing active fluid within an excluded volume region between two large particles and the bulk fluid velocity surrounding them gives rise to a pressure imbalance that drives them together, rather than an osmotic pressure imbalance as in the case of equilibrium depletion.

While we have demonstrated that a combination of active and passive microrheology can reveal whether a system is in thermal equilibrium, an intriguing possibility is whether such a determination could be made via passive microrheology measurements alone. One possible analytic scheme to achieve this goal was proposed by Steinberg in Ref. [101]. In this paper, it was theoretically shown that time reversal of higher order autocorrelation functions of a system's noise can be used to distinguish systems that are in equilibrium from systems that are out of equilibrium. Conventional first-order time-forward autocorrelation functions, $G(\tau) = \langle f(t+\tau)f(t)\rangle$, are invariant under time reversal ($t \longrightarrow -t$), i.e. $G_r(\tau) \equiv \langle f(-(t+\tau))f(-t)\rangle = G(\tau)$ where $f(t)$ denotes a function of the system's stochastic noise which can be, e.g., voltage fluctuations $V(t)$ of a patch-clamped ion channel or position $x(t)$ of a fluctuating Brownian particle. However, higher order moments of the autocorrelation function of the system's noise, i.e., $G^{\alpha\beta}(\tau) = \langle f^{\alpha}(t+\tau)f^{\beta}(t)\rangle$ where $\alpha \neq \beta \geq 1$, are in general not necessarily invariant under time reversal, i.e., $G_r^{\alpha\beta}(\tau) \neq G^{\alpha\beta}(\tau)$. It can be shown that $G_r^{\alpha\beta}(\tau) = G^{\alpha\beta}(\tau)$ holds in general if and only if the underlying process that generates the noise obeys detailed balance, as is the case for systems in equilibrium. This opens the possibility that a comparison of $G_r^{\alpha\beta}(\tau)$ and $G^{\alpha\beta}(\tau)$ would constitute a "one-shot" method to determine whether a system is in equilibrium via analysis of the noise fluctuations of the system alone. Moreover, if true, then the departure from equilibrium may perhaps be quantitatively correlated with the difference between the time-reversed autocorrelation function and the time-forward autocorrelation function, $\Delta(\tau) = G_r^{\alpha\beta}(\tau) - G^{\alpha\beta}(\tau)$. Bacterial baths, owing to the relative ease with which control parameters could be tuned, are an attractive model system to test the validity of this "time-reversal

microrheology" scheme for active matter systems. A preliminary experiment would entail measuring the trajectories of particles in an active bacterial bath and computing the $G^{\alpha\beta}(\tau)$ and $G_r^{\alpha\beta}(\tau)$ using the time-forward and time-reversed trajectories, respectively. The next step would be to check whether there are systematic deviations between the two and how they depend on the lag time τ. Naively, we would expect the deviation $\Delta(\tau)$ to be larger at long lag times where the deviation from equilibrium is largest for the bacterial bath, based on our passive and active microrheology measurements.

7.2.3 Self-healing Materials

The ability of the nanotube gel (and many other soft glassy materials) to be rejuvenated under shear (e.g. with sonication) classifies them as "self-healing" materials. Currently, there is widespread interest in identifying the mechanisms of self-healing in various materials with the goal of engineering them for use in "real-world" applications [22]. From a technological standpoint, there are many obvious potential uses for self-healing materials. These range from materials to reinforce structures subject to high stresses such as building columns in seismically active regions or airplane wings to biocompatible materials such as DARPA's proposal to develop a "battlefield putty" that is capable of temporarily mending wounds in battlefield situations. Microrheology is well suited as a technique to characterize the detailed mechanisms of these materials. For example, variants of the active microrheology experiment can be used to locally tear the material and then passive microrheology could be used to subsequently monitor the recovery of the material as a function of both length and time.

What lies in the future is anybody's guess. But it seems fair to say that given the current trend toward miniaturization (and accompanying small-scale measurements) across the scientific

disciplines, the knowledge afforded by microrheological techniques will play an increasing role in our understanding of soft materials.

Appendix A

Correction for Dynamic Errors in MSD data of Chapter 6

We use the procedure outlined in Section 3.3.4 of Chapter 3 to correct our dynamic error in our MSD data. The first step is to find a suitable functional form to fit the MSD. With the exception of the earliest time data at t = 10 minutes, our MSDs are not linear, thus precluding the use of the Newtonian fluid model of Eq. 3.14. The next simplest form is a power law MSD: $\langle \Delta x^2(\tau) \rangle = A\tau^\alpha$. Plugging this form into Eq. 3.13 yields:

$$\langle \Delta x^2(\tau, \sigma) \rangle = A\sigma^\alpha \frac{\left(\frac{\tau}{\sigma}+1\right)^{2+\alpha} + \left(\frac{\tau}{\sigma}-1\right)^{2+\alpha} - 2\left(\frac{\tau}{\sigma}\right)^{2+\alpha} - 2}{(1+\alpha)(2+\alpha)} \tag{A.1}$$

which is Eq. (30) in Ref. [92]. Eq. A.1 described the t = 1 hr data well, shown in Figure A.1.

However, the power law form did not work for $t \geq 2$ hr post-gel data, as shown in Figure A.1. The poorness of the fits, particularly at the short lag times, indicates that the downward curvature cannot wholly be accounted for by dynamic error alone. Otherwise, we would have been able to obtain good fits of the MSDs with Eq. A.1 as in the t = 1 hr data. Thus, the

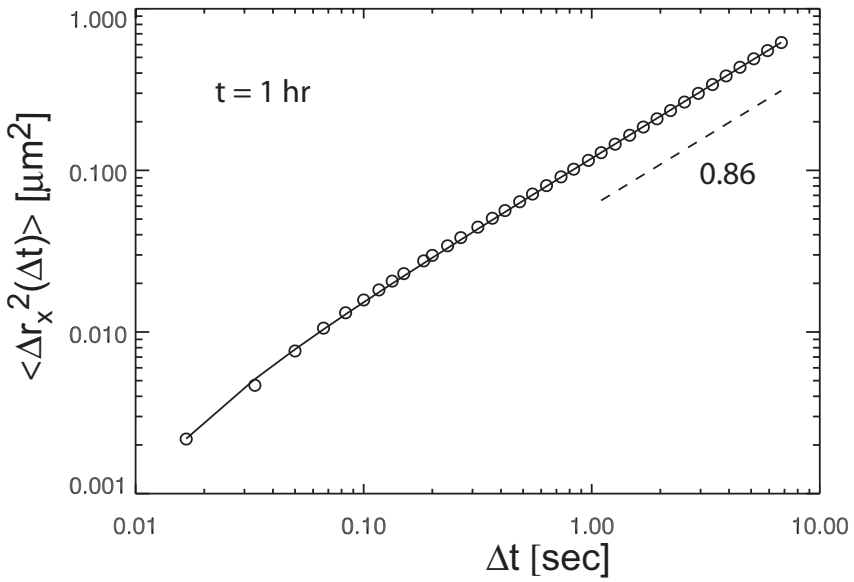

Figure A.1: mean square displacement for t = 1 hr data. Solid line is a fit to Eq. A.1

downward curvature is a feature of the relaxation of the gel network.

A natural choice to describe the tracer MSD expected for a gel would be the Voigt model, considered in Eq. (22) of Ref. [92]. However, we found that the single relaxation time exponential saturation described by the Voigt model was insufficient to capture the slow saturation of our data which grows as a weak power law over our entire experimental time window. Moreover, we have a further constraint due to scaling considerations: the functional form for the data must be consistent with collapse under time-cure superposition scaling (i.e. $f(G,\omega) = (G/G_0)f(\omega/\omega_0)$). The simplest functional form that described the behavior of our data well was the empirical form: $\langle \Delta x^2(\tau) \rangle = A \ln(1 + \tau/\tau_0)$. Note that this form is not expected to be the true form since gels must saturate at long times and the logarithm does not, but it is good over the dynamic range of our data. Plugging into Eq. 3.13 yields:

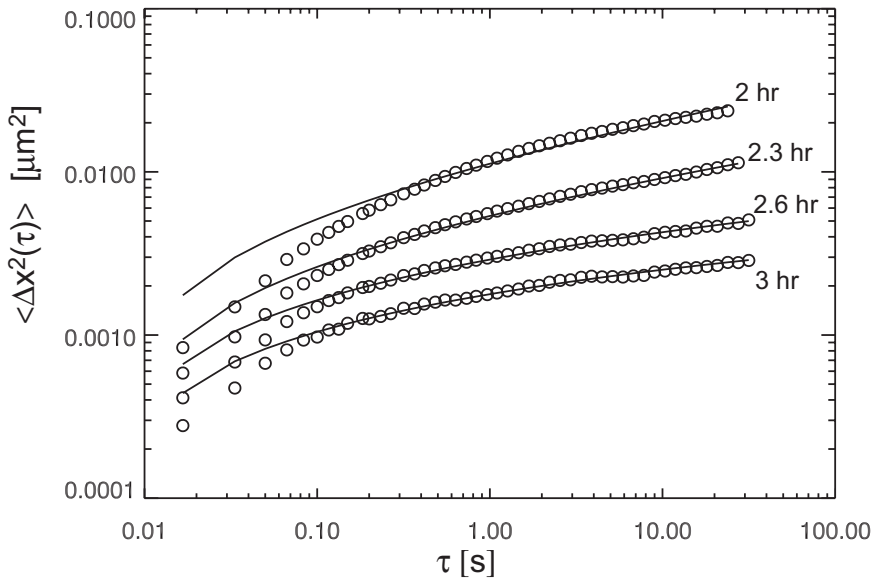

Figure A.2: Post-gel MSD data (circles) along with the best fit (lines) to Eq. A.1.

$$\begin{aligned}\langle \Delta x^2(\tau,\sigma)\rangle =& \frac{A\tau_0}{\sigma} - \frac{A}{2}\left(\frac{\tau+\tau_0}{\sigma}-1\right)^2 \ln(\tau+\tau_0)+ \\ & A\left[\frac{1}{2}-\left(\frac{\tau+\tau_0}{\sigma}\right)\left(1+\frac{\tau+\tau_0}{2\sigma}\right)\right]\ln\left(1+\frac{\tau}{\tau_0}\right)+ \\ & \frac{A}{2}\left(\frac{\tau+\tau_0}{\sigma}-1\right)^2\ln(\tau+\tau_0-\sigma) - A\left(1+\frac{\tau_0}{\sigma}\right)^2\ln\left(1+\frac{\sigma}{\tau_0}\right)+ \\ & \frac{A}{2}\left(1+\frac{\tau+\tau_0}{\sigma}\right)^2\ln\left(1+\frac{\tau+\sigma}{\tau_0}\right). \end{aligned} \tag{A.2}$$

We find a good fit for the post-gel data using Eq. A.2, as shown in Figure A.3.

Using Eq. 3.14 for t = 10 min, Eq. A.1 for t = 1 hr, and Eq. A.2 for $t \geq 2hr$, we are able to correct for the dynamic errors in all our MSD data. In Figure A.4 we show the results of the correction. The solid line is the dynamic error-biased data and the dashed lines are the data after their respective corrections have been made. For the $t \leq 1hr$ data, the downward curvature has

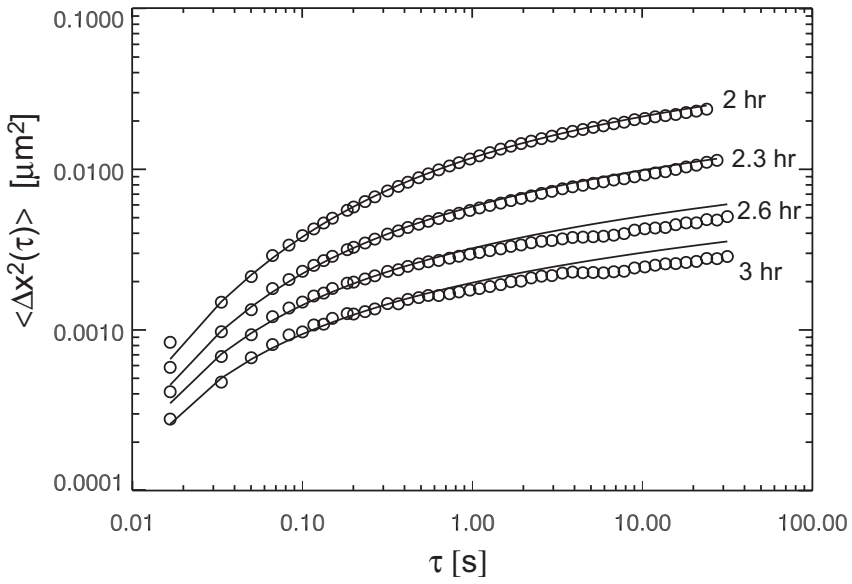

Figure A.3: Post-gel MSD data (circles) along with the best fit (lines) to Eq. A.2.

been largely eliminated, confirming that it was an artifact of dynamic error. For the $t \geq 2hr$ data, however, the downward curvature persists, indicating that it is a feature of the relaxation dynamics of the SWNT gel.

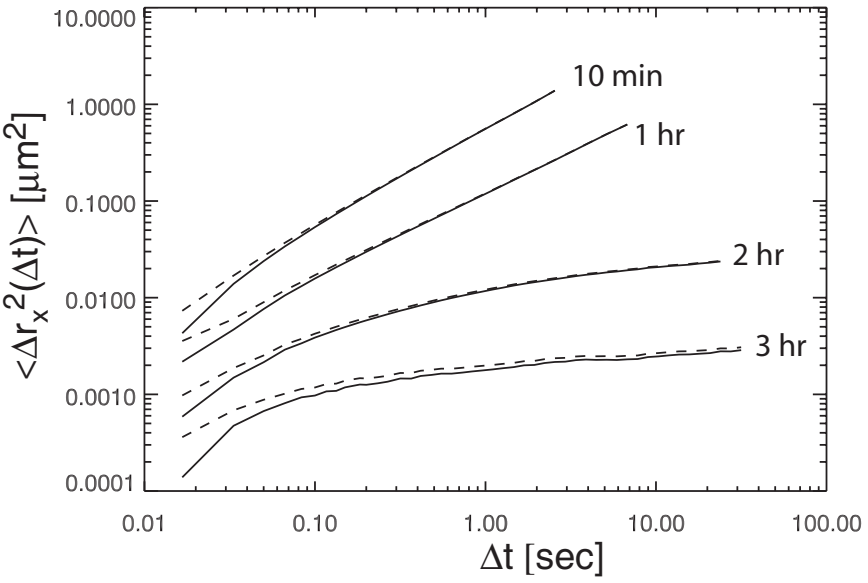

Figure A.4: mean square displacement for t = 10 min, 1hr, 2hr, and 3 hr. Solid lines are the uncorrected MSD. Dashed lines are the dynamic error corrected MSD.

The dynamic error corrected MSDs, denoted by the dashed lines in the figure, are exhibited in Figure 6.1 and is used to calculate the viscoelastic moduli exhibited in Figures 6.2 and 6.3. Comparing the moduli obtained with the dynamic error-biased data and without in Figure A.5, indicates that dynamic error can shift the crossover of the moduli and tends to affect the viscous modulus to a greater extent than the storage modulus in our post-gel data.

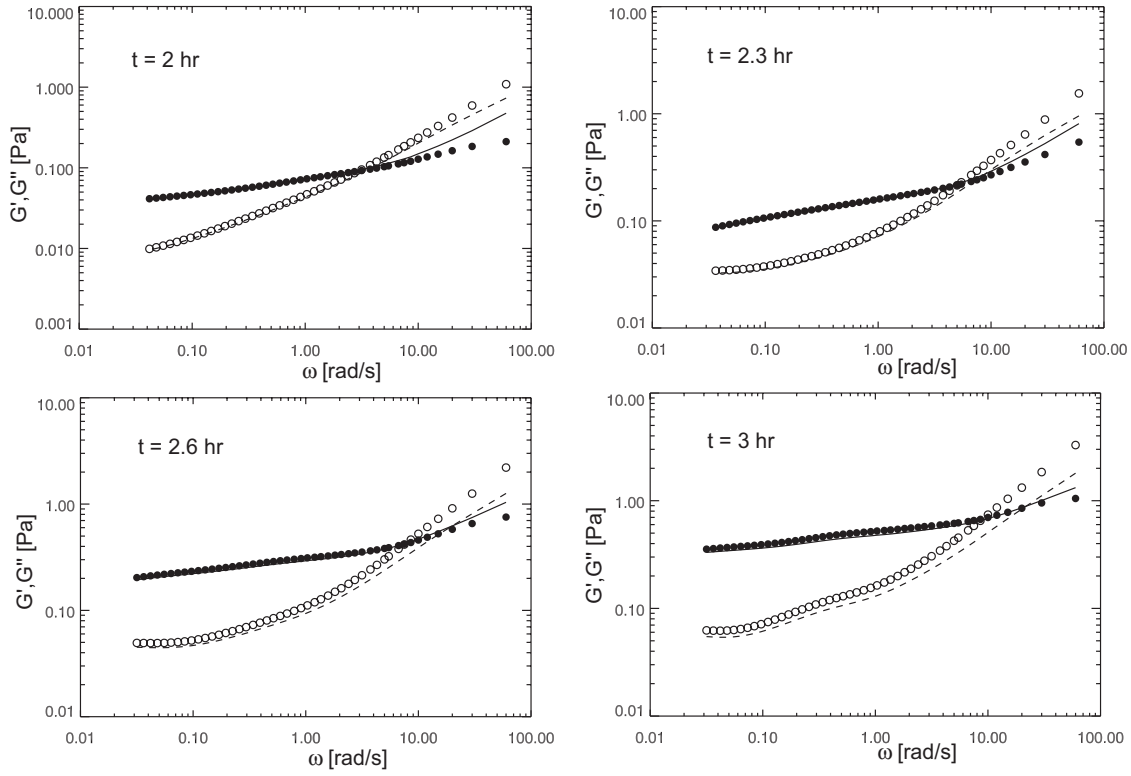

Figure A.5: Viscoelastic moduli derived from the MSD for gel times above the percolation transition. G' and G" derived from dynamic error-biased MSD data are solid and open circles respectively. Solid and dashed lines are the G' and G", respectively, derived from the dynamic error corrected MSD.

The dynamic error corrected $G^*(\omega)$ data denoted by the solid and dashed lines is exhibited in Figures 6.2, 6.3, and 6.9.

Bibliography

[1] J. Adler and B. Templeton. The effect of environmental conditions on the motility of *Escherichia coli*. *J. gen. Microbiol.* **46**, 175 (1967).

[2] D. Adolf and J. E. Martin. Time-cure superposition during cross-linking. *Macromolecules* **23**, 3700 (1990).

[3] U. Alon, L. Camarena, M. G. Surette, B. A. y Arcas, Y. Liu, S. Leibler, and J. B. Stock. Response regulator output in bacterial chemotaxis. *EMBO J.* **17**(15), 4238 (1998).

[4] A. M. Alsayed. *Melting in Temperature Sensitive Suspensions*. PhD dissertation University of Pennsylvania Department of Physics and Astronomy Aug (2006).

[5] I. S. Aranson, A. Sokolov, J. O. Kessler, and R. E. Goldstein. Model for dynamical coherence in thin films of self-propelled microorganisms. *Phys. Rev. E* **75**, 040901 (2007).

[6] S. Asakura and S. Oosawa. Interaction between particles suspended in solutions of macromolecules. *J. Polym. Sci.* **33**, 183 (1958).

[7] A. Ashkin. Acceleration and trapping of particles by radiation pressure. *Phys. Rev. Lett.* **24**, 156 (1970).

[8] A. Ashkin, J. M. Dziedzic, J. E. Bjorkholm, and S. Chu. Observation of a single-beam gradient force optical trap for dielectric particles. *Opt. Lett.* **11**, 288 (1986).

[9] M. Atakhorrami, G. Koenderink, C. Schmidt, and F. MacKintosh. Short-time inertial response of viscoelastic fluids: observation of vortex propagation. *Phys. Rev. Lett.* **95**(20), 208302 (2005).

[10] I. Balberg, C. H. Anderson, S. Alexander, and N. Wagner. Excluded volume and its relation to the onset of percolation. *Phys. Rev. B* **30**(7), 3933 (1984).

[11] G. K. Batchelor. Brownian diffusion of particles with hydrodynamic interaction. *J. Fluid Mech.* **74**, 1 (1976).

[12] H. Berg. *E. coli in Motion*. Springer New York, USA 1st edition (2004).

[13] B. J. Berne and R. Pecora. *Dynamic Light Scattering with Applications in Chemistry, Biology, and Physics*. Dover Publication Inc. New York, USA 1st edition (2000).

[14] M. B. Bryning. *Carbon Nanotube Networks in Epoxy Composites and Aerogels*. PhD dissertation University of Pennsylvania Department of Physics and Astronomy May (2007).

[15] P. Bursac, G. Lenormand, B. Fabry, M. Oliver, D. A. Weitz, V. Viasnoff, J. P. Butler, and J. J. Fredberg. Cytoskeletal remodelling and slow dynamics in the living cell. *Nature Materials* **4**, 557 (2005).

[16] P. M. Chaikin and T. C. Lubensky. *Principles of Condensed Matter Physics*. Cambridge University Press Cambridge, UK 1st edition (1995).

[17] H. Chate, F. Ginelli, and R. Montagne. Simple model for active nematics: Quasi-long-range order and giant fluctuations. *Phys. Rev. Lett.* **96**(18), 180602 (2006).

[18] D. T. Chen, E. R. Weeks, J. C. Crocker, M. F. Islam, R. Verma, J. Gruber, A. J. Levine, T. C. Lubensky, and A. G. Yodh. Rheological microscopy: Local mechanical properties from microrheology. *Phys. Rev. Lett.* **90**(10), 108301 (2003).

[19] D. T. N. Chen, K. Chen, L. A. Hough, M. F. Islam, and A. G. Yodh. Rheology of carbon nanotube networks during gelation. *Macromolecules* **43**(4), 2048 (2010).

[20] D. T. N. Chen, A. W. C. Lau, L. A. Hough, M. F. Islam, M. Goulian, T. C. Lubensky, and A. G. Yodh. Fluctuations and rheology in active bacterial suspensions. *Phys. Rev. Lett.* **99**(14), 148302 (2007).

[21] D. T. N. Chen, Q. Wen, P. A. Janmey, J. C. Crocker, and A. G. Yodh. Rheology of soft materials. *Ann. Rev. Cond. Mat. Phys.* **1** (2010).

[22] P. Cordier, F. Tournilhac, C. Soulié-Ziakovic, and L. Leibler. Self-healing and thermoreversible rubber from supramolecular assembly. *Nature* **451**, 997 (2008).

[23] J. C. Crocker and D. G. Grier. Methods of digital video microscopy. *J. Colloid and Interface Sci.* **179**, 298 (1996).

[24] J. C. Crocker and B. D. Hoffman. Methods of digital video microscopy. *Methods Cell Biol.* **83**, 141 (2007).

[25] J. C. Crocker, J. A. Matteo, A. D. Dinsmore, and A. G. Yodh. Entropic attraction and repulsion in binary colloids probed with a line optical tweezer. *Phys. Rev. Lett.* **82**(21), 4352 (1999).

[26] J. C. Crocker, M. T. Valentine, E. R. Weeks, T. Gisler, P. D. Kaplan, A. G. Yodh, and D. A. Weitz. Two-point microrheology of inhomogeneous soft materials. *Phys. Rev. Lett.* **85**(4), 888 (2000).

[27] J. G. Curro and P. Pincus. A theoretical basis for viscoelastic relaxation of elastomers in the long-time limit. *Macromolecules* **16**(4), 559 (1983).

[28] J. E. Curtis, B. A. Koss, and D. G. Grier. Dynamic holographic optical tweezers. *Opt. Comm.* **207**, 169 (2002).

[29] B. R. Dasgupta, S. Y. Tee, J. C. Crocker, B. J. Frisken, and D. A. Weitz. Microrheology of polyethylene oxide using diffusing wave spectroscopy and single scattering. *Phys. Rev. E* **65**, 051505 (2002).

[30] P. G. deGennes. *Scaling Concepts in Polymer Physics*. Cornell University Press Ithaca, USA 1st edition (1990).

[31] B. A. DiDonna and D. C. Morse. Gellation of rigid filament networks. , arXiv:cond–mat/0703418v1.

[32] M. Doi and S. Edwards. *The Theory of Polymer Dynamics*. Oxford University Press New York, USA 1st edition (1995).

[33] E. R. Dufresne, T. M. Squires, M. P. Brenner, and D. G. Grier. Hydrodynamic coupling of two brownian spheres to a planar surface. *Phys. Rev. Lett.* **85**(15), 3317 (2000).

[34] B. Fabry, G. N. Maksym, J. P. Butler, and J. J. F. M. Glogauer, D. Navajas. Scaling the microrheology of living cells. *Phys. Rev. Lett.* **87**, 148102 (2001).

[35] L. P. Faucheux, G. Stolovitzsky, and A. Libchaber. Periodic forcing of a brownian particle. *Phys. Rev. E* **51**(6), 5239 (1995).

[36] J. D. Ferry. *Viscoelastic Properties of Polymers*. Wiley New York, USA 1st edition (1980).

[37] M. Foygel, R. D. Morris, D. Anez, S. French, and V. L. Sobolev. Theoretical and computational studies of carbon nanotube composites and suspensions: Electrical and thermal conductivity. *Phys. Rev. B* **71**(10), 104201 (2005).

[38] M. L. Gardel, J. H. Shin, F. C. MacKintosh, L. Mahadevan, P. Matsudaira, and D. A. Weitz. Elastic behavior of cross-linked and bundled actin networks. *Science* **304**(5675), 1301 (2004).

[39] H. Z. Geng, R. Rosen, B. Zheng, H. Shimoda, L. Fleming, J. Liu, and O. Zhou. Fabrication and properties of composites of poly(ethylene oxide) and functionalized carbon nanotubes. *Adv. Mat.* **14**(19), 1387 (2002).

[40] F. Gittes, B. Schnurr, P. D. Olmsted, F. C. MacKintosh, and C. F. Schmidt. Microscopic viscoelasticity: Shear moduli of soft materials determined from thermal fluctuations. *Phys. Rev. Lett.* **79**(17), 3286 (1997).

[41] L. L. Goff, F. Amblard, and E. M. Furst. Motor-driven dynamics in actin-myosin networks. *Phys. Rev. Lett.* **88**, 018101 (2001).

[42] D. G. Grier. A revolution in optical manipulation. *Nature* **424**, 810 (2003).

[43] J. Happel and H. Brenner. *Low Reynolds Number Hydrodynamics*. Kluwer Academic Dordecht, the Netherlands 2nd edition (1991).

[44] Y. Hatwalne and S. Ramaswamy. Rheology of active-particle suspensions. *Phys. Rev. Lett.* **92**(11), 118101 (2004).

[45] C. Hertlein, L. Helden, A. Gambassi, S. Dietrich, and C. Bechinger. Direct measurement of critical casimir forces. *Nature* **451**, 172 (2008).

[46] E. K. Hobbie and D. J. Fry. Rheology of concentrated carbon nanotube suspensions. *J. Chem. Phys.* **126**(12), 124907 (2007).

[47] L. A. Hough, M. F. Islam, P. A. Janmey, and A. G. Yodh. Viscoelasticty of single wall carbon nanotube suspensions. *Phys. Rev. Lett.* **93**(16), 168102 (2004).

[48] L. A. Hough and H. D. Ou-Yang. Correlated motions of two hydrodynamically coupled particles confined in separate quadratic potential wells. *Phys. Rev. E* **65**, 021906 (2002).

[49] L. A. Hough and H. D. Ou-Yang. Viscoelasticity of aqueous telechelic poly(ethylene oxide) solutions: Relaxation and structure. *Phys. Rev. E* **73**, 031802 (2006).

[50] Y. Y. Huang, S. V. Ahir, and E. M. Terentjev. Dispersion rheology of carbon nanotubes in a polymer matrix. *Phys. Rev. B* **73**(12), 125422 (2006).

[51] S. Inoué and K. R. Spring. *Video Microscopy: The Fundamentals*. Plenum Press New York, NY 2nd edition (1997).

[52] M. F. Islam, E. Rojas, D. M. Bergey, A. T. Johnson, and A. G. Yodh. High weight fraction surfactant solubilization of single-wall carbon nanotubes in water. *Nanoletters* **3**, 269 (2003).

[53] G. Koenderink, M. Atakhorrami, F. MacKintosh, and C. Schmidt. High-frequency stress relaxation in semiflexible polymer solutions and networks. *Phys. Rev. Lett.* **96**, 138307 (2006).

[54] L. D. Landau and E. M. Lifshitz. *Theory of Elasticity*. Butterworth-Heinemann Oxford, UK 3rd edition (1986).

[55] T. H. Larsen and E. M. Furst. Microrheology of the liquid-solid transition during gelation. *Phys. Rev. Lett.* **100**(14), 146001 (2008).

[56] R. G. Larson. *The Structure and Rheology of Complex Fluids*. Oxford University Press Oxford, UK 1st edition (1999).

[57] A. W. C. Lau, B. D. Hoffman, A. Davies, J. C. Crocker, and T. C. Lubensky. Microrheology, stress fluctuations, and active behavior of living cells. *Phys. Rev. Lett.* **91**, 198101 (2003).

[58] A. W. C. Lau and T. C. Lubensky. Fluctuating hydrodynamics and microrheology of a dilute suspension of swimming bacteria. *Phys. Rev. E* **80**(1), 011917 (2009).

[59] A. J. Levine and T. C. Lubensky. One- and two-particle microrheology. *Phys. Rev. Lett.* **85**(8), 1774 (2000).

[60] A. J. Levine and T. C. Lubensky. Response function of a sphere in a viscoelastic two-fluid medium. *Phys. Rev. E* **63**, 041510 (2001).

[61] A. J. Levine and T. C. Lubensky. Two-point microrheology and the electrostatic analogy. *Phys. Rev. E* **65**, 011501 (2001).

[62] K. H. Lin. *Entropically Driven Interaction Between Colloids and their self-assembly*. PhD dissertation University of Pennsylvania Department of Physics and Astronomy Aug (2002).

[63] Y. C. Lin, G. H. Koenderink, F. C. MacKintosh, and D. A. Weitz. Viscoelastic properties of microtubule networks. *Macromolecules* **40**(21), 7714 (2007).

[64] T. Liverpool and M. Marchetti. Instabilities of isotropic solutions of active polar filaments. *Phys. Rev. Lett.* **90**, 138102 (2003).

[65] C. W. Macosko. *Rheology: Principles, Measurements, and Applications*. Wiley-VCH, Inc New York, USA 1st edition (1994).

[66] D. S. Martin, M. B. Forstner, and J. A. Kas. Apparent subdiffusion inherent to single particle tracking. *Biophys. J.* **83**, 2109 (2002).

[67] P. Martin, A. J. Hudspeth, and F. Julicher. Comparison of a hair bundle's spontaneous oscillations with its response to mechanical stimulation reveals the underlying active process. *Proc. Nat. Acad. Sci.* **98**(25), 14380 (2001).

[68] T. G. Mason. Estimating the viscoelastic moduli of complex. fluids using the generalized stokes einstein equation. *Rheol. Acta.* **39**, 371 (2000).

[69] T. G. Mason, K. Ganesan, J. H. van Zanten, D. Wirtz, and S. C. Kuo. Particle tracking microrheology of complex fluids. *Phys. Rev. Lett.* **79**(17), 3282 (1997).

[70] T. G. Mason and D. A. Weitz. Optical measurements of frequency-dependent linear viscoelastic moduli of complex fluids. *Phys. Rev. Lett.* **74**(7), 1250 (1995).

[71] J.-C. Meiners and S. Quake. Direct measurement of hydrodynamic cross correlations between two particles in an external potential. *Phys. Rev. Lett* **82**(10), 2211 (1999).

[72] D. Mizuno, C. Tardin, C. F. Schmidt, and F. C. MacKintosh. Nonequilibrium mechanics of active cytoskeletal networks. *Science.* **315**, 370 (2007).

[73] J. R. Moffitt, Y. R. Chemla, S. B. Smith, and C. Bustamante. Recent advances in optical tweezers. *Ann. Rev. Biochem.* **77**, 205 (2008).

[74] M. Moniruzzaman and K. I. Winey. Polymer nanocomposites containing carbon nanotubes. *Macromolecules* **39**(16), 5194 (2006).

[75] V. Narayan, N. Menon, and S. Ramaswamy. Nonequilibrium steady states in a vibrated-rod monolayer: tetratic, nematic, and smectic correlations. *Journal of Statistical Mechanics-Theory and Experiment* **01**, P01005 (2006).

[76] V. Narayan, S. Ramaswamy, and N. Menon. Long-lived giant number fluctuations in a swarming granular nematic. *Science* **317**(5834), 105 (2007).

[77] K. C. Neuman and S. M. Block. Optical trapping. *Rev. Sci. Inst.* **75**(9), 2787 (2004).

[78] R. Nossal. Spectral analysis of laser light scattered from motile microorganisms. *Biophys. J.* **11**, 341 (1971).

[79] S. Park, P. M. Wolanin, E. A. Yuzbashyan, H. Lin, N. C. Darnton, J. B. Stock, P. Silberzan, and R. Austin. Influence of topology on bacterial social interaction. *Proc. Nat. Acad. Sci.* **100**(24), 13910 (2003).

[80] J. S. Parkinson. Complementation analysis and deletion mapping of escherichia coli mutants defective in chemotaxis. *J. Bacteriology* **135**(1), 45 (1978).

[81] N. Pernodet and B. Tinland. Influence of λ-dna concentration on mobilities and dispersion coefficients during agarose gel electrophoresis. *Biopolymers* **42**, 471 (1997).

[82] C. P. Pomona. Kohler microscope alignment procedure. `http://www.csupomona.edu/~biology/docs/kohler.htm`.

[83] X.-L. Qiu, P. Tong, and B. Ackerson. Proposal and testing of dual-beam dynamic light scattering for two-particle microrheology. *Appl. Opt.* **43**(17), 3382 (2004).

[84] S. Rafai, L. Jibuti, and P. Peyla. Effective viscosity of microswimmer suspensions. *Phys. Rev. Lett.* **104**, 098102 (2010).

[85] S. Ramaswamy. The mechanics and statistics of active matter. *Ann. Rev. Cond. Mat. Phys.* **1** (2010).

[86] F. Reif. *Fundamentals of Statistical and Thermal Physics*. McGraw-Hill New York, USA 1st edition (1965).

[87] M. Rubinstein and R. H. Colby. *Polymer Physics*. Oxford University Press Oxford, UK 1st edition (2003).

[88] W. Russel, D. Saville, and W. Schowalter. *Colloidal Dispersions*. Cambridge University Press Cambridge, UK 1st edition (1989).

[89] D. Saintillan and M. J. Shelley. Orientational order and instabilities in suspensions of self-locomoting rods. *Phys. Rev. Lett.* **99**, 058102 (2007).

[90] J. Sambrook, E. Fritsch, and T. Maniatis. *Molecular Cloning- A Lab Manual*. Cold Spring Harbor Laboratory Press New York, USA 2nd edition (1989).

[91] T. Savin and P. S. Doyle. Role of a finite exposure time on measuring an elastic modulus using microrheology. *Phys. Rev. E* **71**(4), 041106 (2005).

[92] T. Savin and P. S. Doyle. Static and dynamic errors in particle tracking microrheology. *Biophys. J.* **88**(1), 623 (2005).

[93] B. Schnurr, F. Gittes, F. MacKintosh, and C. Schmidt. Determining microscopic viscoelasticity in flexible and semiflexible polymer networks from thermal fluctuations. *Macromolecules* **30**(25), 7781 (1997).

[94] R. A. Simha and S. Ramaswamy. Hydrodynamic fluctuations and instabilities in ordered suspensions of self-propelled particles. *Phys. Rev. Lett.* **89**(5), 058101 (2002).

[95] A. Sokolov and I. S. Aranson. Reduction of viscosity in suspension of swimming bacteria. *Phys. Rev. Lett.* **103**, 148101 (2009).

[96] G. V. Soni, B. M. J. Ali, Y. Hatwalne, and G. V. Shivashankar. Single particle tracking of correlated bacterial dynamics. *Biophys. J.* **84**, 2634 (2003).

[97] T. M. Squires. Nonlinear microrheology: Bulk stresses versus direct interactions. *Langmuir* **24**, 1147 (2008).

[98] T. M. Squires and J. F. Brady. A simple paradigm for active and nonlinear microrheology. *Physics of Fluids* **17**, 073101 (2005).

[99] T. M. Squires and T. G. Mason. Fluid mechanics of microrheology. *Ann. Rev. Fluid Mech.* **42**, 413 (2010).

[100] L. Starrs and P. Bartlett. Colloidal dynamics in polymer solutions: Optical two-point microrheology measurements. *Faraday Disc.* **123**, 323 (2002).

[101] I. Z. Steinberg. On the time reversal of noise signals. *Biophys. J.* **50**, 171 (1986).

[102] C. Storm, J. J. Pastore, F. C. MacKintosh, T. C. Lubensky, and P. A. Janmey. Nonlinear elasticity in biological gels. *Nature* **435**(7039), 191 (2005).

[103] K. Svoboda and S. M. Block. Biological applications of optical forces. *Ann. Rev. Biophys. Biomol. Struct.* **23**, 247 (1994).

[104] J. Toner and Y. Tu. Long-range order in a two-dimensional dynamical xy model: How birds fly together. *Phys. Rev. Lett.* **75**, 4326 (1995).

[105] J. Toner, Y. Tu, and S. Ramaswamy. Hydrodynamics and phases of flocks. *Annals of Physics* **318**(1), 170 (2005).

[106] I. Tuval, L. Cisneros, C. Dombrowski, C. W. Wolgemuth, J. O. Kessler, and R. E. Goldstein. Bacterial swimming and oxygen transport near contact lines. *Proc. Nat. Acad. Sci.* **102**(7), 2277 (2005).

[107] P. T. Underhill, J. P. Hernandez-Ortiz, and M. D. Graham. Diffusion and spatial correlations in suspensions of swimming particles. *Phys. Rev. Lett.* **100**, 248101 (2008).

[108] M. T. Valentine, L. E. Dewalt, and H. D. Ou-Yang. Forces on a colloidal particle in a polymer solution: a study using optical tweezers. *J. Phys. Cond. Mat.* **8**, 9477 (1996).

[109] M. T. Valentine, Z. E. Perlman, M. L. Gardel, J. H. Shin, P. Matsudaira, T. J. Mitchison, and D. A. Weitz. Colloid surface chemistry critically affects multiple particle tracking measurements of biomaterials. *Biophys. J.* **86**, 4004 (2004).

[110] R. Verma. *Entropic Attractions in Colloid-Polymer Solutions*. PhD dissertation University of Pennsylvania Department of Physics and Astronomy Aug (1999).

[111] R. Verma, J. C. Crocker, T. C. Lubensky, and A. G. Yodh. Entropic colloidal interactions in concentrated dna solutions. *Phys. Rev. Lett.* **81**(18), 4004 (1998).

[112] R. Verma, J. C. Crocker, T. C. Lubensky, and A. G. Yodh. Attractions between hard colloidal spheres in semiflexible polymer solutions. *Macromolecules* **33**(1), 177 (2000).

[113] N. J. Wagner and J. F. Brady. Shear thickening in colloidal dispersions. *Phys. Today* **62**, 27 (2009).

[114] T. A. Waigh. Microrheology of complex fluids. *Rep. Prog. Phys.* **68**, 685 (2005).

[115] E. Weeks. Particle tracking using idl. http://www.physics.emory.edu/~weeks/idl/.

[116] J. Wilhelm and E. Frey. Elasticity of stiff polymer networks. *Phys. Rev. Lett.* **91**(10), 108103 (2003).

[117] H. H. Winter and F. Chambon. Analysis of linear viscoelasticity of a cross-linking polymer at the gel point. *Journal of Rheology* **30**(2), 367 (1986).

[118] X. L. Wu and A. Libchaber. Particle diffusion in a quasi-two-dimensional bacterial bath. *Phys. Rev. Lett.* **84**, 3017 (2000).

[119] K. Xu, M. G. Forest, and I. Klapper. On the correspondence between creeping flows of viscous and viscoelastic fluids. *J. of Non-Newtonian Fluid Mech.* **145**(2-3), 150 (2007).

[120] S. Yamada, D. Wirtz, and S. C. Kuo. Mechanics of living cells measured by laser tracking microrheology. *Biophys. J.* **78**(4), 1736 (2000).

[121] H. P. Zhang, A. Be'er, R. S. Smith, E.-L. Florin, and H. L. Swinney. Swarming dynamics in bacterial colonies. *Europhys. Lett.* **87**(4), 48011 (2009).